STRESS-INDUCED EQUIVALENT PERMEABILITY ESTIMATION AND ITERATIVELY-COUPLED FLUID FLOW AND GEOMECHANICS SIMULATION USING FRACTAL AND STATISTICAL METHODS

A Dissertation

by

SANGYUP LEE

Submitted to the Office of Graduate and Professional Studies of
Texas A&M University
in partial fulfillment of the requirements for the degree of

DOCTOR OF PHILOSOPHY

Chair of Committee,	David Schechter
Committee Members,	John Killough
	Eduardo Gildin
	Marcelo Sanchez
Head of Department,	A. Daniel Hill

August 2016

Major Subject: Petroleum Engineering

ABSTRACT

Permeability and porosity are two of the key parameters of reservoir simulations. For naturally fractured reservoir simulations, when matrix porosity is negligible, it is important to estimate the proper fracture porosity and permeability to obtain accurate simulation results. However, it is very difficult to measure and estimate such parameters, due to factors such as the high heterogeneity of fluid and fracture properties, scale differences between the sampling window and actual reservoir domain, and so on.

In order to reduce the scale discrepancy error and properly describe natural-like fracture aperture characteristics, fractal theory has been adopted, and a cumulative distribution function of the generated fracture networks was calculated after a 1,000-time Monte Carlo simulation. P50 case was then selected as the reservoir fracture map.

The Discrete Fracture Network (DFN) approach can be effective when a limited numbers of fractures dominate the fluid flow in the fractured reservoir. However, if the reservoir has a very complex and large numbers of fractures, using the DFN approach to simulate a fracture flow will require significant computational effort and time. Therefore, in such cases the Equivalent Continuum (EC) approach is more suitable. I developed equivalent permeability calculation codes through a modified Oda's algorithm; the heterogeneous nature of the fracture network was reflected by using the full tensor permeability method.

I developed Stress-Induced Permeability Changing (SIPC) coupling simulation codes to better describe the anisotropic behavior and more accurately reflect the

geomechanical characteristics in the coupling simulation. For that, I combined DFN and EC schemes for the SIPC coupling simulation. During the coupling simulation, generated discrete fracture network and aperture data were imported into the coupling simulator, and openings/closings of the apertures due to stress/strain changes were calculated using a kriging scheme. Permeability and porosity were directly estimated via the aperture opening/closing calculation.

After a comparison of the FDM and iterative coupling simulations, it was observed that the SIPC coupling simulation successfully described the anisotropic characteristics of the directional permeability estimation, and reflected the reservoir properties in the coupling simulation. The combined DFN and EC approach was effectively applied to the stress-induced permeability changing reservoir coupling simulation.

DEDICATION

I dedicate my doctoral dissertation to my lovely wife, Eunjeong. Without her unwavering support and love, I could not have completed this work.

I also dedicate my work to my family: my parents, parents-in-law, brother, sister, and all of my sisters-in-law. They have always believed in and prayed for me.

I also want to offer special thanks to my friends. They have always encouraged and supported me.

ACKNOWLEDGEMENTS

I am grateful to my supervisor, Dr. Schechter, whose expertise, generous guidance, and support made it possible for me to complete this research. It was a pleasure working with him.

I would also like express my gratitude to my committee members: Dr. Killough, Dr. Gildin, and Dr. Sanchez. They spent valuable time with me and were an excellent source of inspiration.

Finally, I am thankful to all of my colleagues for their encouragement and support.

TABLE OF CONTENTS

Page

Page

Page

LIST OF FIGURES

Page

Page

Page

LIST OF TABLES

Page

CHAPTER I

INTRODUCTION

1.1 Statement of the Problem

Porosity and permeability are key parameters in reservoir simulations. It is important to properly estimate them in order to obtain accurate simulation results (T. H. Kim & Schechter, 2009; Y. Wang et al., 2013). However, Naturally Fractured Reservoirs (NFRs) usually have scale-dependent and highly heterogeneous fracture geometries, making it almost impossible to estimate proper in-situ fracture porosity and permeability. In addition, because researchers can only obtain a very limited range of survey data, it is always challenging to directly apply sampling/logging data to field-scale simulations. In order to reduce scale discrepancy errors and properly describe natural-like fracture aperture characteristics in this research, fractal theory has been adopted. A previous study developed Fractal Discrete Fracture Network (FDFN) generation codes (T. H. Kim & Schechter, 2009) for use in generating fracture networks based on outcrop maps, core samples, and/or image log data. FDFN simulation codes generate fracture networks with natural-like fracture aperture characteristics. Such generated fracture apertures would either follow a constant, normal, or log normal aperture distribution. From the generated fracture data, the codes could then directly calculate fracture porosity using the generated fracture geometry and aperture distribution data.

Because fractal and statistical methods were used to generate the fracture networks, the generated fracture geometries may be different, even if the same input data were used. Therefore, a Cumulative Distribution Function (CDF) of the generated fracture networks was calculated after a 1,000-time Monte Carlo simulation, and the P10, P50, and P90 fracture network distribution maps were estimated. The P50 case was selected as the reservoir fracture map, and fracture network data were imported into the equivalent permeability estimation codes.

In this studies, the generated fracture apertures followed a normal distribution. For the sake of simplicity, the natural-like aperture distribution was simplified as a set of consecutive rectangular cells in the simulation. In the case study of fracture geometry effect on equivalent permeability estimation, a single averaged aperture value of each fracture was calculated and assigned for the equivalent permeability estimation. Each fracture had a different single averaged aperture value, depending upon the fracture geometry, but the distribution of the total averaged apertures of all fracture networks also followed a normal distribution.

To estimate the production performance with a large number of fractures, I used an Equivalent Continuum (EC) scheme. The codes were used to calculate the directional equivalent permeability distributions using the generated fracture network data, by employing a statistical and modified Oda's algorithm. The heterogeneous nature of the fracture networks was reflected by adopting the full tensor permeability scheme (Harstad et al., 1996; Brown & Bruhn, 1998; Y. Wang et al., 2013). Calculated permeability data were passed to the coupling simulator.

Conventional reservoir simulations have widely been used to analyze diverse reservoir problems, and in many cases have shown appropriate simulation results. In traditional reservoir engineering, the geomechanical characteristics of a rock matrix, such as displacement, stress, and strain change are not of primary interest, and thus are usually neglected or simplified. Therefore, in most cases, fracture porosity and permeability are considered to be either static or pressure-dependent variables, and not incorporated with the stress/strain change of the solid matrix during simulations. However, because the effective stress changes in the solid matrix and pore pressure changes in the fluids simultaneously affect one another in an ongoing process, a coupled analysis of fluid flow and geomechanics is required for more accurate simulation results, especially in cases of stress-sensitive or poorly compacted reservoirs. Therefore, I developed two-dimensional, iterative coupling simulation codes to investigate the interaction effects generated by the fluid flow and geomechanics. The fluid flow in porous media was first solved by the Finite Difference Method (FDM). In this study, the MATLAB Reservoir Simulation Toolbox (MRST) framework was used for the fluid flow simulator (Lie et al., 2011). The pore pressure calculated by FDM was passed to the elasto-plastic geomechanics model to calculate stress and volumetric strain changes for each element, using the Finite Element Method (FEM). The Mohr-Coulomb failure model employed in this study is a model that has been widely used to describe elasto-plastic properties. Porosity was a convergence-checking parameter for the coupling simulation.

Some assumptions were employed in the equivalent permeability and iterative coupling simulations. The solid particles were incompressible; thus, small strain theory was assumed so that linear elasticity theory could be used. The solid material was isotropic with respect to the rock's mechanical properties. The solid velocity was very small; Darcy's law was valid for the fluid flow. Also, an isothermal condition was assumed. Finally, the reservoir fractures were well connected to one another. The Representative Elementary Volume (REV), an important assumption when using the EC approach (Bear, 1972), was checked before the simulation.

In the iterative coupling simulation, equivalent permeability was updated at each time step by empirical relationships controlled by volumetric strain and/or porosity variations. However, these empirical equations had certain limitation of describing the anisotropic characteristics of directional permeability because porosity and volumetric strain are isotropic variables. In addition, it was difficult for the EC approach to properly describe the fracture flow effect on the simulation, due to certain inherent characteristics of the method.

In this study, I developed Stress-Induced Permeability Changing (SIPC) coupling simulation codes to better describe the anisotropic behavior and more accurately reflect the geomechanical characteristics in the coupling simulation. For that, two different simulation schemes were combined for the SIPC coupling simulation; a Discrete Fracture Network (DFN) scheme was used to generate the fracture network map and aperture data, and an EC scheme was used to run the coupling simulation with a large number of fractures, effectively using less computational effort. During the coupling

simulation, the generated discrete fracture network and aperture data were imported into the coupling simulator. The domain was divided into numbers of sub-domains, and the divided sub-domain cells contained corresponding fracture segments. Then, the middle points of the fracture segments in each sub-domain cell were calculated. The normal and shear stresses at these middle points in the fracture segments were interpolated from estimated nodal stresses using an ordinary kriging scheme. The changes in aperture values resulted in openings/closings of the apertures. The permeability and fracture porosity were directly calculated after this aperture opening/closing calculation. Figure 1.1 is a flow chart of the simulation procedure. In Figure 1.1 (b), aperture change calculation scheme was only used for SIPC coupling simulation case. In the iterative coupling scheme, aperture calculation step was skipped, and permeability was updated by empirical equations.

As a synthetic field case study, a stress-sensitive reservoir was considered, and the Belridge and Lost Hills (LH) oil fields in California were selected for this study. Because some of the Belridge and Lost Hills field data were not available, I tried to select a reasonable field data through a series of literature reviews. Two filed case studies were performed; a 5-spot pattern case study with a relatively large domain size, and a horizontal well case study with a small domain size.

All codes were written in MATLAB®.

1.2 Objectives

The objectives of this research were to:

- Estimate the equivalent directional permeability distribution using generated FDFN geometry and aperture distribution data;
- Develop stress-induced equivalent permeability changing and iterative coupling simulation codes;
- Investigate the effects of the geomechanical properties on the coupling simulation;
- Directly estimate the stress-induced changes of fracture porosity, aperture and directional equivalent permeability; and
- Propose a combined DFN and EC scheme to better describe the anisotropic behavior and more accurately reflect the geomechanical characteristics in the coupling simulation.

1.3 Significance

I estimated the directional permeability distribution using generated FDFN and aperture distribution data; the simulation results reflected the heterogeneous characteristics of the fracture network geometry. The estimated permeability data were passed to the coupling simulator.

In this study, I developed SIPC coupling simulation codes. SIPC coupling simulation scheme better described the anisotropic behavior and more accurately reflected the geomechanical characteristics than did the iterative coupling simulation scheme using empirical relationship to estimate directional permeability change.

In order to simulate the stress-induced aperture change, I proposed a method combining two different DFN and EC schemes. A DFN method was used to generate the fracture network map and aperture data, and an EC method was used to run the coupling simulation with a large number of fractures, effectively using less computational effort.

The literature review conducted for this study uncovered no research using this combined DFN and EC scheme in a stress-induced permeability changing coupling simulation.

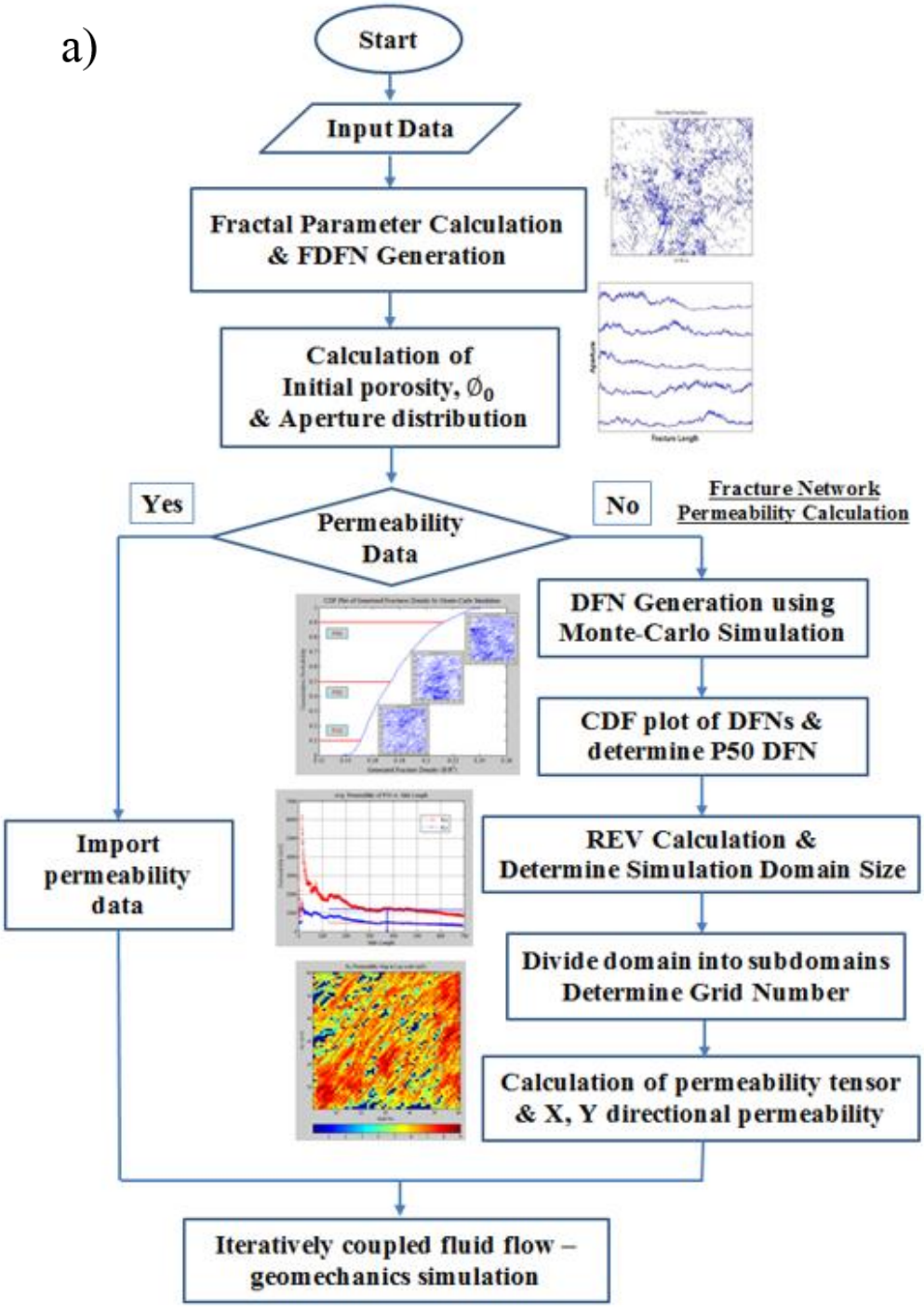

Figure 1.1 Flow chart of the simulation: a) Flow chart illustrating the equivalent permeability calculation. b) Flow chart of the iterative coupling procedure.

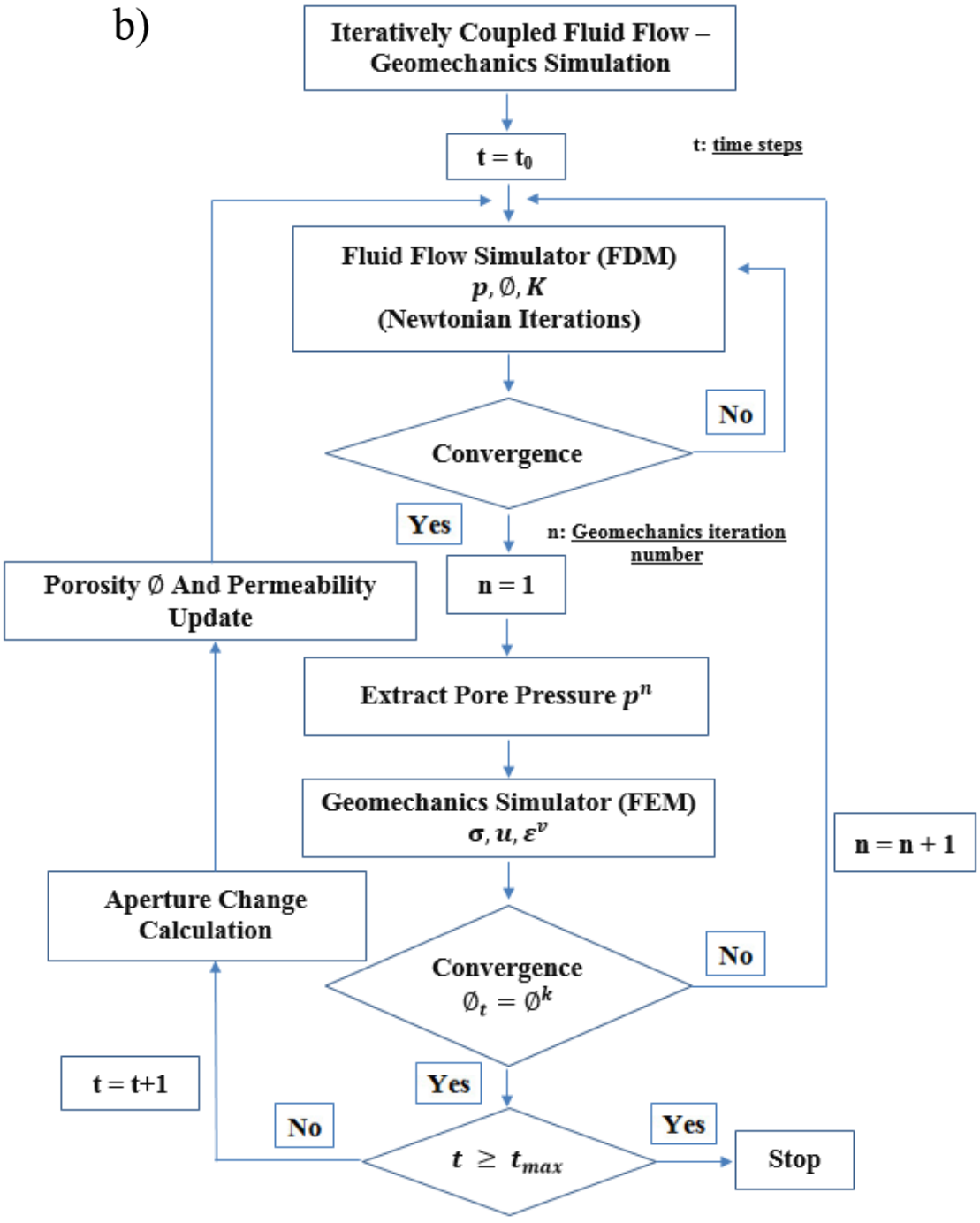

Figure 1.1 Continued.

CHAPTER II

LITERATURE REVIEW

2.1 Fractal Theory

Mandelbrot (1983) first described the concept of the fractal as a "rough or fragmented geometric shape that can be split into parts, each of which is a reduced-size copy of the whole". Fractals are usually categorized into two groups: self-similar and self-affine. A self-similar fractal has an isotropic scale factor in every spatial direction and conserves its statistical similarities among various scales. A Koch curve is the classic example of a self-similar fractal. On the other hand, a self-affine fractal has an anisotropic scale and a different scale factor along each of its spatial directions. Several studies have shown that fractures have self-affine fractal properties (Sakellariou et al., 1991; Kulatilake & Um, 1999; Fardin et al., 2001; T. H. Kim & Schechter, 2009).

Feder (1988) defined a fractal dimension as a statistical quantity of complexity showing how a fractal pattern completely changes through alterations to the scale. Katz and Thompson (1985) applied fractal theory to investigate the pore space of sandstone samples, and showed that the pore spaces had similar fractal characteristics. Chang and Yortsos (1990) applied fractal theory to a slightly compressible and single-phase fluid flow reservoir simulation process. They modified a Warren-Root model, designed a fractal fracture network with a Euclidean matrix, and proposed a fractal diffusivity equation.

Sakellariou et al. (1991) proposed that a rock surface has a self-affine random fractal property. They expressed roughness with a Joint Roughness Coefficient (JRC) and fractal dimension. Based on this theory, a fracture aperture can be expressed using a self-affine fractal property. Olarewaju (1996) described a heterogeneous reservoir permeability field using effective permeability and a fractal dimension from a well test analysis. He solved the pressure diffusivity equation using transformations similar to those of Chang and Yortsos (1990).

The modified Successive Random Addition (SRA) method is used for generating fracture aperture distribution. SRA is the most common mathematical algorithm for generating fractional Brownian motion (fBM) (McGaughey & Aitken, 2000; Liu et al., 2004; T. H. Kim & Schechter, 2009).

T. H. Kim and Schechter (2009) developed a 2D/3D fractal discrete fracture network (FDFN) generation code and calculated fracture porosity using a natural-like aperture distribution with a modified SRA method. These codes were used in this study to generate a discrete fracture network.

2.2 Equivalent Permeability Estimation

The numerical simulation of fluid flow in a fractured reservoir can be categorized into two methods: explicit (or discrete) and implicit (or equivalent continuum). The Discrete Fracture Network (DFN) approach recognizes fracture geometry and treats it discretely. It is effective when considering a limited number of fractures dominating the fluid flow in a fractured reservoir. The equivalent continuum approach uses equivalent

permeability tensor notation instead of ignoring the fracture geometry. Thanks to progress in computational and surveying technologies, we can now consider and simulate more accurate and detailed reservoir features, and the DFN approach appears to be more accurate for fracture flow simulation. However, if the reservoir has very complex and large numbers of fractures, then simulating the fracture flow via the DFN approach requires a substantial amount of computational effort and time. Therefore, in such cases the equivalent continuum approach may be more suitable. To obtain equivalent parameters such as porosity and permeability, it is important to simulate the fluid flow in the fractured reservoir (Amaziane et al., 2001; W. Dershowitz et al., 2004; He et al., 2013).

Oda (1985) considered fractured rock mass to be homogeneous and anisotropic porous media. In this approach, fluid flow follows Darcy's law and the permeability properties are related to the fracture geometry. Oda used permeability tensor notation, which represents permeability orientation and magnitude; he then compared his calculated permeability tensor results with the simulation results obtained by Long et al. (1982). He expressed fracture orientation using two opposing directional unit normal vectors, $+n$ and $-n$. Even though Oda's method has some limitations – it does not consider fracture size and is only applicable to cases with well-connected fractured reservoirs – it definitely has an advantage in that it can calculate equivalent permeability without running flow simulations (B. Dershowitz et al., 2000).

Harstad et al. (1996) suggested a positive scalar correction value to make up for the shortcomings in Oda's method, which has non-zero permeability even when a crack

tensor becomes negligibly small. He also applied a modified version of Oda's model to the field data obtained by Frontier Sandstone. B. Dershowitz et al. (2000) calculated the permeability tensor using equivalent permeability tensor methods in a discrete fracture network simulation. M. Wang et al. (2002) calculated the REV and a three-dimensional hydraulic conductivity tensor for a discrete fracture flow model, and confirmed that hydraulic conductivity in different directions does not change when the block size is greater than the REV size.

Min and Jing (2003; 2004) calculated the equivalent elastic compliance tensor using the distinct element method. They used a two-dimensional distinct element method program, UDEC, and developed several stochastic DFNs of various scales. They studied the scale dependency and tensor characteristics of the mechanical properties of fractured rock masses and determined the REV.

However, even though previous studies have considered both fracture geometry and aperture data, they have all had certain limitations, especially in that the fracture followed a constant aperture distribution. When there were no available aperture data, many researchers used cubic laws to back-calculate the constant aperture value from the flow rate. In this study, a discrete fracture network and its aperture distribution were generated by FDFN codes using surveying data. The generated apertures followed either a constant, normal, or log-normal distribution. After the fracture porosity calculation, the generated aperture distribution was simplified as a set of consecutive rectangular cells for the equivalent permeability estimation.

2.3 Coupled Fluid Flow and Geomechanics

Conventional reservoir simulations have been widely used to analyze diverse reservoir problems, and in many cases they have shown appropriate simulation results. In traditional reservoir engineering, the geomechanical characteristics of a rock matrix (such as displacement stress and strain change) are not of primary interest, and are usually either neglected or simplified. Also, the interaction effect between the fluid flow and solid matrix are often ignored. Therefore, in most cases, fracture porosity and permeability are considered to be static or pressure-dependent variables, and are not incorporated into the stress/strain change of the solid matrix during simulations. However, because effective stress changes in the solid matrix and pore pressure changes in fluids simultaneously affect one another and this interaction is an ongoing process, a coupled analysis of fluid flow and geomechanics is required in order to obtain more accurate simulation results regarding stress-sensitive or weak reservoir conditions (Chin et al., 2002). A coupling simulation is especially necessary for analyzing special phenomena (such as subsidence problems, wellbore stability, and failure) that a traditional reservoir simulator cannot adequately describe (Antonin Settari & Mourits, 1998; Tran et al., 2004; Pan, 2009).

The fundamental equations coupling geomechanics and fluid flow were first analyzed by Terzaghi (1926; 1943). He tried to solve the consolidation problem using an effective stress concept. Based on Terzaghi's theory, (Biot, 1941) developed a generalized 3D formulation of consolidation using a linear stress-strain relationship and single phase fluid flow. Following their work, many researchers have studied the

coupling of fluid flow and geomechanics (Geertsma, 1957; Antonin Settari & Mourits, 1998; Chin et al., 2002; Thomas et al., 2003; Tran et al., 2004; Jalali & Dusseault, 2008; Pan et al., 2009).

Antonin Settari and Mourits (1998) first applied their iterative coupling scheme in the petroleum engineering field. They also developed and tested the iteratively modular coupling of a commercial reservoir simulator and three-dimensional stress code (Antonin Settari & Mourits, 1998).

Chen et al. (1995) showed how Biot's two-phase, linear, poroelastic and isothermal model is applicable to the conventional porous fluid flow model.

Chin et al. (2000) developed a fully coupled procedure for isothermal single-phase flow in a porous medium in order to analyze pressure-transient problems in stress-sensitive reservoirs. They applied their methods to an analysis of laboratory compaction data and a well test analysis of a high/low permeability reservoir. They concluded that the sensitivity of the permeability change to other parameters was the most influential factor affecting well productivity in stress sensitive reservoirs.

Chin et al. (2002); Thomas et al. (2003) developed iteratively coupled procedures for a multiphase flow in a fractured reservoir. They used parallel computing methods for geomechanics models, showing that these methods could increase the speed of geomechanics computations.

Tran (2002; 2004; 2005) used an iteratively coupled scheme to simulate reservoir flow in porous media by using a novel porosity formula. Their commercial reservoir simulations considered the bulk volumes of reservoir blocks to be constant. However,

the reservoir pore volume (true pore volume) was changed by the geomechanics computation; it had to be equal to the reservoir pore volume. Therefore, they suggested a novel relationship of porosity as a function of pressure, temperature, and mean total stress.

Gai (2004) applied an iterative coupling scheme in parallel computing and studied convergence with respect to fluid and rock properties. Lu (2008) used an iteratively coupled scheme to simulate the multiphase flow of porous media.

Pan (2009) developed both iteratively and fully coupled geomechanical modules to integrate with GPAS. He coupled a geomechanical module with a dual-porosity GPAS module to simulate a naturally-fractured reservoir.

J. Kim (2010) analyzed the performances of different iteratively coupled methods (sequential methods) for coupled flow and geomechanics. He examined the stability, convergence, accuracy, and efficiency of the sequential methods by considering a drained and undrained split scheme.

Settari and Mourits (1998) divided coupling methods into two categories: "volume coupling" and "coupling through flow properties." Because fluid flow and geomechanics models calculate pore volume changes in different ways, the results of pore volume changes obtained from the two models are usually different from one another. Coupling requires the same pore volume change in both models. This is "volume coupling," and porosity is a coupling parameter. The "coupling through flow properties" method is also called "stress-permeability coupling." In this method, permeability is a coupling parameter, and changes in porosity and permeability are

related to normal stresses, shear stresses, and compaction (Albinali et al., 2011). Later, A. Settari and Walters (2001) expanded the application of their iteratively modular coupled method into a full-field reservoir model.

Methods coupling fluid flow and geomechanics models can be differently classified into four coupling methods, as described below (Tran et al., 2004; Jalali & Dusseault, 2008; Pan, 2009; J. Kim, 2010; Albinali et al., 2011; Rayan, 2014):

In this study, I used an iteratively coupled method with a volume coupling scheme. Prosity was the coupling parameter.

1) **Loosely Coupled Method.** In the loosely coupled method, fluid and geomechanics models were coupled only after a predefined time step (see Figure 2.1). This coupling scheme generated less computational cost than other coupling schemes, but the simulation results were far less accurate.

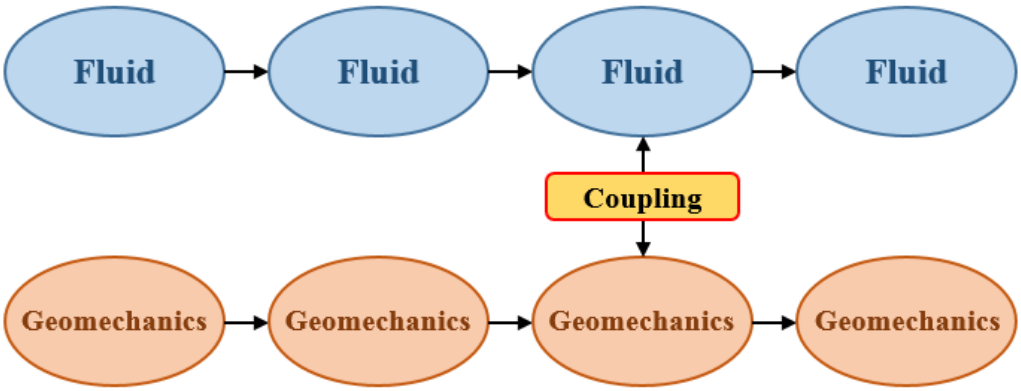

Figure 2.1 Loosely coupled method.

2) **Explicitly Coupled Method.** The explicitly coupled method is also called one-way or staggered coupling because information calculated from the fluid flow model is passed to the geomechanics model in only one direction, and vice versa (see Figure 2.2). In each time step, only one iteration is taken.

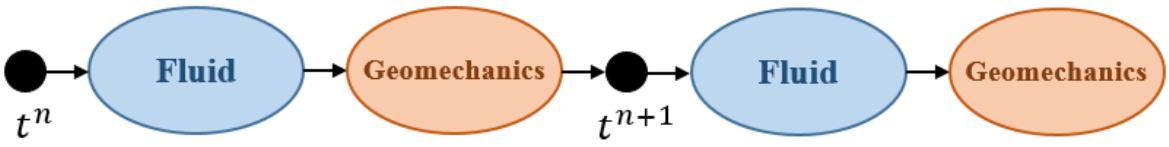

Figure 2.2 Explicitly coupled method.

3) **Iteratively Coupled Method.** In this method, either the fluid or geomechanical parameters are solved first; then, the other parameters are solved sequentially (see Figure 2.3). The exchange of calculated information is performed by iterations at each time step, conducted through the coupling module; this continues until the convergence is below an acceptable tolerance level.

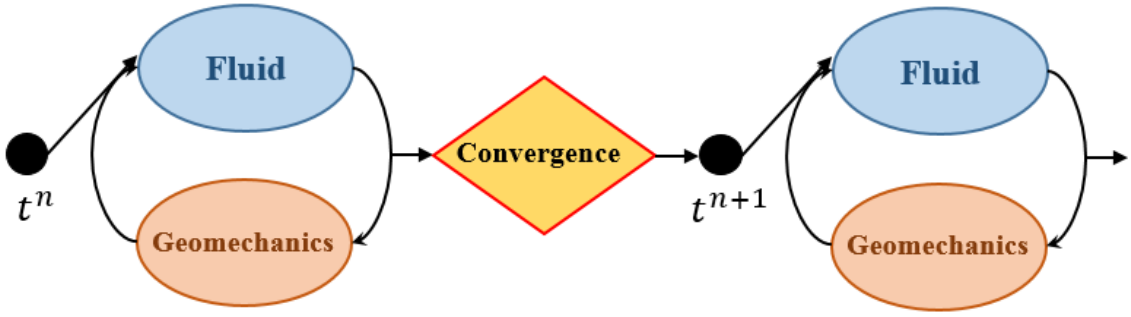

Figure 2.3 Iteratively coupled method.

4) **Fully Coupled Method.** The fully coupled method is sometimes called the implicitly coupled method because the fluid flow and geomechanics equations are discretized on one grid cell and solved simultaneously at every time step (see Figure 2.4).

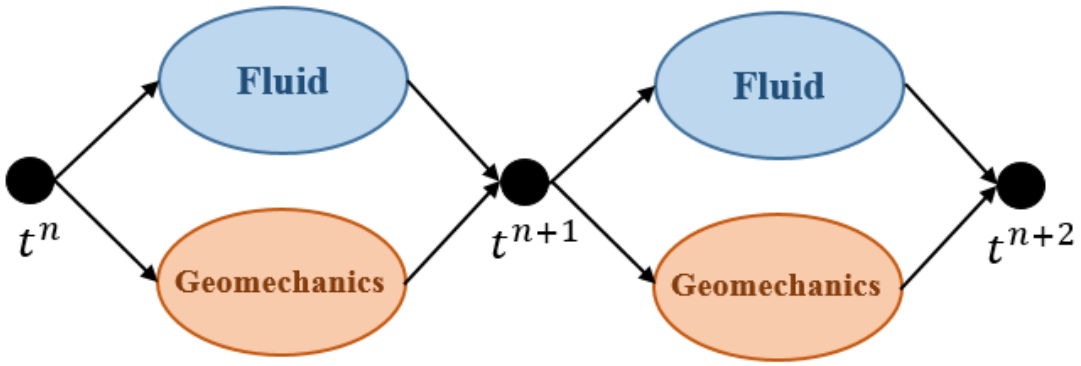

Figure 2.4 Fully coupled method

As shown in Table 2.1, many researchers have proposed various relationships to estimate permeability changes using the results of coupled simulations. However, most equations estimate permeability using porosity changes; they have certain limitations that reflect the heterogenous characteristics of permeabilty distributions. Furthermore, it was difficult to directly apply these equations to different reservoir conditions because weak consideration was made regarding rock properties.

In this study, I proposed a stress-induced pemeability changing and iterative coupling simualtion method. I combined two different DFN and EC schemes for the

coupling simulation. The pore pressure changes calculated by the fliuid flow simulaions resulted in effective stress changes in the geomechanics models. The effective normal and shear stress changes of each fracture were estimated by an ordinary kring scheme, and then normal stiffness was calculated. Stress-induced fracture aperture deformations were calculated by using estimated fracture stresses, normal stiffness and rock properties. Then, the directional permeability distribution was directly calculated by fracture geomtry and changed aperture data. Through this method, better permeability estimations for the different reservoir conditions were possible when the proper reservoir properties were available.

Table 2.1 Permeability relationships

Name	Equation	Variables
Fractures	$k = \frac{0.544 \times 10^8 \times w^3}{h}$	k = permeability (D) w = fracture aperture (in) h = fracture width (in)
Tixier	$k = 62.5 \frac{\phi^6}{S_{wi}^2}$	k = permeability (mD) ϕ = porosity S_{wi} = irreducible water saturation
Wyllie and Rose	$k = \left(\frac{100\phi^2 [1 - S_{wi}]}{S_{wi}} \right)^2$	k = permeability (mD) ϕ = porosity S_{wi} = irreducible water saturation
Timur	$k = 8.58 \frac{\phi^{4.4}}{S_{wi}^2}$	k = permeability (mD) ϕ = porosity S_{wi} = irreducible water saturation
Coates and Dumanoir	$k = 4.90 \frac{\phi^4 (1 - S_{wi})^2}{S_{wi}^4}$	k = permeability (mD) ϕ = porosity S_{wi} = irreducible water saturation
Kozeny-Carman	$k = \frac{cd^2\phi^3}{(1-\phi)^2}$	k = permeability (mD) c = constant ϕ = porosity S_{wi} = irreducible water saturation
Berg	$k = 8.4 \times 10^{-2} \times d^2 \phi^{5.1}$	k = permeability (mD) d = grain size (microns) ϕ = porosity
Tortike and Ali	$\frac{k}{k_0} = \frac{\left(1 + \frac{\varepsilon_v}{\phi_0}\right)^3}{1 + \varepsilon_v}$	k = permeability (mD) k_0 = initial permeability (mD) ε_v = volumetric strain ϕ_0 = initial porosity

CHAPTER III

EQUIVALENT PERMEABILITY SIMULATION

3.1 Fractal Discrete Fracture Network Generation

To generate Discrete Fracture Networks (DFNs), fracture geometry information (fracture center distribution, length distribution, orientation, and aperture distribution) is required. These data can be obtained from outcrop maps, FMI log image information, core samplings, and so on. However, because they are scale-dependent data, measured data cannot be directly used in the simulation. In this study, fractal theory was employed to reduce uncertainty and scale discrepancy errors. In a previous study, T. H. Kim and Schechter (2009) developed 2D/3D Fractal Discrete Fracture Network (FDFN) generation codes and calculated fracture porosity. I generated 2D FDFNs using these codes; the generated fracture geometry data were imported to the equivalent permeability simulation codes.

In the FDFN generation codes, the first-order model expressed by Eq. 3.1 was used (Hirata, 1989).

$$N(L) = \frac{\alpha}{D_l} L^{D_c} {l_{\min}}^{-D_l} \quad \text{..... (3.1)}$$

where $N(L)$ is the number of fractures whose length is longer than $l_{\min}$ in a domain of size L, α is the fracture density term, D_l is a fractal dimension of the fracture length distribution, D_c is a fractal dimension of the fracture center distribution, and $l_{\min}$ is the

minimum fracture length. The biggest advantage of this model is that the density term, α, is constant regardless of domains scale (Bour et al., 2002). The fractal dimension of the fracture center distribution was calculated by the pair correlation function as shown in Eq. 3.2 (Darcel et al., 2003).

$$C_2(r) = \frac{2N_p(r)}{N(N-1)} = cr^{D_C} \quad \text{..... (3.2)}$$

The multiplicative cascade method can be used to generate fracture center points following a first-order fractal model. In this process, the parent domain is divided into subdomains; each subdomain has its own probability. Then, the subdomains are iteratively divided into smaller subdomains until the subdomain numbers reach the desired numbers. Even though the random Poisson process is widely used in DFN studies, it cannot sufficiently capture fracture clustering characteristics. The main advantage of the multiplicative cascade method is that it can describe fracture clustering and generate more realistic DFNs.

Fracture orientation can be calculated by using a Fisher distribution (Priest, 1993), and aperture distribution can be generated by using a corrected SRA algorithm (Liu et al., 2004). Fractures generated by an FDFN have their own fracture aperture profiles. Such generated fracture apertures will follow either a constant, normal, or log normal aperture distribution. In this study, I used a normal distribution for the fracture aperture distribution. After calculating fracture porosity, for the sake of simplicity the natural-like aperture distribution was simplified as a set of consecutive rectangular cells. In the averaged aperture distribution cases, a single averaged aperture was calculated and

assigned for each. Each fracture had a different averaged aperture value, depending upon the fracture geometry, but the distribution of the total averaged apertures for each fracture followed a normal distribution.

3.2 Equivalent Continuum Approach

Understanding fluid flow in fractured porous media is quite difficult because of the heterogeneous characteristics of fracture geometry. Usually, the DFN approach is more accurate for fracture flow simulations. However, if a reservoir has very complex and large quantities of fractures, a DFN approach would require high computational effort and much time to simulate fracture flow; in such cases, the Equivalent Continuum (EC) approach may be more suitable.

The Representative Element Volume (REV, see Figure 3.1) is an important assumption to make when using the EC approach (Bear, 1972). REV represents the minimum block size that has constant hydraulic characteristics. To achieve this, the REV must exist for a certain hydraulic property, and derived equivalent properties must have a tensor form to which the EC approach in fractured reservoir conditions can be applied (Long et al., 1982; Bear & Bakhmaṭ, 1991; M. Wang et al., 2002; Min & Jing, 2003; Min et al., 2004). In this study, when discrete fracture network data were used for estimating equivalent permeability, the REV was verified as having a constant directional permeability. To accomplish this verification, the lateral size of the screen windows located at the center of the reservoir domain was expanded from 1 to the domain's side length. Then, the x and y directional equivalent permeability for each

screen window was calculated and plotted. Figure 3.2 shows an example of the screen window expansion for the REV calculation.

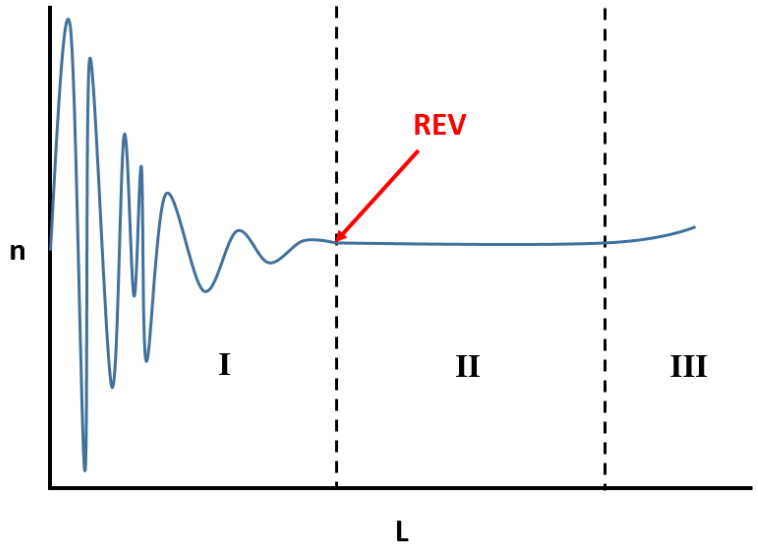

Figure 3.1 Representative Elementary Volume (REV).

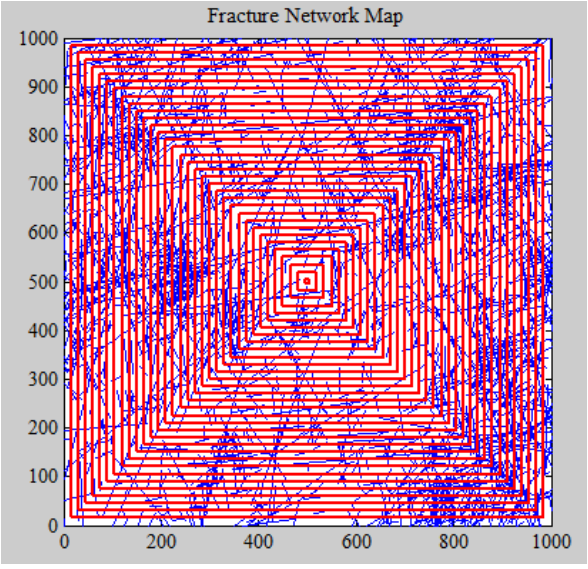

Figure 3.2 REV calculation for a 1000 by 1000 reservoir domain.

3.3 Oda's Equivalent Permeability Calculation Methods

Oda (1982) considered fractured rock mass to be homogeneous, anisotropic porous media. He used permeability tensor notation (the permeability tensor was a function of the fracture geometry and orientation) to propose a stochastic permeability expression using the EC approach. Oda (1985) modified his previous work to develop a tensor permeability model of fractured rock mass. He assumed that a fracture was composed of two parallel planes and that it had a constant aperture t and two unit-normal vectors, +n and -n, as shown in Figure 3.3.

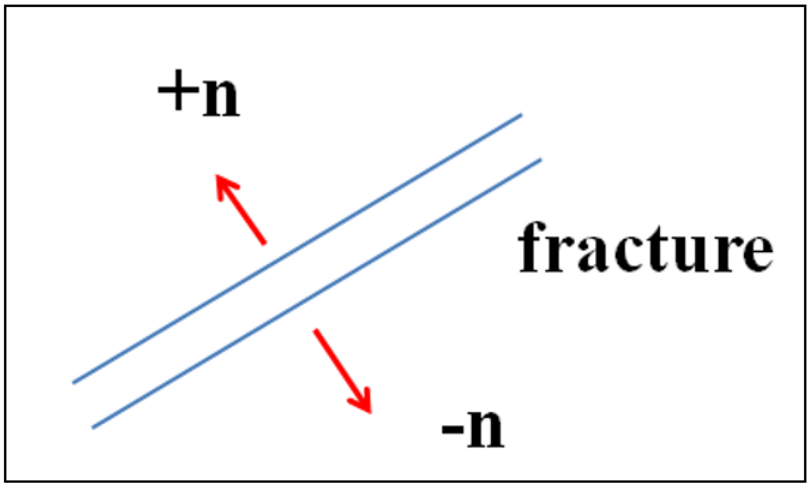

Figure 3.3 Fracture and two unit-normal vectors.

Oda used the cubic law for fluid flow and assumed the volumetric fluid flow rate to be proportional to the aperture cubed, t^3. The fracture tensor can be calculated by Eq. 3.3.

$$P_{ij} = \frac{\pi\rho}{4} \iiint r^2 t^3 n_i n_j E(n,r,t) d\Omega dr dt \quad \text{..... (3.3)}$$

where ρ is the fracture density of the domain, r is the fracture length, t is the fracture aperture, n_i and n_j are two unit normal vectors, $E(n,r,t)$ is a probability density function, and $d\Omega$ is a small solid angle. The fraction $\pi/4$ was used for penny-shaped fractures, but omitted when rectangle-shaped fractures were considered. Oda et al. (1986) proposed Eq. 3.4 to explain the interconnectivity.

$$\lambda = \lambda(F_{ij}) \quad \text{..... (3.4)}$$

where λ is the interconnectivity parameter ranging between 0 and 1/12 and F_{ij} is the fabric tensor. If the fractures are perfectly connected to one another, λ has a value of 1/12. Oda suggested the fabric tensor, F_{ij}, which is related to fracture geometry; he used the fabric tensor to estimate the value for λ. F_{ij} was calculated by Eq. 3.5.

$$F_0 = \frac{\pi\rho}{4} \int r^3 f(r) dr \quad \text{..... (3.5)}$$

Oda et al. (1987) studied the relationship between the interconnectivity parameter, λ, and the first invariant of the fabric tensor, F_0, through an empirical analysis.

$A^{(F)}$ is the anisotropic index and F_0 is the first invariant of the fabric tensor. The variable $A^{(F)} = 1$ for the isotropic fracture condition and $0 < A^{(F)} < 1$ for the

anisotropic fracture condition. The approximation described below was derived by several researchers; I also used this relationship to calculate the interconnectivity parameter λ (Harstad et al., 1996; Brown & Bruhn, 1998).

$$\lambda = 0.0210 + 0.0017 F_0 \quad \text{(3.6)}$$

A modified Oda's method has been used in numerous studies (Harstad et al., 1996; Brown & Bruhn, 1998; M. Wang et al., 2002; Min & Jing, 2003; Min et al., 2004; Du & Wong, 2007a). In this study, I used the modified Oda's algorithm employed by Brown and Bruhn (1998) and Harstad et al. (1996) to estimate the equivalent permeability distributions.

After generating the FDFN and fracture coordinates, the orientation and aperture data were imported into the equivalent permeability simulation codes by using a modified Oda's algorithm. In the codes, the fracture volume, V_f, and fracture porosity, ϕ_f, were calculated by Eqs. 3.7 and 3.8.

$$V_f = \sum_{i=1}^{N} L_f \times t \quad \text{(3.7)}$$

$$\phi_f = \frac{V_f}{A} \quad \text{(3.8)}$$

where N is the total of the fracture numbers in the domain, L_f is the fracture length, t is the fracture aperture, and A is the domain area.

Each fracture angle, θ, was converted into a radian, ω, to calculate the two unit vectors. The two unit vectors were the direction cosines of the fracture pole to the fracture trace, and were calculated by:

$$n_i = -\sin(\omega) = -\sin\left(\frac{\theta \times \pi}{180}\right)$$
$$n_j = \cos(\omega) = \cos\left(\frac{\theta \times \pi}{180}\right) \quad \text{..... (3.9)}$$

Then, the fabric tensor, F_{ij}, was calculated by:

$$F_{ij} = \frac{\sum_{i=1}^{N} L_f^2 \cdot n_i \cdot n_j}{A} \quad \text{..... (3.10)}$$

The fabric tensor had four components in the two-dimensional case, as seen in Eq. 3.11.

$$F_{ij} = \begin{bmatrix} F_{11} & F_{12} \\ F_{21} & F_{22} \end{bmatrix} \quad \text{..... (3.11)}$$

The principle fabric tensors, F_1 and F_2, were calculated by:

$$F_1 = \frac{1}{2}(F_{11} + F_{22}) + \sqrt{{F_{12}}^2 + \frac{1}{4}(F_{11} - F_{22})^2}$$
$$F_2 = \frac{1}{2}(F_{11} + F_{22}) - \sqrt{{F_{12}}^2 + \frac{1}{4}(F_{11} - F_{22})^2} \quad \text{..... (3.12)}$$

Then, the first invariant of the fabric tensor, F_0, and the anisotropic index, $A^{(F)}$, were calculated by:

$$F_0 = F_1 + F_2 \quad \text{..... (3.13)}$$

$$A^{(F)} = \frac{F_1 - F_2}{F_1 + F_2} \quad \text{..... (3.14)}$$

Next, the interconnectivity parameter, λ, was calculated by Eq. 3.6.

The fracture tensor, P_{ij}, was calculated by Eq. 3.15.

$$P_{ij} = \frac{\sum_{i=1}^{N} t^3 \cdot L_f \cdot n_i \cdot n_j}{A} \quad \text{..... (3.15)}$$

The fracture tensor, P_{ij}, also had four components in the two-dimensional case, the same as the fabric tensor. The equivalent permeability tensor, which included the matrix and fracture permeability tensors, was calculated by:

$$k_{ij}^{(f+m)} = \lambda\left(P_{kk}\delta_{ij} - P_{ij}\right) + k^m \delta_{ij} \quad \text{..... (3.16)}$$

where k_{ij}^{f} is the fracture permeability tensor, k_{ij}^{m} is the matrix permeability tensor, and δ_{ij} is the Kronecker delta function. The variable δ_{ij} was 1 if i and j were equal; otherwise, it was 0. The equivalent permeability tensors were expressed in full tensor format:

$$k_{ij}^{(f+m)} = \begin{bmatrix} k_{11} & k_{12} \\ k_{21} & k_{22} \end{bmatrix} \quad \text{..... (3.17)}$$

The deviatoric angle of θ to the horizontal direction was calculated by:

$$\theta = \frac{1}{2}\tan^{-1}\left(\frac{2k_{12}}{k_{11}-k_{22}}\right) \quad \text{..... (3.18)}$$

As shown in Figure 3.4, the original permeability tensor in *x'-y'* coordinates were transformed into new *α-β* coordinates by using a tensor transformation formula (Y. Wang et al., 2013). The transformed permeability tensor was calculated by:

$$k_{\alpha\alpha} = \frac{k_1+k_2}{2} + \frac{k_1-k_2}{2}\cos 2\theta + k_{12}\sin 2\theta$$
$$k_{\beta\beta} = \frac{k_1+k_2}{2} - \frac{k_1-k_2}{2}\cos 2\theta - k_{12}\sin 2\theta$$
$$k_{\alpha\beta} = k_{\beta\alpha} = -\frac{(k_1-k_2)}{2}\sin 2\theta + k_{12}\cos 2\theta \quad \text{..... (3.19)}$$

Using these transformation equations, the x and y directional permeability tensor corresponding to the Cartesian coordinates used in the numerical analysis was then calculated.

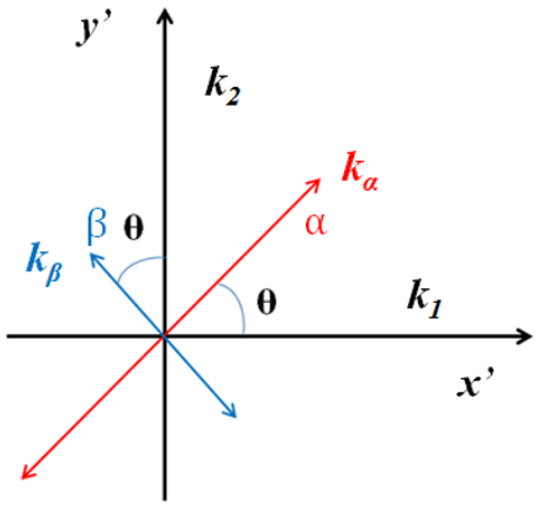

Figure 3.4 Transformation of directional permeability.

3.4 Equivalent Permeability Calculation Procedure

In this study, a modified Oda's method was used to estimate the equivalent directional permeability distribution.

1. One thousand FDFNs were generated by one thousand Monte Carlo simulation runs, and then used to calculated the Cumulative Distribution Function (CDF) plot.
2. A P50 fracture map was selected as a representative reservoir condition because P50 in a CDF plot represents the average condition of a given data range.
3. The domain size was determined from the REV calculation.
4. Directional equivalent permeabilities were calculated by a modified Oda's algorithm; the calculated permeability data were then passed to the iterative coupling simulator.

CHAPTER IV

FINITE DIFFERENCE METHODS (FDM) FOR FLUID FLOW SIMULATION

4.1. Fluid Flow Simulation in Porous Media

The basic governing equations of fluid flow simulation are the mass conservation equation and Darcy's law. In this study, an isothermal, immiscible, and slightly compressible two-phase (oil and water) flow was considered for the fluid flow model (Harlow, 1995; Ing & Xiaoyan, 2002; Tran, 2002; Albinali et al., 2011).

The basic fluid flow assumptions that were used in this study are as follows:

1) The reservoir is an isothermal condition;
2) Darcy's law is valid;
3) No mass change exists between fluid and solid matrices and no chemical reactions occur;
4) Fluid is slightly compressible; and
5) Injection and production wells are treated as source and sink terms in the fluid flow simulation.

4.1.1. 1-Dimensional Single Phase Fluid Flow Equation

I considered the material region to have a volume, V, and be bounded by a surface s; thus, the mass conservation law meant that the rate of mass change of the material region was zero.

$$\frac{dM_{MR}}{dt} = \frac{d}{dt}\int_{MR} \rho \, dV = 0 \quad \text{..... (4.1)}$$

where ρ is the density.

If I selected a small part of the control surface where the velocity was normal and mass was to be conserved, the 1-Dimensional (1D) net inflow through the boundary of the control volume was:

$$-\int_{\Gamma} \rho u \cdot \vec{n} \, ds \quad \text{..... (4.2)}$$

where the negative sign means the net inflow, $\int_{\Gamma}$ is the integral over the control surface, u is the velocity of the fluid and $\vec{n}$ is the outward normal vector.

Therefore, the mass conservation equation in an integral form was:

$$\int_{\Omega} \frac{\partial \rho}{\partial t} dV = -\int_{s} \rho u \cdot \vec{n} \, ds \quad \text{..... (4.3)}$$

Eq. 4.3 of the control surface, when in integral form, was able to be converted into control volume integral form by the divergence theorem.

$$\int_{\Gamma} \rho u \cdot \vec{n} \, ds = \int_{\Omega} \nabla \cdot (\rho u) dV \quad \text{..... (4.4)}$$

where Ω and Γ represent volume and surface, respectively.

The differential form of the governing equation for fluid flow was calculated by rearranging Eqs. 4.3 and 4.4.

$$\int_{\Omega}\left[\frac{\partial \rho}{\partial t}+\nabla\cdot(\rho u)\right]dV=0 \quad \text{..... (4.5)}$$

Because an arbitrary control volume was selected, Eq. 4.5 held true for any control volume. Therefore, the integrand was equal to zero.

$$\frac{\partial \rho}{\partial t}+\nabla\cdot(\rho u)=0 \quad \text{..... (4.6)}$$

Eq. 4.6 was the continuity equation of the fluid flow.

I considered an element of porous material where, for the time being, there was a single phase flow through a unit control volume; the resulting mass balance equation was expressed as:

$$\begin{pmatrix}Flow\ mass\ into\\ element\ @\ x\end{pmatrix}-\begin{pmatrix}Flow\ mass\ out\ of\\ element\ @\ x+dx\end{pmatrix}\\ =\begin{pmatrix}Change\ rate\ of\\ mass\ inside\ element\end{pmatrix}+(sources/sinks) \quad \text{..... (4.7)}$$

The mass accumulation equation was expressed as:

$$\rho\phi A dx=\rho\phi V_{total} \quad \text{..... (4.8)}$$

Then, '*Change rate of mass*' was written as the mass accumulation rate:

$$\int_{\Omega}\frac{\partial}{\partial t}(\phi\rho)dV \quad \text{..... (4.9)}$$

The mass balance equation could then be expressed as:

$$-\int_{\partial\Omega}(\rho u)\cdot\vec{n}\,dA=\int_{\Omega}\tilde{m}\,dV+\int_{\Omega}\frac{\partial}{\partial t}(\phi\rho)dV \quad \text{..... (4.10)}$$

where $\tilde{m}$ is the '*sources/sinks*' term. Eq. 4.10 can be rearranged by using divergent theorem as:

$$\int_{\Omega}\left[-\nabla\cdot(\rho u)-\tilde{m}\right]dV=\int_{\Omega}\frac{\partial}{\partial t}(\phi\rho)dV \quad \text{..... (4.11)}$$

Because an arbitrary control volume was selected, Eq. 4.11 also held true for any control volume. Therefore, the mass balance equation for a single-phase fluid flow in porous media was expressed as:

$$-\nabla\cdot(\rho u)-q=\frac{\partial}{\partial t}(\phi\rho) \quad \text{..... (4.12)}$$

In Eq. 4.12, u was written by Darcy's law, as follows:

$$u=-\frac{1}{\mu}K(\nabla p-\rho g\nabla z) \quad \text{..... (4.13)}$$

Putting Eq. 4.13 into Eq. 4.12 allowed it to be rearranged, as follows:

$$\frac{\partial}{\partial t}(\phi\rho)=\nabla\cdot\left[\frac{\rho}{\mu}K(\nabla p-\rho g\nabla z)\right]-q \quad \text{..... (4.14)}$$

Eq. 4.14 was the single-phase flow equation. For cases of slightly compressible fluid flow, fluid density and porosity were expressed as:

$$\rho = \rho^0 e^{c_f\left(p-p^0\right)} \rightarrow \rho \approx \rho^0\left[1+c_f\left(p-p^0\right)\right]$$
$$\phi = \phi^0 e^{c_R\left(p-p^0\right)} \rightarrow \phi \approx \phi^0\left[1+c_R\left(p-p^0\right)\right] \quad \text{..... (4.15)}$$

where ρ^0 is the density at p^0, c_f is the fluid compressibility, ϕ^0 is the porosity at p^0, c_R is the rock compressibility, and p^0 is the reference pressure. The left-side term in Eq. 4.14 was expanded using a chain rule, as follows:

$$\frac{\partial}{\partial t}(\phi\rho) = \phi\frac{\partial\rho}{\partial t} + \rho\frac{\partial\phi}{\partial t} = \phi\frac{\partial\rho}{\partial p}\frac{\partial p}{\partial t} + \rho\frac{\partial\phi}{\partial p}\frac{\partial p}{\partial t} \quad \text{..... (4.16)}$$

Therefore, Eq. 4.14 could be rearranged as:

$$\left[\phi\frac{\partial\rho}{\partial p} + \rho\frac{\partial\phi}{\partial p}\right]\frac{\partial p}{\partial t} = \nabla\cdot\left[\frac{\rho}{\mu}K\left(\nabla p - \rho g\nabla z\right)\right] - q \quad \text{..... (4.17)}$$

Using $c_f = \frac{1}{\rho}\frac{\partial\rho}{\partial p}$ and $\frac{d\phi}{dp} = \phi^0 c_R$, Eq. 4.17 was then rearranged as:

$$\phi\rho\left[c_f + \frac{\phi^0}{\phi}c_R\right]\frac{\partial p}{\partial t} = \nabla\cdot\left[\frac{\rho}{\mu}K\left(\nabla p - \rho g\nabla z\right)\right] - q \quad \text{..... (4.18)}$$

In these equations, total compressibility, c_t, was written as:

$$c_t = c_f + \frac{\phi^0}{\phi}c_R \quad \text{..... (4.19)}$$

Therefore, Eq. 4.18 became:

$$\phi\rho c_t \frac{\partial p}{\partial t} = \nabla \cdot \left[\frac{\rho}{\mu} K\left(\nabla p - \rho g \nabla z\right) \right] - q \quad \text{..... (4.20)}$$

With the density and formation volume factor at reference pressure, p^0, I could then substitute $\rho = \frac{\rho^0 B^0}{B}$ into Eq. 4.20, and rearrange it as follows:

$$\phi\left(\frac{\rho^0 B^0}{B}\right) c_t \frac{\partial p}{\partial t} = \nabla \cdot \left[\frac{\rho^0 B^0}{\mu B} K\left(\nabla p - \rho g \nabla z\right) \right] - q$$
$$= \frac{\partial p}{\partial t}\left(\frac{\phi c_t}{B}\right) = \nabla \cdot \left[\frac{K}{B\mu}\left(\nabla p - \rho g \nabla z\right) \right] - \frac{q}{\rho^0 B^0} \quad \text{..... (4.21)}$$

where B^0 is the formation volume factor at p^0. The mobility, λ, compressibility term, C, and $\tilde{q}$ were defined as described below:

$$\lambda = \frac{K}{B\mu}$$
$$C = \frac{\phi}{B} c_t$$
$$\frac{q}{\rho^0 B^0} = \tilde{q} \quad \text{..... (4.22)}$$

Using Eq. 4.22, I then obtained the following equation for the 1D slightly compressible single-phase flow equation:

$$C \frac{\partial p}{\partial t} = \frac{\partial}{\partial x}\left[\lambda\left(\nabla p - \rho g \nabla z\right)\right] - \tilde{q} \quad \text{..... (4.23)}$$

4.1.2. 1D Two-Phase Fluid Flow Equation

In the two-phase fluid flow, Darcy's law was expressed as:

$$u_l = -\frac{1}{\mu_l} K_l \left(\nabla p_l - \rho_l \, g \nabla z\right) \quad \text{(4.24)}$$

Here, the subscript l indicates the fluid phase (oil/water). However, since the simultaneous flow of two fluids causes each to interfere with the other, the effective permeability cannot be greater than the absolute permeability, K, of the porous medium. In this case, I used the concept of relative permeability.

$$K_l = k_{rl} K \quad \text{(4.25)}$$

Then, Eq. 4.14 for the single-phase fluid flow equation was written for the two-phase fluid flow, as follows:

$$\frac{\partial}{\partial t}\left(\phi \rho_l S_l\right) = \nabla \cdot \left[\frac{\rho_l}{\mu_l} k_{rl} K \left(\nabla p_l - \rho_l g \nabla z\right)\right] - q_l \quad \text{(4.26)}$$

With the density and formation volume factor for each fluid phase at the reference pressure, p^0, I substituted $\rho_l = \frac{\rho_l^0 B_l^0}{B_l}$ into Eq. 4.26 and rearranged it as:

$$\frac{\partial}{\partial t}\left(\phi \frac{S_l}{B_l}\right) = \nabla \cdot \left[\frac{k_{rl} K}{B_l \mu_l} \left(\nabla p_l - \rho_l g \nabla z\right)\right] - \frac{q_l}{\rho_l^0 B_l^0} \quad \text{(4.27)}$$

Eq. 4.27 was rearranged using the relationships of $\lambda_l = \frac{k_{rl}}{B_l \mu_l}$, $\rho_l \, g_l = \gamma_l$, and $\frac{q_l}{\rho_l^0 B_l^0} = \tilde{q}_l$, as follows:

$$\frac{\partial}{\partial t}\left(\phi\frac{S_l}{B_l}\right)=\nabla\cdot\left[K\lambda_l\left(\nabla p_l-\gamma_l\nabla z\right)\right]-\tilde{q}_l \quad \text{..... (4.28)}$$

The oil and water equations were written in the same manner as the single-phase flow equation.

$$\frac{\partial}{\partial t}\left(\phi\frac{S_o}{B_o}\right)=\nabla\cdot\left[K\lambda_o\left(\nabla p_o-\gamma_o\nabla z\right)\right]-\tilde{q}_o$$
$$\frac{\partial}{\partial t}\left(\phi\frac{S_w}{B_w}\right)=\nabla\cdot\left[K\lambda_w\left(\nabla p_w-\gamma_w\nabla z\right)\right]-\tilde{q}_w \quad \text{..... (4.29)}$$

At that point, I had two equations and four unknowns: S_w, p_w, S_o , and p_o. To solve these equations, I used the relationships between oil and water described below.

$$S_o+S_w=1\Rightarrow S_o=1-S_w \quad \text{..... (4.30)}$$

$$p_c(S_w)=p_o-p_w \;\Rightarrow p_w=p_o-p_c \quad \text{..... (4.31)}$$

Substituting the two equations into Eq. 4.29, I had the following oil and water flow equations:

$$\frac{\partial}{\partial t}\left(\phi\frac{(1-S_w)}{B_o}\right)=\nabla\cdot\left[K\lambda_o\left(\nabla p_o-\gamma_o\nabla z\right)\right]-\tilde{q}_o \quad \text{..... (4.32)}$$

$$\frac{\partial}{\partial t}\left(\phi\frac{S_w}{B_w}\right)=\nabla\cdot\left[K\lambda_w\left(\nabla p_o-\frac{dp_c}{dS_w}\nabla S_w-\gamma_w\nabla z\right)\right]-\tilde{q}_w \quad \text{..... (4.33)}$$

4.2. Finite Difference Methods (FDMs) for Fluid Flow Simulation

4.2.1. Spatial Discretization for FDMs

I began by considering the Taylor series approximation of the derivatives of $p(x,t)$. Once the grid points shown in Figure 4.1 were considered, the first derivative at grid point i was approximated as follows:

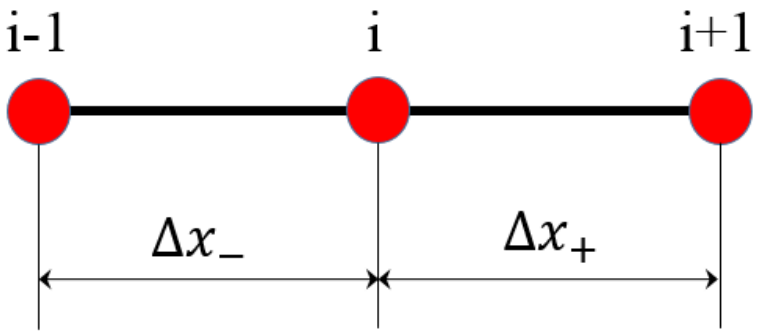

Figure 4.1 Grid points.

4.2.1.1. Forward Difference (FD) Method

If I expanded $u(x_i + \Delta x_{i+}, t)$ around $u(x,t) \rightarrow u_i$, I got:

$$u_{i+1} = u_i + (\Delta x_{i+}) \left.\frac{\partial u}{\partial x}\right|_i + \frac{(\Delta x_{i+})^2}{2!} \left.\frac{\partial^2 u}{\partial x^2}\right|_i + \frac{(\Delta x_{i+})^3}{3!} \left.\frac{\partial^3 u}{\partial x^3}\right|_i + \cdots + HOT \quad \text{..... (4.34)}$$

where HOT represents the higher order terms. Eq. 4.34 was then rearranged as:

$$\left.\frac{\partial u}{\partial x}\right|_i = \frac{u_{i+1} - u_i}{\Delta x_{i+}} - \frac{(\Delta x_{i+})}{2!} \left.\frac{\partial^2 u}{\partial x^2}\right|_i - \frac{(\Delta x_{i+})^2}{3!} \left.\frac{\partial^3 u}{\partial x^3}\right|_i \quad \text{..... (4.35)}$$

Using the first order approximation, I rewrote Eq. 4.35, as follows:

$$\left.\frac{\partial u}{\partial x}\right|_i \approx \frac{\Delta u_i}{\Delta x_{i+}} = \frac{u_{i+1}-u_i}{\Delta x_{i+}} + (R_x)_i \quad \text{..... (4.36)}$$

where $(R_x)_i$ is the local truncation or discretization error.

4.2.1.2. Backward Difference (BD) Method

Similarly, if I expanded $u_i = u_{i-1} + (\Delta x_{i-})$ around $u(x,t) \to u_i$, I got:

$$u_{i-1} = u_i - (\Delta x_{i-})\left.\frac{\partial u}{\partial x}\right|_i + \frac{(\Delta x_{i-})^2}{2!}\left.\frac{\partial^2 u}{\partial x^2}\right|_i - \frac{(\Delta x_{i-})^3}{3!}\left.\frac{\partial^3 u}{\partial x^3}\right|_i + \cdots + HOT \quad \text{..... (4.37)}$$

Eq. 4.37 could then be rearranged as:

$$\left.\frac{\partial u}{\partial x}\right|_i = \frac{u_i - u_{i-1}}{\Delta x_{i-}} + \frac{(\Delta x_{i-})}{2!}\left.\frac{\partial^2 u}{\partial x^2}\right|_i - \frac{(\Delta x_{i-})^2}{3!}\left.\frac{\partial^3 u}{\partial x^3}\right|$$

$$\Rightarrow \left.\frac{\partial u}{\partial x}\right|_i \approx \frac{\Delta u_{i-1}}{\Delta x_{i-}} = \frac{u_i - u_{i-1}}{\Delta x_{i-}} + (R_x)_i \quad \text{..... (4.38)}$$

4.2.1.3. Central Difference (CD) Method

If I added the FD equation, Eq. 4.35, to the BD equation, Eq. 4.37, and assumed that each grid distance, Δx, was the same (for the sake of simplicity), I got the below equation:

$$\left.\frac{\partial u}{\partial x}\right|_i = \frac{u_{i+1}-u_{i-1}}{2\Delta x_i} - \frac{(\Delta x_i)^2}{3!}\left.\frac{\partial^3 u}{\partial x^3}\right|_i - \frac{(\Delta x_i)^4}{5!}\left.\frac{\partial^5 u}{\partial x^5}\right|_i \quad \text{..... (4.39)}$$

If I used the first-order approximation, the CD equation could then be expressed as:

$$\left.\frac{\partial u}{\partial x}\right|_i = \frac{u_{i+1} - u_{i-1}}{2\Delta x_i} + \left(R_x\right)_i \quad \text{..... (4.40)}$$

I used the second-order derivative approximation to rewrite the FD equation, Eq. 4.35, as:

$$\frac{\left(\Delta x_i\right)^2}{2!}\left.\frac{\partial^2 u}{\partial x^2}\right|_i = u_{i+1} - u_i - \left(\Delta x_i\right)\left.\frac{\partial u}{\partial x}\right|_i - \frac{\left(\Delta x_i\right)^3}{3!}\left.\frac{\partial^3 u}{\partial x^3}\right|_i - \frac{\left(\Delta x_i\right)^4}{4!}\left.\frac{\partial^4 u}{\partial x^4}\right|_i \cdots \text{..... (4.41)}$$

$$\left.\frac{\partial^2 u}{\partial x^2}\right|_i = 2 \times \left[\frac{\left(u_{i+1} - u_i\right)}{\left(\Delta x_i\right)^2} - \frac{1}{\left(\Delta x_i\right)}\left.\frac{\partial u}{\partial x}\right|_i - \frac{\left(\Delta x_i\right)}{3!}\left.\frac{\partial^3 u}{\partial x^3}\right|_i - \frac{\left(\Delta x_i\right)^2}{4!}\left.\frac{\partial^4 u}{\partial x^4}\right|_i \cdots\right] \text{..... (4.42)}$$

Similarly, rewrote the BD equation, Eq. 4.37, as:

$$\frac{\left(\Delta x_i\right)^2}{2!}\left.\frac{\partial^2 u}{\partial x^2}\right|_i = u_{i-1} - u_i + \left(\Delta x_i\right)\left.\frac{\partial u}{\partial x}\right|_i + \frac{\left(\Delta x_i\right)^3}{3!}\left.\frac{\partial^3 u}{\partial x^3}\right|_i - \frac{\left(\Delta x_i\right)^4}{4!}\left.\frac{\partial^4 u}{\partial x^4}\right|_i \cdots \text{..... (4.43)}$$

$$\left.\frac{\partial^2 u}{\partial x^2}\right|_i = 2 \times \left[-\frac{\left(u_i - u_{i-1}\right)}{\left(\Delta x_i\right)^2} + \frac{1}{\left(\Delta x_i\right)}\left.\frac{\partial u}{\partial x}\right|_i + \frac{\left(\Delta x_i\right)}{3!}\left.\frac{\partial^3 u}{\partial x^3}\right|_i - \frac{\left(\Delta x_i\right)^2}{4!}\left.\frac{\partial^4 u}{\partial x^4}\right|_i \cdots\right] \text{..... (4.44)}$$

I then added Eq. 4.42 to Eq. 4.44 to rearrange the equation as: I then added Eq. 4.42 to Eq. 4.44 to rearrange the equation as:

$$2 \times \left.\frac{\partial^2 u}{\partial x^2}\right|_i = 2 \times \left[\frac{u_{i+1} - u_i - u_i + u_{i-1}}{\left(\Delta x_i\right)^2} - \frac{\left(\Delta x_i\right)^2}{4!}\left.\frac{\partial^4 u}{\partial x^4}\right|_i - \frac{\left(\Delta x_i\right)^2}{4!}\left.\frac{\partial^4 u}{\partial x^4}\right| \cdots\right]$$

$$\Rightarrow \left.\frac{\partial^2 u}{\partial x^2}\right|_i = \frac{u_{i+1} - 2u_i + u_{i-1}}{\left(\Delta x_i\right)^2} - \frac{2\left(\Delta x_i\right)^2}{4!}\left.\frac{\partial^4 u}{\partial x^4}\right|_i - \frac{2\left(\Delta x_i\right)^4}{6!}\left.\frac{\partial^6 u}{\partial x^6}\right|_i - \cdots$$

$$\Rightarrow \left.\frac{\partial^2 u}{\partial x^2}\right|_i = \frac{\Delta^2 u_i}{(\Delta x_i)^2} + (R_x)_i = \frac{u_{i+1} - 2u_i + u_{i-1}}{(\Delta x_i)^2} + (R_x)_i \quad \text{..... (4.45)}$$

4.2.2. Time Discretization for FDM

4.2.2.1. Forward (Explicit) Method

Using a Taylor series expansion, I expanded $u_i^{n+1} = u(x_i, t + \Delta t)$ around $u(x,t) \rightarrow u_i$, as:

$$u_i^{n+1} = u_i^n + (\Delta t)\left.\frac{\partial u}{\partial t}\right|_i^n + \frac{(\Delta t)^2}{2!}\left.\frac{\partial^2 u}{\partial t^2}\right|_i^n + \frac{(\Delta t)^3}{3!}\left.\frac{\partial^3 u}{\partial t^3}\right|_i^n + \cdots + HOT$$

$$\left.\frac{\partial u}{\partial x}\right|_i^n = \frac{u_i^{n+1} - u_i^n}{\Delta t} - - \frac{\Delta t}{2!}\left.\frac{\partial^2 u}{\partial t^2}\right|_i^n - \frac{(\Delta t)^2}{3!}\left.\frac{\partial^3 u}{\partial t^3}\right|_i^n - \cdots + HOT \quad \text{..... (4.46)}$$

where $u_i^n = u(x_i, t)$ and $u_i^{n+1} = u(x_i, t + \Delta t)$. Using the first-order approximation, Eq. 4.46 could then be rewritten as:

$$\left.\frac{\partial u}{\partial x}\right|_i^n = \frac{\Delta_t u_i}{\Delta t} = \frac{u_i^{n+1} - u_i^n}{\Delta t} + (R_t)_i^n \quad \text{..... (4.47)}$$

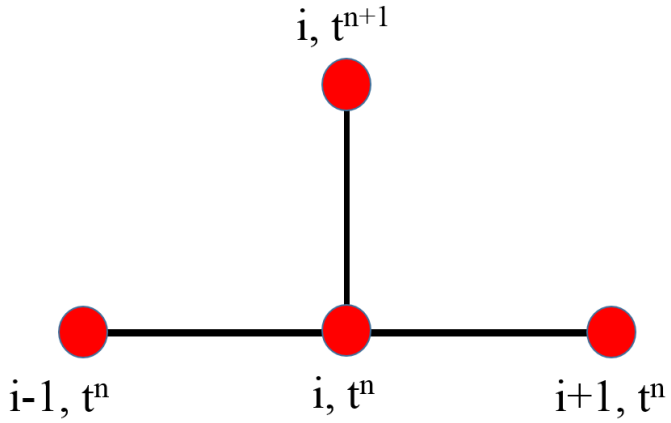

Figure 4.2 Stencil for the explicit time discretization method.

4.2.2.2. Backward (Implicit) Method

Similarly, I expanded $u_i^{n+1} = u_i^n + \Delta t$ around $u(x,t) \rightarrow u_i$, as:

$$u_i^n = u_i^{n+1} - (\Delta t)\frac{\partial u}{\partial t}\bigg|_i^{n+1} + \frac{(\Delta t)^2}{2!}\frac{\partial^2 u}{\partial t^2}\bigg|_i^{n+1} - \frac{(\Delta t)^3}{3!}\frac{\partial^3 u}{\partial t^3}\bigg|_i^{n+1} + \cdots + HOT$$

$$\frac{\partial u}{\partial x}\bigg|_i^{n+1} = \frac{u_i^{n+1} - u_i^n}{\Delta t} + \frac{\Delta t}{2!}\frac{\partial^2 u}{\partial t^2}\bigg|_i^{n+1} - \frac{(\Delta t)^2}{3!}\frac{\partial^3 u}{\partial t^3}\bigg|_i^{n+1} + \cdots + HOT \quad \text{..... (4.48)}$$

where $u_i^n = u(x_i, t)$ and $u_i^n = u_i^{n+1} - \Delta t^{n+1}$. Using the first-order approximation, Eq. 4.48 could then be rewritten as:

$$\frac{\partial u}{\partial x}\bigg|_i^{n+1} = \frac{\Delta_t u_i}{\Delta t} = \frac{u_i^{n+1} - u_i^n}{\Delta t} + (R_t)_i^{n+1} \quad \text{..... (4.49)}$$

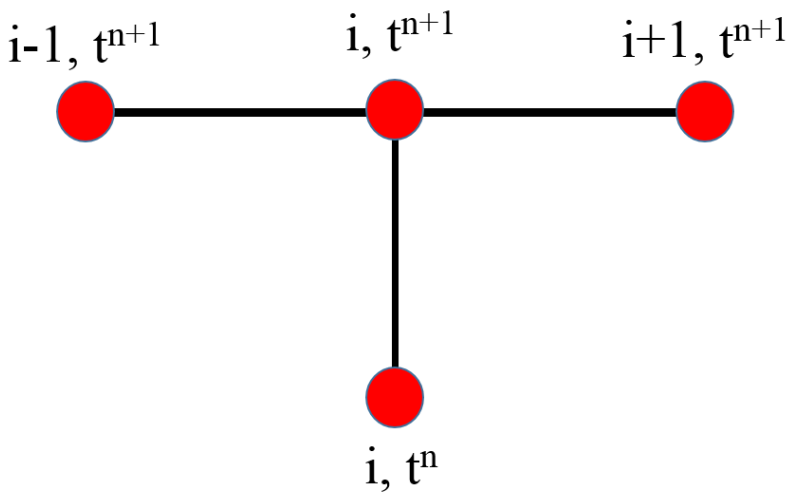

Figure 4.3 Stencil for the implicit time discretization method.

Figures 4.2 and 4.3 show the stencils for the explicit and implicit time discretization methods. In these Figures, i represents the grid position and t^n represents the n^{th} time step.

4.2.3. 3D FDM for Single Phase Fluid Flow

4.2.3.1. Discretization of Space

In this section, I discuss our expansion of the 1D fluid flow equations and FDM formulation into the 3D fluid flow equations. In this study, a 2D iteratively coupled fluid flow FDM and a series of geomechanical FEM simulation codes were developed. To simulate the 2D case, I assumed that Δz was equal to the unit length. The 1D single-

phase fluid flow equation, Eq. 4.14, was rewritten using the relationships of mobility, $\lambda = \frac{K}{B\mu}$, $\rho = \frac{\rho^0 B^0}{B}$, and $\gamma = \rho g$, as:

$$\frac{\partial}{\partial t}\left(\frac{\phi}{B}\right) = \nabla \cdot \left(\lambda\left(\nabla p - \gamma \nabla z\right)\right) - \tilde{q} \quad \text{..... (4.50)}$$

Eq. 4.50 was discretized into a 2D finite difference equation, as follows:

$$\frac{\partial}{\partial t}\left(\frac{\phi}{B}\right) = \frac{\partial}{\partial x}\left(\lambda\left(\frac{\partial p}{\partial x} - \gamma\frac{\partial z}{\partial x}\right)\right) + \frac{\partial}{\partial y}\left(\lambda\left(\frac{\partial p}{\partial y} - \gamma\frac{\partial z}{\partial y}\right)\right) + \frac{\partial}{\partial z}\left(\lambda\left(\frac{\partial p}{\partial z} - \gamma\frac{\partial z}{\partial z}\right)\right) - \tilde{q} \quad \text{..... (4.51)}$$

This single-phase flow Partial Differential Equation (PDE) was discretized into a finite difference equation, as follows:

$$\begin{aligned}\frac{\partial}{\partial t}\left(\frac{\phi}{B}\right)_{i,j,k} \approx{}& \frac{\lambda}{\Delta x}\left(\frac{p_{i+1,j,k} - p_{i,j,k}}{\Delta x_{i+}} - \gamma\frac{z_{i+1,j,k} - z_{i,j,k}}{\Delta x_{i+}}\right) \\ &+ \frac{\lambda}{\Delta x}\left(\frac{p_{i-1,j,k} - p_{i,j,k}}{\Delta x_{i-}} - \gamma\frac{z_{i-1,j,k} - z_{i,j,k}}{\Delta x_{i-}}\right) \\ &+ \frac{\lambda}{\Delta y}\left(\frac{p_{i,j+1,k} - p_{i,j,k}}{\Delta y_{j+}} - \gamma\frac{z_{i,j+1,k} - z_{i,j,k}}{\Delta y_{j+}}\right) \\ &+ \frac{\lambda}{\Delta y}\left(\frac{p_{i,j-1,k} - p_{i,j,k}}{\Delta y_{j-}} - \gamma\frac{z_{i,j-1,k} - z_{i,j,k}}{\Delta y_{j-}}\right) \\ &+ \frac{\lambda}{\Delta z}\left(\frac{p_{i,j,k+1} - p_{i,j,k}}{\Delta z_{k+}} - \gamma\frac{z_{i,j,k+1} - z_{i,j,k}}{\Delta z_{k+}}\right) \\ &+ \frac{\lambda}{\Delta y}\left(\frac{p_{i,j,k-1} - p_{i,j,k}}{\Delta z_{k-}} - \gamma\frac{z_{i,j,k-1} - z_{i,j,k}}{\Delta z_{k-}}\right) - \tilde{q}_{i,j,k} \quad \text{..... (4.52)}\end{aligned}$$

By multiplying both sides by the volume of the grid block , $V_{i,j,k} = \Delta x \Delta y \Delta z$, Eq. 4.52 could then be expressed as follows. Here, $Q_{i,j,k} = \tilde{q}_{i,j,j} V_{i,j,k} = \left(\frac{qV}{\rho^0 B^0} \right)_{i,j,k}$ was the source/sink volumetric rate of the fluid.

$$
\begin{aligned}
V_{i,j,k} \frac{\partial}{\partial t} \left(\frac{\phi}{B} \right)_{i,j,k} \approx & \Delta y \Delta z \lambda \left(\frac{p_{i+1,j,k} - p_{i,j,k}}{\Delta x_{i+}} - \gamma \frac{z_{i+1,j,k} - z_{i,j,k}}{\Delta x_{i+}} \right) \\
& + \Delta y \Delta z \lambda \left(\frac{p_{i-1,j,k} - p_{i,j,k}}{\Delta x_{i-}} - \gamma \frac{z_{i-1,j,k} - z_{i,j,k}}{\Delta x_{i-}} \right) \\
& + \Delta x \Delta z \lambda \left(\frac{p_{i,j+1,k} - p_{i,j,k}}{\Delta y_{j+}} - \gamma \frac{z_{i,j+1,k} - z_{i,j,k}}{\Delta y_{j+}} \right) \\
& + \Delta x \Delta z \lambda \left(\frac{p_{i,j-1,k} - p_{i,j,k}}{\Delta y_{j-}} - \gamma \frac{z_{i,j-1,k} - z_{i,j,k}}{\Delta y_{j-}} \right) \\
& + \Delta x \Delta y \lambda \left(\frac{p_{i,j,k+1} - p_{i,j,k}}{\Delta z_{k+}} - \gamma \right) + \Delta x \Delta y \lambda \left(\frac{p_{i,j,k-1} - p_{i,j,k}}{\Delta z_{k-}} - \gamma \right) - Q_{i,j,k} \quad \text{..... (4.53)}
\end{aligned}
$$

I defined transmissibility as consisting of both geometric and flow parts, as shown below. This explained how the x -directional transmissibility related to the i component. The y - and z - directional transmissibilities were defined using the same methods.

$$
\begin{aligned}
T_{i\pm 1/2,j,k} &= \frac{\Delta y \Delta z}{\Delta x_{i\pm}} \lambda_{i\pm 1/2,j,k} = \frac{A_{i\pm 1/2,j,k}}{\Delta x_{i\pm}} \left(\frac{K}{B\mu} \right)_{i\pm 1/2,j,k} \\
&= \left(\frac{KA}{\Delta x} \right)_{i\pm 1/2,j,k} \left(\frac{1}{B\mu} \right)_{i\pm 1/2,j,k} = \left(T_g \right)_{i\pm 1/2,j,k} \left(T_f \right)_{i\pm 1/2,j,k} \quad \text{..... (4.54)}
\end{aligned}
$$

where T_g and T_f represent the geometric and fluid parts of the transmissibility, respectively. In the FDM, T_g was not changed during the simulation and could be considered a constant, whereas the flow part of transmissibility, T_f, may vary based on the property values of the grid blocks. The interblock permeability, $K_{i+\frac{1}{2}}$, was estimated using a harmonic average, as follows.

$$\frac{\frac{\Delta x_i}{2}+\frac{\Delta x_{i+1}}{2}}{K_{i+\frac{1}{2}}}=\frac{\frac{\Delta x_i}{2}}{K_i}+\frac{\frac{\Delta x_{i+1}}{2}}{K_{i+1}}$$

$$\Rightarrow K_{i+\frac{1}{2}}=\frac{K_iK_{i+1}\left(\frac{\Delta x_i}{2}+\frac{\Delta x_{i+1}}{2}\right)}{K_{i+1}\frac{\Delta x_i}{2}+K_i\frac{\Delta x_{i+1}}{2}} \quad \text{..... (4.55)}$$

T_f was calculated in a similar way:

$$\left(T_f\right)_{i\pm1/2,j,k}=\frac{\left(T_f\right)_{i\pm1,j,k}\left(T_f\right)_{i,j,k}\left(\frac{\Delta x_i}{2}+\frac{\Delta x_{i\pm1}}{2}\right)}{\frac{\left(T_f\right)_{i\pm1,j,k}\Delta x_i}{2}+\frac{\left(T_f\right)_{i,j,k}\Delta x_{i\pm1}}{2}}$$

$$=\frac{\left(T_f\right)_{i\pm1,j,k}\left(T_f\right)_{i,j,k}\left(\Delta x_i+\Delta x_{i\pm1}\right)}{\left(T_f\right)_{i\pm1,j,k}\Delta x_i+\left(T_f\right)_{i,j,k}\Delta x_{i\pm1}} \quad \text{..... (4.56)}$$

Using the transmissibility, the 3D single phase fluid flow finite difference equation was rewritten as:

$$V_{i,j,k}\frac{\partial}{\partial t}\left(\frac{\phi}{B}\right)_{i,j,k}\approx T_{i+1/2,j,k}\left(p_{i+1,j,k}-p_{i,j,k}\right)$$
$$+T_{i-1/2,j,k}\left(p_{i-1,j,k}-p_{i,j,k}\right)+T_{i,j+1/2,k}\left(p_{i,j+1,k}-p_{i,j,k}\right)$$

$$
\begin{aligned}
&+T_{i,j-1/2,k}\left(p_{i,j-1,k}-p_{i,j,k}\right)+T_{i,j,k+1/2}\left(p_{i,j,k+1}-p_{i,j,k}\right)\\
&+T_{i,j,k-1/2}\left(p_{i,j,k-1}-p_{i,j,k}\right)+\gamma\cdot[T_{i+1/2,j,k}\left(z_{i+1,j,k}-z_{i,j,k}\right)\\
&+T_{i-1/2,j,k}\left(z_{i-1,j,k}-z_{i,j,k}\right)+T_{i,j+1/2,k}\left(z_{i,j+1,k}-z_{i,j,k}\right)\\
&+T_{i,j-1/2,k}\left(z_{i,j-1,k}-z_{i,j,k}\right)+T_{i,j,k+1/2}\left(z_{i,j,k+1}-z_{i,j,k}\right)\\
&+T_{i,j,k-1/2}\left(z_{i,j,k-1}-z_{i,j,k}\right)]-Q_{i,j,k} \qquad \text{(4.57)}
\end{aligned}
$$

By arranging the gravity and source/sink terms, I finally arrived at the following space-discretized equation. The sign of the source/sink term was (+) in production, and (-) in injection. Also, I made the gravity term $\sum T\gamma\Delta z$.

$$
\begin{aligned}
&V_{i,j,k}\frac{\partial}{\partial t}\left(\frac{\phi}{B}\right)_{i,j,k}+\sum T\gamma\Delta z+Q_{i,j,k}\\
&\quad\approx T_{i+1/2,j,k}\left(p_{i+1,j,k}-p_{i,j,k}\right)+T_{i-1/2,j,k}\left(p_{i-1,j,k}-p_{i,j,k}\right)\\
&\quad+T_{i,j+1/2,k}\left(p_{i,j+1,k}-p_{i,j,k}\right)+T_{i,j-1/2,k}\left(p_{i,j-1,k}-p_{i,j,k}\right)\\
&\quad+T_{i,j,k+1/2}\left(p_{i,j,k+1}-p_{i,j,k}\right)+T_{i,j,k-1/2}\left(p_{i,j,k-1}-p_{i,j,k}\right) \qquad \text{(4.58)}
\end{aligned}
$$

4.2.3.2. Discretization of Time

The time-derivative term of the equation (the accumulation term) was described by the following methods.

$$
\frac{\partial}{\partial t}\left(\frac{\phi}{B}\right)=\left(\frac{\phi^{n+1}c_f}{B^0}+\frac{c_R\phi^0}{B^n}\right)\frac{\partial p}{\partial t} \qquad \text{(4.59)}
$$

By multiplying the volume of the grid block, V , to this accumulation term, Eq. 4.59 was rearranged as:

$$
V\frac{\partial}{\partial t}\left(\frac{\phi}{B}\right)=V\left(\frac{\phi^{n+1}c_f}{B^0}+\frac{c_R\phi^0}{B^n}\right)\frac{\partial p}{\partial t}=V\left(\frac{\phi^0c_R}{B^{n+1}}+\frac{c_f\phi^n}{B^n}\right)\frac{\partial p}{\partial t} \qquad \text{(4.60)}
$$

Eq. 4.60 was rewritten by using $C_{i,j,k}$, as follows:

$$V\left(\frac{\phi^0 c_R}{B^{n+1}}+\frac{c_f\phi^n}{B^n}\right)\frac{\partial p}{\partial t}\approx V_{i,j,k}\left(\frac{\phi^{n+1}c_f}{B^0}+\frac{c_R\phi^0}{B^n}\right)_{i,j,k}\frac{p_{i,j,k}^{n+1}-p_{i,j,k}^n}{\Delta t}$$
$$=V_{i,j,k}\left(\frac{\phi^0 c_R}{B^{n+1}}+\frac{c_f\phi^n}{B^n}\right)_{i,j,k}\frac{p_{i,j,k}^{n+1}-p_{i,j,k}^n}{\Delta t}=C_{i,j,k}V_{i,j,k}\frac{p_{i,j,k}^{n+1}-p_{i,j,k}^n}{\Delta t} \quad \text{..... (4.61)}$$

Using Eq. 4.61, the 3D single-phase fluid flow finite difference equation could then be expressed as:

$$C_{i,j,k}V_{i,j,k}\frac{p_{i,j,k}^{n+1}-p_{i,j,k}^n}{\Delta t}+\sum T\gamma\Delta z+Q_{i,j,k}$$
$$=T_{i+1/2,j,k}\left(p_{i+1,j,k}-p_{i,j,k}\right)+T_{i-1/2,j,k}\left(p_{i-1,j,k}-p_{i,j,k}\right)$$
$$+T_{i,j+1/2,k}\left(p_{i,j+1,k}-p_{i,j,k}\right)+T_{i,j-1/2,k}\left(p_{i,j-1,k}-p_{i,j,k}\right)$$
$$+T_{i,j,k+1/2}\left(p_{i,j,k+1}-p_{i,j,k}\right)+T_{i,j,k-1/2}\left(p_{i,j,k-1}-p_{i,j,k}\right) \quad \text{..... (4.62)}$$

4.2.3.3. Source/Sink Term

If the bottomhole pressure was given instead of the production or injection rate, I were able to calculate the pressure of the block, including the well, by using Peaceman's (1978) equation:

$$q_{i,j,k}=(WI)_{i,j,k}\lambda_{i,j,k}\left[p_{i,j,k}-\left(p_{wf}\right)_{i,j,k}\right] \quad \text{..... (4.63)}$$

In this equation, WI is the well index; it was calculated by y:

$$(WI)_{i,j,k}=\frac{2\pi\Delta z}{\ln(r_e/r_w)+s} \quad \text{..... (4.64)}$$

where r_e is the equivalent radius, r_w is the well radius, and s is the skin factor. For the anisotropic media, r_e was calculated by:

$$r_e = 0.28 \frac{\sqrt{\left(\frac{K_y}{K_x}\right)^{1/2}(\Delta x)^2 + \left(\frac{K_x}{K_y}\right)^{1/2}(\Delta y)^2}}{\left(\frac{K_y}{K_x}\right)^{1/4} + \left(\frac{K_x}{K_y}\right)^{1/4}} \quad \text{..... (4.65)}$$

4.2.3.4. Set-up Matrix Equat**ion**

$\sum T_{i,j,k}$ was expressed as:

$$\sum T_{i,j,k} = T_{i+1/2\,j,k} + T_{i-1/2\,j,k} + T_{i,j+1/2,k} + T_{i,j-1/2,k} + T_{i,j,k+1/2} + T_{i,j,k-1/2} \quad \text{..... (4.66)}$$

Using Eq. 4.66, the 3D single-phase fluid flow finite difference equation was expressed simply, as:

$$\begin{aligned} & C_{i,j,k} V_{i,j,k} \frac{p_{i,j,k}^{n+1} - p_{i,j,k}^{n}}{\Delta t} + \sum T \gamma \Delta z + Q_{i,j,k} \\ & = T_{i+1/2,j,k} p_{i+1,j,k} + T_{i-1/2,j,k} p_{i-1,j,k} + T_{i,j+1/2,k} p_{i,j+1,k} \\ & + T_{i,j-1/2,k} p_{i,j-1,k} + T_{i,j,k+1/2} p_{i,j,k+1} + T_{i,j,k-1/2} p_{i,j,k-1} - p_{i,j,k} \sum T_{i,j,k} \end{aligned} \quad \text{..... (4.67)}$$

For example, afterif we considering the 3D grid block shown in Figure 4.4, I were able to rewrite Eq. 4.67 in matrix form using the following notation. The primary variable vector, X, had entries of $\lfloor p_{i,j,k} \rfloor$.

$$C = -\left(T_{i-\frac{1}{2}} + T_{i+\frac{1}{2}} + T_{j-\frac{1}{2}} + T_{j+\frac{1}{2}} + T_{k-\frac{1}{2}} + T_{k+\frac{1}{2}}\right)$$
$$E = T_{i+1/2,j,k},\ W = T_{i-1/2,j,k},\ S = T_{i,j+1/2,k},$$

$$N = T_{i,j-1/2,k},\ B = T_{i,j,k+1/2},\ T = T_{i,j,k-1/2} \quad \text{..... (4.68)}$$

The transmissibility matrix, T, and the accumulation matrix, D, were expressed as:

$$TX = \begin{bmatrix} C & E & & S & & & & & & B & & \\ W & C & E & & S & & & & & & B & \\ & W & C & & & S & & & & & & B \\ N & & & C & E & & S & & & & & \\ & N & & W & C & E & & S & & & & \\ & & & & & \ddots & & & & & & \\ & & & & & & \ddots & & & & & \\ & & & N & & & W & C & E & & S & \\ & & & & N & & & W & C & & & S \\ T & & & & & N & & & W & C & E & \\ & T & & & & & N & & & W & C & E \\ & & T & & & & & N & & & W & C \end{bmatrix} \begin{bmatrix} p \\ \\ \\ \\ \\ \vdots \\ \\ \\ \\ \\ \\ p \end{bmatrix} \quad \text{..... (4.69)}$$

$$D\frac{dX}{dt} = \begin{bmatrix} CV & & & & & & & & & & & \\ & CV & & & & & & & & & & \\ & & CV & & & & & & & & & \\ & & & CV & & & & & & & & \\ & & & & \ddots & & & & & & & \\ & & & & & CV & & & & & & \\ & & & & & & CV & & & & & \\ & & & & & & & CV & & & & \\ & & & & & & & & CV & & & \\ & & & & & & & & & CV & & \\ & & & & & & & & & & CV & \end{bmatrix} \begin{bmatrix} \frac{dp}{dt} \\ \\ \\ \\ \\ \vdots \\ \\ \\ \\ \\ \\ \frac{dp}{dt} \end{bmatrix} \quad \text{..... (4.70)}$$

The transmissibility matrix had either a tri-diagonal (1D case), penta-diagonal (2D case), or hepta-diagonal (3D case) matrix. The accumulation matrix had a diagonal matrix. These matrix equations were simplified as:

$$Tp = D\frac{dp}{dt} + Q + G \quad \text{..... (4.71)}$$

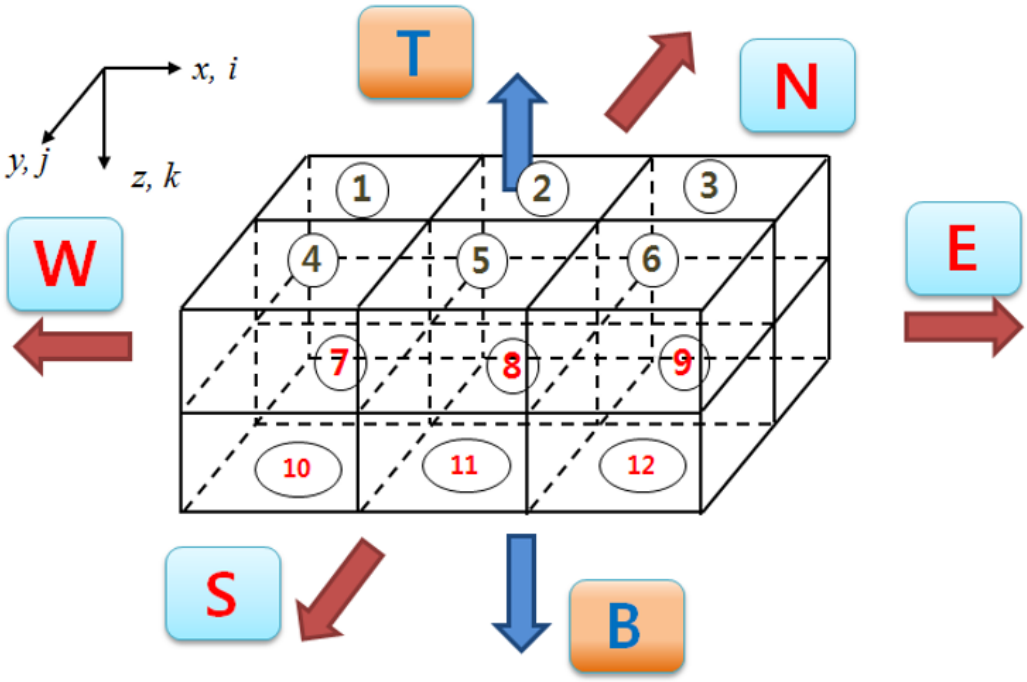

Figure 4.4 3D grid block.

4.2.3.5. Computation of the Primary Variables

In this study, we used the Newton-Raphson iteration (fully implicit) method to solve the fluid flow equation. Through this method, Eq. 4.71 was rewritten as:

$$T^{n+1}X^{n+1} = D^{n+1}\frac{X^{n+1} - X^{n}}{\Delta t} + G^{n+1} + Q^{n+1}$$

$$R\left(X^{n+1}\right) = T^{n+1}X^{n+1} - \left(D^{n+1}\frac{X^{n+1} - X^{n}}{\Delta t} + G^{n+1} + Q^{n+1}\right) \quad \text{..... (4.72)}$$

$R\left(X^{n+1}\right)$ was the residual; it was calculated through the Newton-Raphson iteration, X^{n+1}, which made the residual zero.

$$
\begin{aligned}
X_0^{n+1} &= X^n \quad \Rightarrow \textit{First guess of } X^{n+1} \\
X_1^{n+1} &= X_0^{n+1} - \frac{R(X_0^{n+1})}{R'(X_0^{n+1})} \\
&\vdots \\
X_{k+1}^{n+1} &= X_k^{n+1} - \frac{R(X_k^{n+1})}{R'(X_k^{n+1})}
\end{aligned}
\qquad \text{..... (4.73)}
$$

If I allowed the Jacobian to be $J = R'(X_k^{n+1})$, and $\delta = X_{k+1}^{n+1} - X_k^{n+1}$, then I were able to rewrite Eq. 4.73, as follows:

$$J\delta = -R \qquad \text{..... (4.74)}$$

Eq. 4.74 was calculated through matrix-solving ($\delta = -J \setminus R$) in Matlab®.

After getting δ by solving the matrix equation, I found the new X^{n+1} by $X_{k+1}^{n+1} = X_k^{n+1} + \delta$. The Newton-Raphson iteration was repeated until the residual was below the given tolerance level. If the primary variable, X, converged to X_{k+1}^{n+1}, then X became the solution to this time step $(n+1)$.

The residual for the single-phase fluid flow was:

$$
\begin{aligned}
R\left(p_{i,j,k}^{n+1}\right) = {} & T_{i+1/2,j,k}^{n+1} p_{i+1,j,k}^{n+1} + T_{i-1/2,j,k}^{n+1} p_{i-1,j,k}^{n+1} + T_{i,j+1/2,k}^{n+1} p_{i,j+1,k}^{n+1} \\
& + T_{i,j-1/2,k}^{n+1} p_{i,j-1,k}^{n+1} + T_{i,j,k+1/2}^{n+1} p_{i,j,k+1}^{n+1} + T_{i,j,k-1/2}^{n+1} p_{i,j,k-1}^{n+1} \\
& - p_{i,j,k}^{n+1} \sum T_{i,j,k}^{n+1} - \left(\frac{\phi^{n+1} c_f}{B^0} + \frac{c_R \phi^0}{B^n} \right)_{i,j,k}^{n+1} V_{i,j,k}^{n+1} \frac{p_{i,j,k}^{n+1} - p_{i,j,k}^{n}}{\Delta t} \\
& - \sum T^{n+1} \gamma \Delta z - Q_{i,j,k}^{n+1}
\end{aligned}
\qquad \text{..... (4.75)}
$$

In the single-phase fluid flow, the Jacobian matrix had the same matrix format (hepta-diagonal) as the transmissibility matrix, T.

$$J = \begin{bmatrix}
C & E & & S & & & & & & B & & \\
W & C & E & & S & & & & & & B & \\
 & W & C & & & S & & & & & & B \\
N & & & C & E & & S & & & & & \\
 & N & & W & C & E & & S & & & & \\
 & & & & & \ddots & & & & & & \\
 & & & & & & \ddots & & & & & \\
 & & & N & & & W & C & E & & S & \\
 & & & & N & & & W & C & & & S \\
T & & & & & N & & & W & C & E & \\
 & T & & & & & N & & & W & C & E \\
 & & T & & & & & N & & & W & C
\end{bmatrix} \quad \text{..... (4.76)}$$

In the same row of the Jacobian matrix, I wrote the entries as follows.

$$\begin{aligned}
W &= \frac{\partial T^{n+1}_{i-1/2,j,k}}{\partial p^{n+1}_{i-1,j,k}}\left(p^{n+1}_{i-1,j,k} - p^{n+1}_{i,j,k}\right) + T^{n+1}_{i-1/2,j,k} - \frac{\partial T^{n+1}_{i-1/2,j,k}}{\partial p^{n+1}_{i-1,j,k}}\gamma\left(z_{i-1,j,k} - z_{i,j,k}\right) \\
E &= \frac{\partial T^{n+1}_{i+1/2,j,k}}{\partial p^{n+1}_{i+1,j,k}}\left(p^{n+1}_{i+1,j,k} - p^{n+1}_{i,j,k}\right) + T^{n+1}_{i+1/2,j,k} - \frac{\partial T^{n+1}_{i+1/2,j,k}}{\partial p^{n+1}_{i+1,j,k}}\gamma\left(z_{i+1,j,k} - z_{i,j,k}\right) \\
N &= \frac{\partial T^{n+1}_{i,j-1/2,k}}{\partial p^{n+1}_{i,j-1,k}}\left(p^{n+1}_{i,j-1,k} - p^{n+1}_{i,j,k}\right) + T^{n+1}_{i,j-1/2,k} - \frac{\partial T^{n+1}_{i,j-1/2,k}}{\partial p^{n+1}_{i,j-1,k}}\gamma\left(z_{i,j-1,k} - z_{i,j,k}\right) \\
S &= \frac{\partial T^{n+1}_{i,j+1/2,k}}{\partial p^{n+1}_{i,j+1,k}}\left(p^{n+1}_{i,j+1,k} - p^{n+1}_{i,j,k}\right) + T^{n+1}_{i,j+1/2,k} - \frac{\partial T^{n+1}_{i,j+1/2,k}}{\partial p^{n+1}_{i,j+1,k}}\gamma\left(z_{i,j+1,k} - z_{i,j,k}\right) \\
T &= \frac{\partial T^{n+1}_{i,j,k-1/2}}{\partial p^{n+1}_{i,j,k-1}}\left(p^{n+1}_{i,j,k-1} - p^{n+1}_{i,j,k}\right) + T^{n+1}_{i,j,k-1/2} - \frac{\partial T^{n+1}_{i,j,k-1/2}}{\partial p^{n+1}_{i,j,k-1}}\gamma\left(z_{i,j,k-1} - z_{i,j,k}\right) \\
B &= \frac{\partial T^{n+1}_{i,j,k+1/2}}{\partial p^{n+1}_{i,j,k+1}}\left(p^{n+1}_{i,j,k+} - p^{n+1}_{i,j,k}\right) + T^{n+1}_{i,j,k+1/2} - \frac{\partial T^{n+1}_{i,j,k+1/2}}{\partial p^{n+1}_{i,j,k+1}}\gamma\left(z_{i,j,k+1} - z_{i,j,k}\right) \quad \text{..... (4.77)}
\end{aligned}$$

Additionally, the center component, C, was expressed as:

$$
\begin{aligned}
C = \frac{\partial R_{i,j,k}}{\partial p_{i,j,k}} &= \frac{\partial T_{i+1/2,j,k}^{n+1}}{\partial p_{i,j,k}^{n+1}} p_{i+1,j,k}^{n+1} + \frac{\partial T_{i-1/2,j,k}^{n+1}}{\partial p_{i,j,k}^{n+1}} p_{i-1,j,k}^{n+1} \\
&+ \frac{\partial T_{i,j+1/2,k}^{n+1}}{\partial p_{i,j,k}^{n+1}} p_{i,j+1,k}^{n+1} + \frac{\partial T_{i,j-1/2,k}^{n+1}}{\partial p_{i,j,k}^{n+1}} p_{i,j-1,k}^{n+1} \\
&+ \frac{\partial T_{i,j,k+1/2}^{n+1}}{\partial p_{i,j,k}^{n+1}} p_{i,j,k+1}^{n+1} + \frac{\partial T_{i,j,k-1/2}^{n+1}}{\partial p_{i,j,k}^{n+1}} p_{i,j,k-1}^{n+1} - \sum T_{i,j,k}^{n+1} - p_{i,j,k}^{n+1} \sum \frac{\partial T_{i,j,k}^{n+1}}{\partial p_{i,j,k}^{n+1}} \\
&- \frac{V_{i,j,k}^{n+1}}{\Delta t} \left(\phi^{n+1} c_f b^0 + c_R \phi^0 b^n \right)_{i,j,k}^{n+1} - \frac{V_{i,j,k}^{n+1}}{\Delta t} \left(c_f b^0 \right) \frac{\partial \phi^{n+1}}{\partial p_{i,j,k}^{n+1}} \left(p_{i,j,k}^{n+1} - p_{i,j,k}^{n} \right) \\
&- \left(\sum \frac{\partial \left(T^{n+1} \gamma \right)}{\partial p_{i,j,k}^{n+1}} \Delta z \right) - \frac{\partial q_{i,j,k}^{n+1}}{\partial p_{i,j,k}^{n+1}} \qquad \text{(4.78)}
\end{aligned}
$$

4.2.4. 3D FDM for Two-Phase Fluid Flow

4.2.4.1. Discretization of Space

The 3D two-phase flow equation was discretized in the same manner as was used for the derivation of the single-phase fluid flow equation.

1) Oil flow equation:

The oil flow equation, Eq. 4.32, was rewritten as:

$$
\begin{aligned}
V \frac{\partial}{\partial t} \left(\phi \frac{S_o}{B_o} \right) &= V \nabla \cdot \left(K \lambda_o \left(\nabla p_o - \gamma_o \nabla z \right) \right) - Q_o \\
&\approx (T_o)_{i+1/2,j,k} \left[(p_o)_{i+1,j,k} - (p_o)_{i,j,k} \right] + (T_o)_{i-1/2,j,k} \left[(p_o)_{i-1,j,k} - (p_o)_{i,j,k} \right] \\
&+ (T_o)_{i,j+1/2,k} \left[(p_o)_{i,j+1,k} - (p_o)_{i,j,k} \right] + (T_o)_{i,j-1/2,k} \left[(p_o)_{i,j-1,k} - (p_o)_{i,j,k} \right] \\
&+ (T_o)_{i,j,k+1/2} \left[(p_o)_{i,j,k+1} - (p_o)_{i,j,k} \right] + (T_o)_{i,j,k-1/2} \left[(p_o)_{i,j,k-1} - (p_o)_{i,j,k} \right] \\
&- \sum T_o \gamma_o \Delta z - Q_{oi,j,k} \qquad \text{(4.79)}
\end{aligned}
$$

Here, the transmissibility of oil, T_o, was calculated in the same manner as the single-phase fluid flow. The only difference was that relative permeability was used for the two-phase fluid flow equation.

$$\left(T_o\right)_{i\pm1/2,j,k} = \frac{\Delta y \Delta z}{\Delta x_{i\pm}} \lambda_{i\pm1/2,j,k} = \frac{A_{i\pm1/2,j,k}}{\Delta x_{i\pm}} \left(\frac{Kk_o}{B_o \mu_o} \right)_{i\pm1/2,j,k}$$
$$= \left(\frac{KA}{\Delta x} \right)_{i\pm1/2,j,k} \left(\frac{k_o}{B_o \mu_o} \right)_{i\pm1/2,j,k} = \left(T_{o,g}\right)_{i\pm1/2,j,k} \left(T_{o,f}\right)_{i\pm1/2,j,k} \quad \text{..... (4.80)}$$

$T_{o,f}$ was calculated using the harmonic average, as was the single-phase flow case.

$$\left(T_{o,f}\right)_{i\pm1/2,j,k} == \frac{\left(T_{o,f}\right)_{i\pm1,j,k} \left(T_{o,f}\right)_{i,j,k} \left(\Delta x_i + \Delta x_{i\pm1}\right)}{\left(T_{o,f}\right)_{i\pm1,j,k} \Delta x_i + \left(T_{o,f}\right)_{i,j,k} \Delta x_{i\pm1}} \quad \text{..... (4.81)}$$

2) Water flow equation:

The water flow equation, Eq. 4.33, was rewritten using $\frac{dp_c}{dS_w} = p_c'$, as follows:

$$V \frac{\partial}{\partial t} \left(\phi \frac{S_w}{B_w} \right) = V \nabla \cdot \left[K \lambda_w \left(\nabla p_o - \frac{dp_c}{dS_w} \nabla S_w - \gamma_w \nabla z \right) \right] - Q_w$$
$$\approx \left(T_w\right)_{i+1/2,j,k} \left[\left(p_o\right)_{i+1,j,k} - \left(p_o\right)_{i,j,k} \right] + \left(T_w\right)_{i-1/2,j,k} \left[\left(p_o\right)_{i-1,j,k} - \left(p_o\right)_{i,j,k} \right]$$
$$+ \left(T_w\right)_{i,j+1/2,k} \left[\left(p_o\right)_{i,j+1,k} - \left(p_o\right)_{i,j,k} \right] + \left(T_w\right)_{i,j-1/2,k} \left[\left(p_o\right)_{i,j-1,k} - \left(p_o\right)_{i,j,k} \right]$$
$$+ \left(T_w\right)_{i,j,k+1/2} \left[\left(p_o\right)_{i,j,k+1} - \left(p_o\right)_{i,j,k} \right] + \left(T_w\right)_{i,j,k-1/2} \left[\left(p_o\right)_{i,j,k-1} - \left(p_o\right)_{i,j,k} \right]$$
$$- \left(T_w p_c'\right)_{i+1/2,j,k} \left[\left(S_w\right)_{i+1,j,k} - \left(S_w\right)_{i,j,k} \right] - \left(T_w p_c'\right)_{i-1/2,j,k} \left[\left(S_w\right)_{i-1,j,k} - \left(S_w\right)_{i,j,k} \right]$$
$$- \left(T_w p_c'\right)_{i,j+1/2,k} \left[\left(S_w\right)_{i,j+1,k} - \left(S_w\right)_{i,j,k} \right] - \left(T_w p_c'\right)_{i,j-1/2,k} \left[\left(S_w\right)_{i,j-1,k} - \left(S_w\right)_{i,j,k} \right]$$
$$- \left(T_w p_c'\right)_{i,j,k+1/2} \left[\left(S_w\right)_{i,j,k+1} - \left(S_w\right)_{i,j,k} \right] - \left(T_w p_c'\right)_{i,j,k-1/2} \left[\left(S_w\right)_{i,j,k-1} - \left(S_w\right)_{i,j,k} \right]$$
$$- \sum T_w \gamma_w \Delta z + q_{wi,j,k} \quad \text{..... (4.82)}$$

As with the oil flow equation, the water transmissibility, T_w, was calculated as:

$$(T_w)_{i\pm1/2,j,k} = \left(\frac{KA}{\Delta x}\right)_{i\pm1/2,j,k}\left(\frac{k_{rw}}{B_w\mu_w}\right)_{i\pm1/2,j,k} = (T_{w,g})_{i\pm1/2,j,k}(T_{w,f})_{i\pm1/2,j,k} \quad \text{..... (4.83)}$$

4.2.4.2. Discretization of Time

1) Oil flow equation:

For the sake of simplicity, $b_o = \frac{1}{B_o}$ was the defined and time-derivative term for the oil flow equation (the accumulation term); it was rearranged as:

$$\begin{aligned}
V\frac{\partial}{\partial t}\left(\phi\frac{S_o}{B_o}\right) &\approx \frac{V}{\Delta t}\left[(\phi b_o S_o)^{n+1} - (\phi b_o S_o)^n\right] \\
&= \frac{V}{\Delta t}\left[(\phi b_o)^{n+1}\left(S_o^{n+1} - S_o^n\right) - S_o^n\left((\phi b_o)^{n+1} - (\phi b_o)^n\right)\right] \\
&= V(\phi b_o)^{n+1}\Delta_t S_o + VS_o^n\Delta_t(\phi b_o) \\
&= V(\phi b_o)^{n+1}\Delta_t S_o + \frac{VS_o^n}{\Delta t}\left[(\phi b_o)^{n+1} - (\phi b_o)^n + b_o^{n+1}\phi^n - b_o^{n+1}\phi^n\right] \\
&= V(\phi b_o)^{n+1}\Delta_t S_o + VS_o^n\left[b_o^{n+1}\Delta_t\phi + \phi^n\Delta_t b_o\right] \quad \text{..... (4.84)}
\end{aligned}$$

or,
$$\begin{aligned}
&= V(\phi b_o)^{n+1}\Delta_t S_o + \frac{VS_o^n}{\Delta t}\left[(\phi b_o)^{n+1} - (\phi b_o)^n + \phi^{n+1}b_o{}^n - \phi^{n+1}b_o{}^n\right] \\
&= V(\phi b_o)^{n+1}\Delta_t S_o + VS_o^n\left[\phi^{n+1}\Delta_t b_o + b_o{}^n\Delta_t\phi\right] \quad \text{..... (4.85)}
\end{aligned}$$

Using the following relationships,

$$S_o = 1 - S_w$$

$$\frac{\partial\phi}{\partial t} = \frac{\partial\phi}{\partial p_o}\frac{\partial p_o}{\partial t} = \phi'\frac{\partial p_o}{\partial t}, \quad \frac{\partial b_o}{\partial t} = \frac{\partial b_o}{\partial p_o}\frac{\partial p_o}{\partial t} = b_o'\frac{\partial p_o}{\partial t} \quad \text{..... (4.86)}$$

Eqs. 4.84 and 4.85 were rearranged as:

$$V\frac{\partial}{\partial t}\left(\phi\frac{S_o}{B_o}\right)\approx V(\phi b_o)^{n+1}\Delta_t(1-S_w)+V(1-S_w)^n\left[b_o^{n+1}\Delta_t\phi+\phi^n\Delta_t b_o\right]$$

$$=-V(\phi b_o)^{n+1}\Delta_t S_w+V(1-S_w)^n\left[b_o^{n+1}\phi'+\phi^n b_o'\right]\Delta_t p_o \quad \text{..... (4.87)}$$

or,
$$=-V(\phi b_o)^{n+1}\Delta_t S_w+V(1-S_w)^n\left[\phi_o^{n+1}b'+b_o{}^n\phi'\right]\Delta_t p_o \quad \text{..... (4.88)}$$

Consequently, Eqs. 4.87 and 4.88 could then be expressed as:

$$-V(\phi b_o)^{n+1}\Delta_t S_w+V(1-S_w)^n\left[b_o^{n+1}\phi'+\phi^n b_o'\right]\Delta_t p_o$$

or,
$$-V(\phi b_o)^{n+1}\Delta_t S_w+V(1-S_w)^n\left[\phi_o^{n+1}b'+b_o{}^n\phi'\right]\Delta_t p_o$$

$$=(T_o)_{i+1/2,j,k}\left[(p_o)_{i+1,j,k}-(p_o)_{i,j,k}\right]+(T_o)_{i-1/2,j,k}\left[(p_o)_{i-1,j,k}-(p_o)_{i,j,k}\right]$$

$$+(T_o)_{i,j+1/2,k}\left[(p_o)_{i,j+1,k}-(p_o)_{i,j,k}\right]+(T_o)_{i,j-1/2,k}\left[(p_o)_{i,j-1,k}-(p_o)_{i,j,k}\right]$$

$$+(T_o)_{i,j,k+1/2}\left[(p_o)_{i,j,k+1}-(p_o)_{i,j,k}\right]+(T_o)_{i,j,k-1/2}\left[(p_o)_{i,j,k-1}-(p_o)_{i,j,k}\right]$$

$$-\sum T_o\gamma_o\Delta z-Q_{oi,j,k} \quad \text{..... (4.89)}$$

2) Water flow equation:

In the same manner as the oil flow equation, the water flow equation was expressed using the following relationships:

$$\frac{\partial b_w}{\partial t}=\frac{\partial b_w}{\partial p_w}\frac{\partial p_w}{\partial t}=b_w'\frac{\partial p_w}{\partial t}$$

$$\Delta_t p_w=\Delta_t p_o-\Delta_t p_c=\Delta_t p_o-p_c'\Delta_t S_w \quad \text{..... (4.90)}$$

$$V\frac{\partial}{\partial t}\left(\phi\frac{S_w}{B_w}\right)\approx V(\phi b_w)^{n+1}\Delta_t S_w+VS_w^n\left[b_w^{n+1}\Delta_t\phi+\phi^n\Delta_t b_w\right]$$

$$=V(\phi b_w)^{n+1}\Delta_t S_w+VS_w^n\left[b_w^{n+1}\phi'\Delta_t p_o+\phi^n b_w'\Delta_t p_w\right]$$

$$= V(\phi b_w)^{n+1}\Delta_t S_w + VS_w^n\left[b_w^{n+1}\phi'\Delta_t p_o + \phi^n b_w'(\Delta_t p_o - p_c'\Delta_t S_w)\right]$$

$$= V\left[(\phi b_w)^{n+1} - \phi^n S_w^n b_w'\, p_c'\right]\Delta_t S_w + V\left[S_w^n b_w^{n+1}\phi' + S_w^n\phi^n b_w'\right]\Delta_t p_o \quad \text{..... (4.91)}$$

or,
$$= V(\phi b_w)^{n+1}\Delta_t S_w + VS_w^n\left[\phi^{n+1}\Delta_t b_w + b_w{}^n\Delta_t\phi\right]$$

$$= V(\phi b_w)^{n+1}\Delta_t S_w + VS_w^n\left[\phi^{n+1}b_w'\Delta_t p_w + b_w{}^n\phi'\Delta_t p_o\right]$$

$$= V\left[(\phi b_w)^{n+1} - S_w^n\phi^{n+1}b_w'\, p_c'\right]\Delta_t S_w + VS_w^n\left[\phi^{n+1}b_w' + b_w{}^n\phi'\right]\Delta_t p_o \quad \text{..... (4.92)}$$

Consequently, Eqs. 4.91 and 4.92 could then be expressed as:

$$V\left[(\phi b_w)^{n+1} - \phi^n S_w^n b_w'\, p_c'\right]\Delta_t S_w + V\left[S_w^n b_w^{n+1}\phi' + S_w^n\phi^n b_w'\right]\Delta_t p_o$$

or,
$$V\left[(\phi b_w)^{n+1} - S_w^n\phi^{n+1}b_w'\, p_c'\right]\Delta_t S_w + VS_w^n\left[\phi^{n+1}b_w' + b_w{}^n\phi'\right]\Delta_t p_o$$

$$= (T_w)_{i+1/2,j,k}\left[(p_o)_{i+1,j,k} - (p_o)_{i,j,k}\right] + (T_w)_{i-1/2,j,k}\left[(p_o)_{i-1,j,k} - (p_o)_{i,j,k}\right]$$

$$+ (T_w)_{i,j+1/2,k}\left[(p_o)_{i,j+1,k} - (p_o)_{i,j,k}\right] + (T_w)_{i,j-1/2,k}\left[(p_o)_{i,j-1,k} - (p_o)_{i,j,k}\right]$$

$$+ (T_w)_{i,j,k+1/2}\left[(p_o)_{i,j,k+1} - (p_o)_{i,j,k}\right] + (T_w)_{i,j,k-1/2}\left[(p_o)_{i,j,k-1} - (p_o)_{i,j,k}\right]$$

$$-(T_w p_c')_{i+1/2,j,k}\left[(S_w)_{i+1,j,k} - (S_w)_{i,j,k}\right] - (T_w p_c')_{i-1/2,j,k}\left[(S_w)_{i-1,j,k} - (S_w)_{i,j,k}\right]$$

$$-(T_w p_c')_{i,j+1/2,k}\left[(S_w)_{i,j+1,k} - (S_w)_{i,j,k}\right] - (T_w p_c')_{i,j-1/2,k}\left[(S_w)_{i,j-1,k} - (S_w)_{i,j,k}\right]$$

$$-(T_w p_c')_{i,j,k+1/2}\left[(S_w)_{i,j,k+1} - (S_w)_{i,j,k}\right] - (T_w p_c')_{i,j,k-1/2}\left[(S_w)_{i,j,k-1} - (S_w)_{i,j,k}\right]$$

$$- \sum T_w\gamma_w\Delta z - Q_{wi,j,k} \quad \text{..... (4.93)}$$

4.2.4.3. Source/Sink Term

The source/sink term was defined as follows:

$$(q_l)_{i,j,k} = (WI)_{i,j,k}(\lambda_l)_{i,j,k}\left[(p_l)_{i,j,k} - (p_{wf})_{i,j,k}\right] \quad \text{..... (4.94)}$$

The well index was the same as the single-phase flow, and the mobility was expressed as:

$$(\lambda_l)_{i,j,k} = \left(\frac{K(k_r)_l}{B_l \mu_l} \right)_{i,j,k} \quad \text{..... (4.95)}$$

4.2.4.4. Set-up Matrix Equation

The matrix equation for the two-phase fluid flow was expressed as:

$$TX = D\frac{dX}{dt} + G + Q \quad \text{..... (4.96)}$$

X was a primary variable vector. In the single-phase fluid flow, I had one primary variable for pressure. In the two-phase flow, I had two primary variables: pressure and saturation. The finite difference equations for the oil and water flows were expressed as:

1) Oil equation:

$$\begin{aligned} &D_{21}\Delta_t p_o + D_{22}\Delta_t S_w \\ &\quad = (T_o)_{i+1/2,j,k}(p_o)_{i+1,j,k} + (T_o)_{i-1/2,j,k}(p_o)_{i-1,j,k} + (T_o)_{i,j+1/2,k}(p_o)_{i,j+1,k} \\ &+ (T_o)_{i,j-1/2,k}(p_o)_{i,j-1,k} + (T_o)_{i,j,k+1/2}(p_o)_{i,j,k+1} + (T_o)_{i,j,k-1/2}(p_o)_{i,j,k-1} \\ &- (p_o)_{i,j,k}\sum (T_o)_{i,j,k} - \sum T_o \gamma_o \Delta z + q_{oi,j,k} \end{aligned} \quad \text{..... (4.97)}$$

where

$$\begin{aligned} \sum (T_o)_{i,j,k} &= (T_o)_{i+1/2\,j,k} + (T_o)_{i-1/2\,j,k} + (T_o)_{i,j+1/2,k} \\ &\quad + (T_o)_{i,j-1/2,k} + (T_o)_{i,j,k+1/2} + (T_o)_{i,j,k-1/2} \end{aligned}$$

$$D_{21} = V_{i,j}(1 - S_w)^n \left[\phi_o^{n+1} b' + b_o{}^n \phi' \right], \quad D_{22} = -V_{i,j}(\phi b_o)^{n+1} \quad \text{..... (4.98)}$$

2) Water equation

$$
\begin{aligned}
&D_{11}\Delta_t p_o + D_{12}\Delta_t S_w \\
&\quad = (T_w)_{i+1/2,j,k}(p_o)_{i+1,j,k} + (T_w)_{i-1/2,j,k}(p_o)_{i-1,j,k} + (T_w)_{i,j+1/2,k}(p_o)_{i,j+1,k} \\
&\quad + (T_w)_{i,j-1/2,k}(p_o)_{i,j-1,k} + (T_w)_{i,j,k+1/2}(p_o)_{i,j,k+1} + (T_w)_{i,j,k-1/2}(p_o)_{i,j,k-1} \\
&- (p_o)_{i,j,k}\sum(T_w)_{i,j,k} - (T_w p_c')_{i+1/2,j,k}(S_w)_{i+1,j,k} \\
&- (T_w p_c')_{i-1/2,j,k}(S_w)_{i-1,j,k} - (T_w p_c')_{i,j+1/2,k}(S_w)_{i,j+1,k} \\
&- (T_w p_c')_{i,j-1/2,k}(S_w)_{i,j-1,k} - (T_w p_c')_{i,j,k+1/2}(S_w)_{i,j,k+1} \\
&- (T_w p_c')_{i,j,k-1/2}(S_w)_{i,j,k-1} + (S_w)_{i,j,k}\sum(T_w p_c')_{i,j,k} \\
&- \sum T_w \gamma_w \Delta z + q_{wi,j,k} \qquad \cdots\cdots (4.99)
\end{aligned}
$$

where

$$
\begin{aligned}
&\sum(T_w)_{i,j,k} = (T_w)_{i+1/2\,j,k} + (T_w)_{i-1/2\,j,k} + (T_w)_{i,j+1/2,k} \\
&\qquad + (T_w)_{i,j-1/2,k} + (T_w)_{i,j,k+1/2} + (T_w)_{i,j,k-1/2} \\
&D_{11} = V\left[S_w^n b_w^{n+1}\phi' + S_w^n \phi^n b_w'\right], \quad D_{22} = V\left[(\phi b_w)^{n+1} - \phi^n S_w^n b_w' p_c'\right] \\
&\sum(T_w p_c')_{i,j,k} = (T_w p_c')_{i+1/2\,j,k} + (T_w p_c')_{i-1/2\,j,k} + (T_w p_c')_{i,j+1/2,k} \\
&\quad + (T_w p_c')_{i,j-1/2,k} + (T_w p_c')_{i,j,k+1/2} + (T_w p_c')_{i,j,k-1/2} \qquad \cdots\cdots (4.100)
\end{aligned}
$$

The primary variable vector, X, had entries of $\left[(p_o)_{i,j,k}, (S_w)_{i,j,k}\right]^T$. The transmissibility matrix, T, accumulation matrix, D, gravity vector, G, and source/sink term, Q, were expressed as follows.

$$
TX = \begin{bmatrix}
[C] & [E] & & [S] & & & & & & [B] & & \\
[W] & [C] & [E] & & [S] & & & & & & [B] & \\
 & [W] & [C] & & & [S] & & & & & & [B] \\
[N] & & & [C] & [E] & & [S] & & & & & \\
 & [N] & & [W] & [C] & [E] & & [S] & & & & \\
 & & & & & \ddots & & & & & & \\
 & & & & & & \ddots & & & & & \\
 & & & [N] & & & [W] & [C] & [E] & & [S] & \\
 & & & & [N] & & & [W] & [C] & & & [S] \\
[T] & & & & & [N] & & & [W] & [C] & [E] & \\
 & [T] & & & & & [N] & & & [W] & [C] & [E] \\
 & & [T] & & & & & N & & & [W] & [C]
\end{bmatrix}
\begin{bmatrix} [X] \\ \\ \\ \\ \\ \\ \vdots \\ \\ \\ \\ \\ [X] \end{bmatrix} \cdots\cdots \qquad (4.101)
$$

$$[C]=\begin{bmatrix} -\sum(T_w)_{i,j,k} & \sum(T_w p_c')_{i,j,k} \\ -\sum(T_o)_{i,j,k} & 0 \end{bmatrix}, \quad [X]=\begin{bmatrix} p_o \\ S_w \end{bmatrix}$$

$$[E]=\begin{bmatrix} (T_w)_{i+1/2,j,k} & -(T_w p_c')_{i+1/2,j,k} \\ (T_o)_{i+1/2,j,k} & 0 \end{bmatrix} \quad \text{..... (4.102)}$$

$[W]$, $[N]$, $[S]$, $[T]$, and $[B]$ were computed in the same manner as the grid position.

$$D\frac{dX}{dt}=\begin{bmatrix} [D] & & & & & & & & \\ & [D] & & & & & & & \\ & & [D] & & & & & & \\ & & & [D] & & & & & \\ & & & & \ddots & & & & \\ & & & & & [D] & & & \\ & & & & & & [D] & & \\ & & & & & & & [D] & \\ & & & & & & & & [D] \end{bmatrix} \begin{bmatrix} \left[\frac{dX}{dt}\right] \\ \\ \\ \vdots \\ \\ \\ \left[\frac{dX}{dt}\right] \end{bmatrix}, \quad \text{..... (4.103)}$$

where

$$[D]=\begin{bmatrix} D_{11} & D_{12} \\ D_{21} & D_{22} \end{bmatrix}, \quad \left[\frac{dX}{dt}\right]=\begin{bmatrix} \frac{dp_o}{dt} \\ \frac{dS_w}{dt} \end{bmatrix} \quad \text{..... (4.104)}$$

$$G=\begin{bmatrix}\left[G_{i,j,k}\right]\\ \vdots \\ \left[G_{i,j,k}\right]\end{bmatrix},\quad Q=\begin{bmatrix}\left[Q_{i,j,k}\right]\\ \vdots \\ \left[Q_{i,j,k}\right]\end{bmatrix} \qquad \text{(4.105)}$$

where

$$\left[G_{i,j,k}\right]=\begin{bmatrix}\sum T_w\gamma_w\Delta z\\ \sum T_o\gamma_o\Delta z\end{bmatrix},\ \left[Q_{i,j,k}\right]=\begin{bmatrix}(q_w)_{i,j,k}\\ (q_o)_{i,j,k}\end{bmatrix} \qquad \text{(4.106)}$$

4.2.4.5. Computation of the Primary Variables

I wrote the residual $R\left[R_w, R_o\right]$ in the two-phase flow, as follows. Every coefficient term was the value at the $(n+1)$ time step.

$$\begin{aligned}
&R_w\left(X_{i,j,k}^{n+1}\right)=(T_w)_{i+1/2,j,k}(p_o)_{i+1,j,k}+(T_w)_{i-1/2,j,k}(p_o)_{i-1,j,k}\\
&+(T_w)_{i,j+1/2,k}(p_o)_{i,j+1,k}+(T_w)_{i,j-1/2,k}(p_o)_{i,j-1,k}+(T_w)_{i,j,k+1/2}(p_o)_{i,j,k+1}\\
&+(T_w)_{i,j,k-1/2}(p_o)_{i,j,k-1}-(p_o)_{i,j,k}\sum(T_w)_{i,j,k}-(T_w p_c')_{i+1/2,j,k}(S_w)_{i+1,j,k}\\
&-(T_w p_c')_{i-1/2,j,k}(S_w)_{i-1,j,k}-(T_w p_c')_{i,j+1/2,k}(S_w)_{i,j+1,k}\\
&-(T_w p_c')_{i,j-1/2,k}(S_w)_{i,j-1,k}-(T_w p_c')_{i,j,k+1/2}(S_w)_{i,j,k+1}\\
&-(T_w p_c')_{i,j,k-1/2}(S_w)_{i,j,k-1}+(S_w)_{i,j,k}\sum(T_w p_c')_{i,j,k}-\sum T_w\gamma_w\Delta z+q_{wi,j,k}\\
&-V\left[S_w^n b_w^{n+1}\phi'+S_w^n\phi^n b_w'\right]\Delta_t p_o-V\left[(\phi b_w)^{n+1}-\phi^n S_w^n b_w' p_c'\right]\Delta_t S_w
\end{aligned} \qquad \text{(4.107)}$$

$$\begin{aligned}
&R_o\left(X_{i,j,k}^{n+1}\right)=(T_o)_{i+1/2,j,k}(p_o)_{i+1,j,k}+(T_o)_{i-1/2,j,k}(p_o)_{i-1,j,k}\\
&+(T_o)_{i,j+1/2,k}(p_o)_{i,j+1,k}+(T_o)_{i,j-1/2,k}(p_o)_{i,j-1,k}+(T_o)_{i,j,k+1/2}(p_o)_{i,j,k+1}\\
&+(T_o)_{i,j,k-1/2}(p_o)_{i,j,k-1}-(p_o)_{i,j,k}\sum(T_o)_{i,j,k}-\sum T_o\gamma_o\Delta z+q_{oi,j,k}\\
&-V_{i,j}(1-S_w)^n\left[\phi_o^{n+1}b'+b_o{}^n\phi'\right]\Delta_t p_o+V_{i,j}(\phi b_o)^{n+1}\Delta_t S_w
\end{aligned} \qquad \text{(4.108)}$$

In the two-phase flow, the Jacobian matrix was written as follows.

$$J=\begin{bmatrix}
[C] & [E] & & [S] & & & & & & [B] & & \\
[W] & [C] & [E] & & [S] & & & & & & [B] & \\
 & [W] & [C] & & & [S] & & & & & & [B] \\
[N] & & & [C] & [E] & & [S] & & & & & \\
 & [N] & & [W] & [C] & [E] & & [S] & & & & \\
 & & & & & \ddots & & & & & & \\
 & & & & & & \ddots & & & & & \\
 & & & [N] & & & [W] & [C] & [E] & & [S] & \\
 & & & & [N] & & & [W] & [C] & & & [S] \\
[T] & & & & & [N] & & & [W] & [C] & [E] & \\
 & [T] & & & & & [N] & & & [W] & [C] & [E] \\
 & & [T] & & & & & N & & & [W] & [C]
\end{bmatrix} \quad \text{..... (4.109)}$$

The Jacobian matrix had the same block hepta-diagonal matrix format as the transmissibility matrix, T. In the same row of the Jacobian matrix, I wrote the entries as follows.

$$[C]=\begin{bmatrix}
\frac{\partial(R_w)_{i,j,k}}{\partial(p_o)_{i,j,k}} & \frac{\partial(R_w)_{i,j,k}}{\partial(S_w)_{i,j,k}} \\
\frac{\partial(R_o)_{i,j,k}}{\partial(p_o)_{i,j,k}} & \frac{\partial(R_o)_{i,j,k}}{\partial(S_w)_{i,j,k}}
\end{bmatrix}$$

$$[W]=\begin{bmatrix}
\frac{\partial(R_w)_{i,j,k}}{\partial(p_o)_{i-1,j,k}} & \frac{\partial(R_w)_{i,j,k}}{\partial(S_w)_{i-1,j,k}} \\
\frac{\partial(R_o)_{i,j,k}}{\partial(p_o)_{i-1,j,k}} & \frac{\partial(R_o)_{i,j,k}}{\partial(S_w)_{i-1,j,k}}
\end{bmatrix}, \quad [E]=\begin{bmatrix}
\frac{\partial(R_w)_{i,j,k}}{\partial(p_o)_{i+1,j,k}} & \frac{\partial(R_w)_{i,j,k}}{\partial(S_w)_{i+1,j,k}} \\
\frac{\partial(R_o)_{i,j,k}}{\partial(p_o)_{i+1,j,k}} & \frac{\partial(R_o)_{i,j,k}}{\partial(S_w)_{i+1,j,k}}
\end{bmatrix}$$

$$[N]=\begin{bmatrix}
\frac{\partial(R_w)_{i,j,k}}{\partial(p_o)_{i,j-1,k}} & \frac{\partial(R_w)_{i,j,k}}{\partial(S_w)_{i,j-1,k}} \\
\frac{\partial(R_o)_{i,j,k}}{\partial(p_o)_{i,j-1,k}} & \frac{\partial(R_o)_{i,j,k}}{\partial(S_w)_{i,j-1,k}}
\end{bmatrix}, \quad [S]=\begin{bmatrix}
\frac{\partial(R_w)_{i,j,k}}{\partial(p_o)_{i,j+1,k}} & \frac{\partial(R_w)_{i,j,k}}{\partial(S_w)_{i,j+1,k}} \\
\frac{\partial(R_o)_{i,j,k}}{\partial(p_o)_{i,j+1,k}} & \frac{\partial(R_o)_{i,j,k}}{\partial(S_w)_{i,j+1,k}}
\end{bmatrix}$$

$$[T]=\begin{bmatrix} \dfrac{\partial(R_w)_{i,j,k}}{\partial(p_o)_{i,j,k-1}} & \dfrac{\partial(R_w)_{i,j,k}}{\partial(S_w)_{i,j,k-1}} \\ \dfrac{\partial(R_o)_{i,j,k}}{\partial(p_o)_{i,j,k-1}} & \dfrac{\partial(R_o)_{i,j,k}}{\partial(S_w)_{i,j,k-1}} \end{bmatrix},\ [B]=\begin{bmatrix} \dfrac{\partial(R_w)_{i,j,k}}{\partial(p_o)_{i,j,k+1}} & \dfrac{\partial(R_w)_{i,j,k}}{\partial(S_w)_{i,j,k+1}} \\ \dfrac{\partial(R_o)_{i,j,k}}{\partial(p_o)_{i,j,k+1}} & \dfrac{\partial(R_o)_{i,j,k}}{\partial(S_w)_{i,j,k+1}} \end{bmatrix} \quad \text{..... (4.110)}$$

CHAPTER V

FINITE ELEMENT METHODS (FEM) FOR GEOMECHANICS SIMULATION

In the coupling simulation, the geomechanics was computed by finite element methods (FEMs). I modified the FEM algorithm used in the Sherif (2012) study to apply calculated pore pressure to geomechanics as an external load. The basic governing equations for geomechanics consist of equilibrium and constitutive equations, and a strain-displacement relationship (Lewis & Schrefler, 1998; Chin et al., 2002; Zheng et al., 2003; Sherif, 2012).

5.1 Discretization and Selection of Element Types

In this study, the basic four nodes rectangular element of Q4 (Figure 5.1) is used for displacement and pore pressure calculation. The same Cartesian grid is used for both the fluid flow FDM and the geomechanics FEM mode. The domain size is determined in the equivalent permeability simulation algorithm by REV calculation.

5.2 Shape Function

In the FEM, the unknown variables, displacement, and pore pressure were solved at selected finite points, and the variables inside the element were a function of the values at the nodal points of the element. To interpolate the solution at any point inside the element and at the nodal point, I needed a proper shape function.

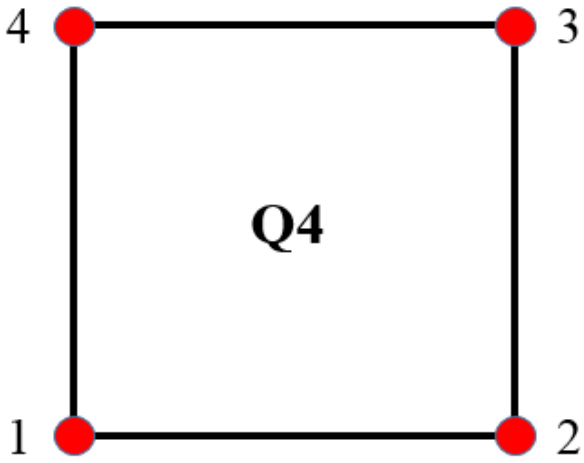

Figure 5.1 Four-node rectangular element (Q4).

Therefore, displacement and pore pressure (u, p) were expressed in vectors of nodal values and could be approximated by using a shape function. With displacement and pore pressure serving as the field variables, these relationships were expressed as:

$$u = N_u \bar{u}\,, \quad v = N_v \bar{v}$$
$$p = N_p \bar{p} \qquad (5.1)$$

where $\bar{u}$, $\bar{v}$, and $\bar{p}$ are the horizontal, vertical displacement, and pore pressure vectors at the element nodes, respectively; N_u, N_v, and N_p are the shape functions of the horizontal displacement, vertical displacement, and pore pressure, respectively. Pore pressure was treated as an external load in the FEM calculation. The shape functions were expressed with a natural coordinate system with a unity magnitude, as shown in Figure 5.2.

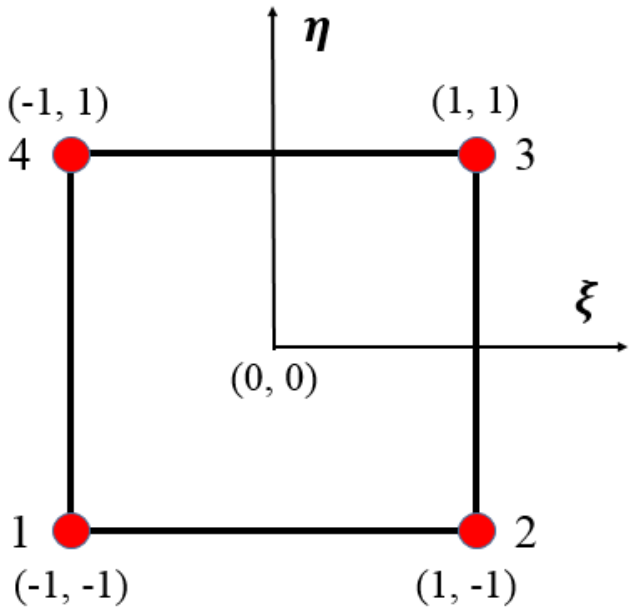

Figure 5.2 Reference coordinates in the four-node rectangular element.

The same shape of function was used for both the displacement and pore pressure vectors. For the Q4 rectangular element, the shape function was expressed as described below. In this equation, the shape function for the horizontal displacement, u, was explained; N_v and N_p were calculated in the same manner.

$$u = \sum_{i=1}^{n} N_i u_i = N_1 u_1 + N_2 u_2 + N_3 u_3 + N_4 u_4 \quad \text{..... (5.2)}$$

where

$$N_1 = \frac{(1-\xi)(1-\eta)}{4}, \quad N_2 = \frac{(1+\xi)(1-\eta)}{4}$$
$$N_3 = \frac{(1+\xi)(1+\eta)}{4}, \quad N_2 = \frac{(1-\xi)(1+\eta)}{4} \quad \text{..... (5.3)}$$

Then, the displacement and pore pressure at the nodal point was expressed using the shape function, as was the case in the relevant literature (Verruijt, 1995; Tran, 2002; Gai, 2004; Pan, 2009; Sherif, 2012):

$$\begin{Bmatrix} u \\ v \\ p \end{Bmatrix} = \begin{bmatrix} N_1 & 0 & 0 & N_2 & 0 & 0 & N_3 & 0 & 0 & N_4 & 0 & 0 \\ 0 & N_1 & 0 & 0 & N_2 & 0 & 0 & N_3 & 0 & 0 & N_4 & 0 \\ 0 & 0 & N_1 & 0 & 0 & N_2 & 0 & 0 & N_3 & 0 & 0 & N_4 \end{bmatrix} \begin{Bmatrix} u_1 \\ v_1 \\ p_1 \\ \vdots \\ \vdots \\ \vdots \\ u_4 \\ v_4 \\ p_4 \end{Bmatrix} \quad \text{..... (5.4)}$$

5.3 Strain/Displacement Relationships

The relationship between strain and displacement at any point in the element was expressed as:

$$\{\varepsilon\} = \begin{Bmatrix} \varepsilon_{xx} \\ \varepsilon_{yy} \\ \varepsilon_{xy} \\ \varepsilon_{zz} \end{Bmatrix} = [B]\{u\} \quad \text{..... (5.5)}$$

where $\{\varepsilon\}$ is the strain vector, $[B]$ is the strain-displacement matrix, and $\{u\}$ is the displacement vector. The strain-displacement matrix was a function of the partial derivatives of the shape function (with respect to the Cartesian coordinate system). Because shape functions are derived based on a reference coordinate system, the strain-

displacement matrix could not be used directly with a Cartesian coordinate system. The partial derivatives of the shape function were calculated using a chain rule. The strain-displacement matrix for a Q4 element was expressed as:

$$[B]=\begin{bmatrix} \frac{\partial N_1}{\partial x} & & \frac{\partial N_2}{\partial x} & & \frac{\partial N_3}{\partial x} & & \frac{\partial N_4}{\partial x} & \\ & \frac{\partial N_1}{\partial y} & & \frac{\partial N_2}{\partial y} & & \frac{\partial N_3}{\partial y} & & \frac{\partial N_4}{\partial y} \\ \frac{\partial N_1}{\partial y} & \frac{\partial N_1}{\partial x} & \frac{\partial N_2}{\partial y} & \frac{\partial N_2}{\partial x} & \frac{\partial N_3}{\partial y} & \frac{\partial N_3}{\partial x} & \frac{\partial N_4}{\partial y} & \frac{\partial N_4}{\partial x} \end{bmatrix} \quad \text{..... (5.6)}$$

where

$$\frac{\partial N}{\partial x}=\frac{\partial N}{\partial \xi}\frac{\partial \xi}{\partial x}+\frac{\partial N}{\partial \eta}\frac{\partial \eta}{\partial x}$$
$$\frac{\partial N}{\partial y}=\frac{\partial N}{\partial \xi}\frac{\partial \xi}{\partial y}+\frac{\partial N}{\partial \eta}\frac{\partial \eta}{\partial y} \quad \text{..... (5.7)}$$

Eq. 5.7 was rearranged using the inverse of a Jacobian matrix, which provided mapping between the derivatives of the real elements of the Cartesian coordinate system and the reference elements of the reference coordinate system. The Jacobian matrix was expressed as:

$$\begin{bmatrix} \frac{\partial N_i}{\partial x} \\ \frac{\partial N_i}{\partial y} \end{bmatrix}=[J]^{-1}\begin{bmatrix} \frac{\partial N_i}{\partial \xi} \\ \frac{\partial N_i}{\partial \eta} \end{bmatrix} \quad \text{..... (5.8)}$$

where

$$[J]=\begin{bmatrix}\frac{\partial x}{\partial \xi} & \frac{\partial y}{\partial \xi}\\ \frac{\partial x}{\partial \eta} & \frac{\partial y}{\partial \eta}\end{bmatrix}=\begin{bmatrix}\frac{\partial N_1}{\partial \xi} & \frac{\partial N_2}{\partial \xi} & \frac{\partial N_3}{\partial \xi} & \frac{\partial N_4}{\partial \xi}\\ \frac{\partial N_1}{\partial \eta} & \frac{\partial N_2}{\partial \eta} & \frac{\partial N_3}{\partial \eta} & \frac{\partial N_4}{\partial \eta}\end{bmatrix}\begin{bmatrix}x_1 & y_1\\ x_2 & y_2\\ x_3 & y_3\\ x_4 & y_4\end{bmatrix} \quad \text{..... (5.9)}$$

5.4 Stress/Strain Relationships

In this study, a plane strain condition was used for the geomechanics simulation. In a plane strain condition, displacement of the long-direction is equal to zero. Usually, a plane strain condition is assumed when the front and rear faces of an element are considered to be restrained against the displacement, as shown in Figure 5.3.

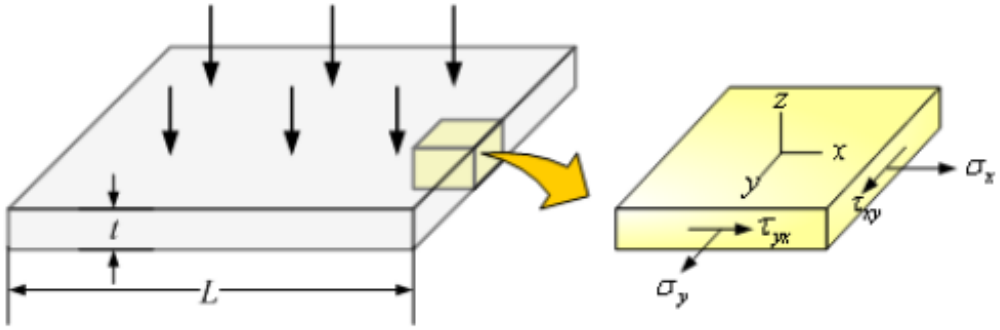

Figure 5.3 Plane strain condition.

In this research, the relationship between stresses and strains in a plane strain condition was expressed as:

$$\{\sigma\}=\begin{Bmatrix}\sigma_{xx}\\ \sigma_{yy}\\ \tau_{xy}\\ \sigma_{zz}\end{Bmatrix}=[C]\{\varepsilon\} \quad \text{..... (5.10)}$$

where

$$\sigma_{zz} = \nu\left(\sigma_{xx} + \sigma_{yy}\right) \quad (5.11)$$

$$[C] = \frac{E}{(1+\nu)(1-2\nu)}\begin{bmatrix} 1-\nu & \nu & 0 & \nu \\ \nu & 1-\nu & 0 & \nu \\ 0 & 0 & \frac{1-2\nu}{2} & 0 \\ \nu & \nu & 0 & 1-\nu \end{bmatrix} \quad (5.12)$$

where $\{\sigma\}$ is the stress vector, τ is the shear stress, $\{\varepsilon\}$ is the strain vector, $[C]$ is the linear elastic constitutive matrix or stress strain matrix, E is the Young's modulus, and ν is the Poisson's ratio.

In Eq. 5.10, σ represents the total stress. If there was fluid in the geomechanics model, the effective stress, σ', was considered instead of σ, because only a change in the effective stress would affect solid matrix deformation.

$$\{\sigma'\} = [C]\{\varepsilon\} \quad (5.13)$$

Effective stress is a function of pore pressure; it was expressed using Biot's theory (Gai, 2004; Aghighi, 2007; Lee, 2008; Yang, 2013), as follows:

$$\sigma'_{ij} = \sigma_{ij} + \alpha\delta_{ij}\, p \quad (5.14)$$

Here, α is a Biot's coefficient and δ_{ij} is a Kronecker delta. They were expressed as:

$$a = 1 - \frac{K_b}{K_s}$$

$$\delta_{ij} = \begin{cases} 0 \ \ if \ \ i \neq j \\ 1 \ \ if \ \ i = j \end{cases} \quad \text{..... (5.15)}$$

where K_b is the bulk stiffness and K_s is the solid matrix stiffness.

5.5 Stiffness Matrix

The stiffness matrix relating nodal forces to displacements was obtained using force equilibrium conditions or the principle of minimum potential energy. The principle of minimum potential energy states that work done by externally applied loads is equal to internal strain energy (Sherif, 2012).

The external work, W_e, relating externally applied loads to displacements was expressed as:

$$W_e = \frac{1}{2} dudF \quad \text{or} \quad W_e = \frac{1}{2} \{du\}^T \{dF\} \quad \text{..... (5.16)}$$

where u is the displacement and, F is the applied force.

The internal work, W_i, was expressed as:

$$W_i = \frac{1}{2} \int_{vol} d\varepsilon d\sigma dV \quad \text{or} \quad W_i = \frac{1}{2} \int_{vol} \{d\varepsilon\}^T \{d\sigma\} dV \quad \text{..... (5.17)}$$

where ε is volumetric strain, σ is the stress, and V is the element volume.

Substituting Eqs. 5.5 and 5.10 for Eq. 5.17 allowed it to be rearranged as:

$$W_i = \frac{1}{2}\int_{vol} \{du\}^T [B]^T [C][B]\{du\} dV \quad \text{..... (5.18)}$$

where $[B]$ is the strain-displacement matrix.

Based on the principle of minimum potential energy, I defined the relationship between force and displacement obtained from Eqs. 5.16 and 5.18.

$$\frac{1}{2}\{du\}^T \{dF\} = \frac{1}{2}\int_{vol} \{du\}^T [B]^T [C][B]\{du\} dV$$
$$\Rightarrow \{dF\} = \int_{vol} [B]^T [C][B] dV \{du\} \quad \text{..... (5.19)}$$

Eq. 5.19 was simplified using the stiffness matrix of element $[K^e]$ (Gai, 2004; Aghighi, 2007; Lee, 2008; Sherif, 2012; Yang, 2013), as follows:

$$\{F\} = [K^e]\{u\} \quad \text{..... (5.20)}$$

where

$$[K^e] = \int_{vol} [B]^T [C][B] dV \quad \text{..... (5.21)}$$

From Eq. 5.21, the nodal displacement was calculated from the force vector as:

$$\{u\} = [K^e]^{-1}\{F\} \quad \text{..... (5.22)}$$

5.6 Element Force Matrix

The force acting on the element consisted of external and internal forces, due to self-weight. The confining and pore pressures were treated as external forces in the FEM

geomechanics simulation; they were converted from the distributed load to the corresponding nodal forces using the shape functions, as follows:

$$\{F^e\} = \int_{vol} [N]^T \{f^d\} dV + \int_{\Gamma_F} [N]^T \{F^d\} d\Gamma \quad \text{..... (5.23)}$$

where $\{F^e\}$ is the force vector of the element, $\{f^d\}$ is the applied internal force vector, Γ_F is the surface where external forces are applied, and $\{F^d\}$ is the applied surface force vector.

5.7 Assembly of the Element Equations to Obtain the Global Equations

The global stiffness matrix that had the same matrix size of total unknown $\times$ total unknown was assembled by placing the local stiffness matrix such that it corresponded to the degree of freedom at each point.

$$[K] = \sum_{e=1}^{N} [K^e] \quad \text{..... (5.24)}$$

where $[K]$ is the global stiffness matrix, and N is the element number.

The global force matrix was calculated in the same manner.

$$[F] = \sum_{e=1}^{N} [F^e] \quad \text{..... (5.25)}$$

Figure 5.4 shows a summary of the equations used in the FEM.

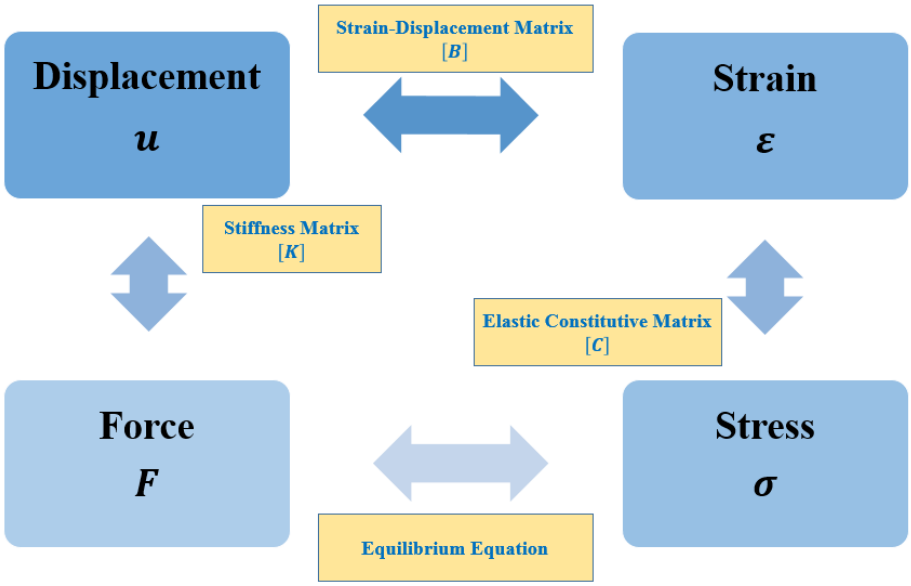

Figure 5.4 A summary of the equations used in the FEM.

The basic governing equations for the 2D solid FEM are given in Table 5.1.

Table 5.1 The basic governing equations for the 2D solid FEM

Equations	Matrix Form	Short Form
Stain-displacement relationship		
$\varepsilon_{xx} = \frac{\partial u_x}{\partial x}$ $\varepsilon_{yy} = \frac{\partial u_y}{\partial y}$ $\gamma_{xy} = \frac{\partial u_x}{\partial y} + \frac{\partial u_y}{\partial x}$	$\begin{Bmatrix}\varepsilon_{xx}\\ \varepsilon_{yy}\\ \gamma_{xy}\end{Bmatrix} = \begin{bmatrix}\frac{\partial}{\partial x} & 0\\ 0 & \frac{\partial}{\partial y}\\ \frac{\partial}{\partial y} & \frac{\partial}{\partial x}\end{bmatrix}\begin{Bmatrix}u_x\\ u_y\end{Bmatrix}$	$\boldsymbol{\varepsilon = Bu}$
Constitutive equation		
$\sigma_{xx} = \left(K + \frac{4}{3}G\right)\varepsilon_{xx} + \left(K - \frac{2}{3}G\right)\varepsilon_{yy}$ $\sigma_{yy} = \left(K - \frac{2}{3}G\right)\varepsilon_{xx} + \left(K + \frac{4}{3}G\right)\varepsilon_{yy}$ $\tau_{xy} = G\gamma_{xy}$	$\begin{Bmatrix}\sigma_{xx}\\ \sigma_{yy}\\ \tau_{xy}\end{Bmatrix} = \begin{bmatrix}\left(K + \frac{4}{3}G\right) & \left(K - \frac{2}{3}G\right) & 0\\ \left(K - \frac{2}{3}G\right) & \left(K + \frac{4}{3}G\right) & 0\\ 0 & 0 & G\end{bmatrix}\begin{Bmatrix}\varepsilon_{xx}\\ \varepsilon_{yy}\\ \gamma_{xy}\end{Bmatrix}$	$\boldsymbol{\sigma = D\varepsilon}$
Equilibrium equations		
$\frac{\partial \sigma_{xx}}{\partial x} + \frac{\partial \tau_{xy}}{\partial y} = 0$ $\frac{\partial \tau_{xy}}{\partial x} + \frac{\partial \sigma_{yy}}{\partial y} = \rho g$	$\begin{bmatrix}\frac{\partial}{\partial x} & 0 & \frac{\partial}{\partial y}\\ 0 & \frac{\partial}{\partial y} & \frac{\partial}{\partial x}\end{bmatrix}\begin{Bmatrix}\sigma_{xx}\\ \sigma_{yy}\\ \tau_{xy}\end{Bmatrix} = \begin{Bmatrix}0\\ \rho g\end{Bmatrix}$	$\boldsymbol{B^T\sigma = F}$

5.8 Gauss Integration

To calculate the stiffness and force matrices, I needed to integrate the equations over either the volume or area. The Gauss integration method, widely used as an approximation method for numerical integration, evaluates an integral as the weighted sum of function values at specified points. The accuracy of the approximation is a function of the integration order. If I chose larger numbers of integration points for the Gauss integration, I obtained more accurate results. However, this process could lead to a waste of computing cost. To address this issue, the integration point was selected after considering the desired accuracy and element type together. In this study, a 2×2 Gauss integration for the Q4 element was used in the FEM simulation (Smith & Griffiths, 1998; White, 2009; Sherif, 2012).

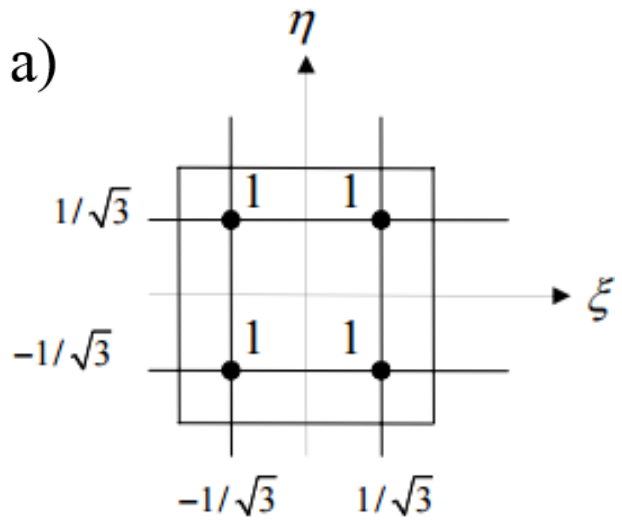

Figure 5.5 The 2×2 and 3×3 Gauss integrations in the Q4 rectangular element: a) 2×2 Gauss integration. b) 3×3 Gauss integration.

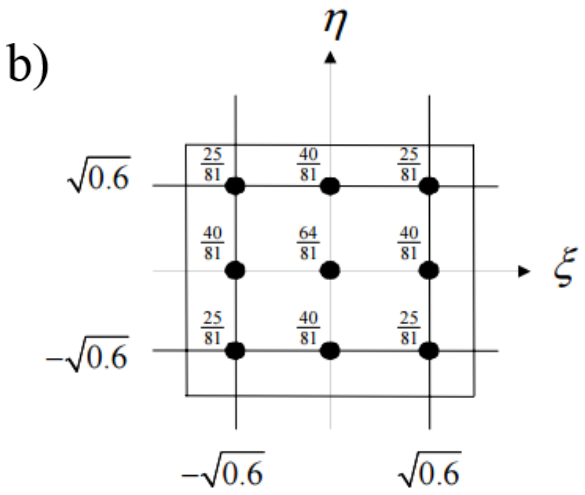

Figure 5.5 Continued.

Table 5.2 The Gauss integration point coordinates and weights for the rectangular element

Number of points, n	Points, $\varepsilon_i = \eta_i$	Weights, w_i
1	0	2
2	$\pm\sqrt{\frac{1}{3}}$	1
3	0	$\frac{8}{9}$
	$\pm\sqrt{\frac{3}{5}}$	$\frac{5}{9}$
4	$\pm\sqrt{\frac{3}{7}-\frac{2}{7}\sqrt{\frac{6}{5}}}$	$\frac{18+\sqrt{30}}{36}$
	$\pm\sqrt{\frac{3}{7}+\frac{2}{7}\sqrt{\frac{6}{5}}}$	$\frac{18-\sqrt{30}}{36}$

Figure 5.5 shows the 2×2 and 3×3 Gauss integrations in the Q4 rectangular element, and Table 5.2 shows the Gauss integration point coordinates and weights for the rectangular element. The Gauss integration of the selected function was calculated by:

$$\int_{-1}^{1}\int_{-1}^{1} f(\xi,\eta)d\xi d\eta = \sum_{j=1}^{n}\sum_{i=1}^{n} W_j W_i f(\xi,\eta) \quad \text{..... (5.26)}$$

where (ξ,η) are the reference coordinates of the Gauss sample point, $f(\xi,\eta)$ is the function value at the Gauss sample point in the reference coordinate system, n is the integration point number (integration order), and W is the weight of the Gauss sample point.

5.9 Finite Element Implementation of Biot's Theory

The equilibrium equation states that the external work accomplished by body and surface forces is equal to the internal work done by the stresses. This relationship is expressed as:

$$\int_{\Omega} \{\delta\varepsilon\}^T \Delta\sigma d\Omega = \int_{\Omega} \{\delta u\}^T \Delta b\, d\Omega + \int_{\Gamma_F} \{\delta u\}^T \Delta t\, d\Gamma \quad \text{..... (5.27)}$$

$$\delta\varepsilon = [B]\delta u \quad \text{..... (5.28)}$$

where $\delta\varepsilon$ is the strain change, δu is the displacement change, $\Delta\sigma$ is the stress increment induced by the external load increment, Δb is the applied internal force or self-weight force increment, Δt is the applied surface force increment, Ω is the volume,

Γ_F is the surface where external forces are applied, and $\left\{F^d\right\}$ is the applied external forces. Eq. 5.27 was rearranged as:

$$\int_{\Omega}\{\delta\varepsilon\}^T\Delta\sigma d\Omega-\int_{\Omega}\{\delta u\}^T\Delta b\,d\Omega-\int_{\Gamma_F}\{\delta u\}^T\Delta t\,d\Gamma=0 \quad \text{(5.29)}$$

Substituting Eq. 5.14 into Eq. 5.29 led to:

$$\int_{\Omega}\{\delta\varepsilon\}^T\Delta\sigma' d\Omega-\alpha\int_{\Omega}\{\delta\varepsilon\}^T\delta_{ij}\Delta p\,d\Omega-\int_{\Omega}\{\delta u\}^T\Delta b\,d\Omega-\int_{\Gamma_F}\{\delta u\}^T\Delta t\,d\Gamma=0 \quad \text{(5.30)}$$

Eq. 5.30 was rewritten in matrix form, as:

$$\int_{\Omega}([B]\{\delta u\})^T\Delta\sigma' d\Omega-\alpha\int_{\Omega}([B]\{\delta u\})^T\delta_{ij}\Delta p\,d\Omega-\int_{\Omega}\{\delta u\}^T\Delta b\,d\Omega-\int_{\Gamma_F}\{\delta u\}^T\Delta t\,d\Gamma=0$$

..... (5.31)

where

$$\int_{\Gamma_F}\{\delta u\}^T\Delta t\,d\Gamma\approx\int_{\Gamma_F}([N]\{\delta u\})^T\Delta t\,d\Gamma=\int_{\Gamma_F}\{\delta u\}^T[N]^T\Delta t\,d\Gamma \quad \text{(5.32)}$$

A Kronecker delta, δ_{ij}, can be expressed as an identity vector, m, in the matrix notation. The identity vector, m, was expressed in the 2D problem (Ing & Xiaoyan, 2002), as follows:

$$\{m\}=\{1\quad 1\quad 1\quad 0\}^T \quad \text{(5.33)}$$

Using the relationships from Eqs. 5.32 and 5.33, Eq. 5.31 was rearranged as:

$$\{\delta u\}\left(\int_{\Omega}[B]^T\Delta\sigma' d\Omega-\alpha\int_{\Omega}[B]^T\{m\}[N]\Delta p\,d\Omega-\int_{\Omega}[N]^T\Delta b\,d\Omega-\int_{\Gamma_F}[N]^T\Delta t\,d\Gamma\right)=0$$

..... (5.34)

Substituting Eq. 5.13 into Eq. 5.34 resulted in the following:

$$\{\delta u\}\left(\int_{\Omega}[B]^T[C]\Delta\varepsilon\, d\Omega-\alpha\int_{\Omega}[B]^T\{m\}[N]\Delta p\, d\Omega-\int_{\Omega}[N]^T\Delta b\, d\Omega-\int_{\Gamma_F}[N]^T\Delta t\, d\Gamma\right)=0$$

$$\{\delta u\}\left(\int_{\Omega}[B]^T[C][B]\Delta u\, d\Omega-\alpha\int_{\Omega}[B]^T\{m\}[N]\Delta p\, d\Omega-\int_{\Omega}[N]^T\Delta b\, d\Omega-\int_{\Gamma_F}[N]^T\Delta t\, d\Gamma\right)=0$$

$$\{\delta u\}\left(\int_{\Omega}[B]^T[C][B]d\Omega\,\Delta u-\alpha\int_{\Omega}[B]^T\{m\}[N]d\Omega\,\Delta p-\int_{\Omega}[N]^T\Delta b\, d\Omega-\int_{\Gamma_F}[N]^T\Delta t\, d\Gamma\right)=0$$

..... (5.35)

From Eq. 5.35, the pore pressure increment, Δp, was considered to be a body force applied to the porous media (Ing & Xiaoyan, 2002; Tran, 2002; Pan, 2009). The variable $\{\delta u\}$ was eliminated from Eq. 5.35 so that it could be further simplified as:

$$[K]\Delta u+[L]\Delta p=dF \quad \text{..... (5.36)}$$

In the equation,

$$[K]=\int_{\Omega}[B]^T[C][B]d\Omega \quad \text{..... (5.37)}$$

$$[L]=\alpha\int_{\Omega}[B]^T\{m\}[N]d\Omega \quad \text{..... (5.38)}$$

$$dF=\int_{\Omega}[N]^T\Delta b\, d\Omega+\int_{\Gamma_F}[N]^T\Delta t\, d\Gamma \quad \text{..... (5.39)}$$

where $[K]$ is the stiffness matrix, $[L]$ is the coupling matrix related to pore pressure, and dF is the incremental load. In Eq. 5.36, $-(\Delta p)$ was used for the pore pressure increment because pore pressure was considered to be an external body force, and the compressible force had a negative sign in the FEM. Using Eq. 5.36, the calculated pore pressure by the fluid flow FDM was passed to the geomechanics FEM simulator as external load data.

CHAPTER VI

ITERATIVE COUPLING SIMULATION AND STRESS-INDUCED PERMEABILITY CHANGING COUPLING SIMULATION

6.1 Coupling Approaches

There are two main kinds of coupling approaches used in coupling simulations: the volume coupling method using porosity as a coupling parameter, and coupling through a flow property such as permeability (Antonin Settari & Mourits, 1998; A. Settari & Walters, 2001; Thomas et al., 2003; Ta, 2007; Pan, 2009).

6.1.1 Volume Coupling

In iterative coupling, fluid flow and geomechanics simulators consider changes in pore volume to be a primary variable. Porosity is typically used for the volume coupling parameter. Calculated porosity is coupled using an external coupling module.

6.1.2 Coupling through Flow Property

Permeability is usually the coupling parameter when coupling through a flow property. Even though permeability is considered to be a constant variable in a traditional reservoir simulator, when coupling through a flow property, permeability is a function of several variables such as pressure, stress, strain, and porosity (Chin et al., 1998; Ta, 2007; Pan, 2009).

6.1.3 Porosity - Permeability Relationships

It is widely held that permeability depends upon porosity. However, because of the complicated and heterogeneous characteristics of a pore system, no fundamental relationship has yet been proposed. Many studies have discussed empirical porosity - permeability relationships (Nelson, 1994; Costa, 2006; Du & Wong, 2007b; Torskaya et al., 2007), and some researchers have tried to describe permeability using porosity and water saturation,

Some researchers have tried to describe permeability using porosity and water saturation, including:

Tixier (1949):

$$k = 62.5\frac{\phi^6}{S_{wi}^2} \quad \text{..... (6.1)}$$

Wyllie and Rose (1950):

$$k = \left(\frac{100\phi^{2.25}}{S_{wi}}\right)^2 \quad \text{..... (6.2)}$$

or,

$$k = \left(\frac{100\phi^2\left[1 - S_{wi}\right]}{S_{wi}}\right)^2 \quad \text{..... (6.3)}$$

Timur (1968):

$$k = 8.58\frac{\phi^{4.4}}{S_{wi}^2} \quad \text{..... (6.4)}$$

Coates and Dumanoir (1973):

$$k = 4.90 \frac{\phi^4 (1 - S_{wi})^2}{S_{wi}^4} \quad \text{..... (6.5)}$$

and, Samuel (2014):

$$k = a\phi^b S_{wi}^c \quad \text{..... (6.6)}$$

where ϕ is the porosity, and S_{wi} is the irreducible water saturation. In Eq. 6.6, the values of a, b, and c are determined from nonlinear iterations during the process of regression (Samuel, 2014).

Berg (1970) used porosity and grain size to suggest the permeability relationship below:

$$k = 8.4 \times 10^{-2} \times d^2 \phi^{5.1} \quad \text{..... (6.7)}$$

where d is the grain size of the porous media.

Costa (2006) used fractal pore-space geometry to describe the permeability relationship, as follows:

$$k = C_c \frac{\phi^m}{(1 - \phi)} \quad \text{..... (6.8)}$$

where C_c is the parameter, and m has the range of $1 < m < 4$.

One of the most widely used porosity – permeability relationships is the Kozeny-Carman (1956) empirical model (Nelson, 1994; Costa, 2006; Ta, 2007; Torskaya et al., 2007). This model assumes that permeability changes attributable to porosity variations are equal in all directions:

$$\frac{k}{k_0} = \left(\frac{\phi}{\phi_0}\right)^3 \frac{(1-\phi_0)^2}{(1-\phi)^2} \quad \text{..... (6.10)}$$

where k is the permeability of the current time step, k_0 is the initial permeability, ϕ is the porosity of the current time step, and ϕ_0 is the initial porosity.

Tortike and Ali (1993) used porosity and volumetric strain to express the permeability relationship as:

$$\frac{k}{k_0} = \frac{\left(1+\frac{\varepsilon_v}{\phi_0}\right)^3}{1+\varepsilon_v} \quad \text{..... (6.11)}$$

where ε_v is the volumetric strain.

Eq. 6.11 was used in the iterative coupling simulation to calculate the equivalent permeability. However, most empirical equations estimate permeability changes using porosity, water saturation, and/or volumetric strain changes; they have certain limitations that reflect the heterogeneous characteristics of permeability distributions. It was also difficult to directly apply these equations to different reservoir conditions.

To overcome this shortcoming, I developed stress-induced aperture-changing coupling simulation algorithms. Stress-induced aperture deformation was calculated using the normal stiffness of fractures. For that, effective normal stress changes of fractures were interpolated by ordinary kriging. Then, the equivalent permeability was estimated using updated aperture and fracture geometry information for every time step.

The stress-induced aperture-changing calculation algorithm will be explained in the following Chapter.

6.2 Reservoir Porosity and True Porosity

For the FDM fluid flow analysis, the bulk volume of the reservoir domain was regarded as a constant during the simulation. Conversely, the bulk and pore volumes in the geomechanics FEM model changed during the simulation. Therefore, the true porosity calculated from the geomechanics model could not directly be used in the fluid flow model. It had to be converted to reservoir porosity, based on the constant bulk volume of the corresponding grid (Aziz & Settari, 1979; Antonin Settari & Mourits, 1998; Chin et al., 2000; Chin et al., 2002; Thomas et al., 2003; Tran et al., 2004; Pan et al., 2009).

The fluid compressibility was expressed as:

$$c_f = \frac{1}{\rho}\left(\frac{\partial \rho}{\partial p}\right)_T \quad \text{..... (6.12)}$$

The pore volume compressibility was defined as:

$$c_p = \frac{1}{\phi}\left(\frac{\partial \phi}{\partial p}\right)_T \quad \text{..... (6.13)}$$

where c_f is the fluid compressibility, and c_p is the pore compressibility at pore pressure, p, and constant reservoir temperature, T. Eq. 6.13 could then be rearranged as:

$$c_p = \frac{1}{\phi}\left(\frac{\partial \phi}{\partial p}\right)_T \Rightarrow \int_{p_0}^{p} c_p dp = \int_{\phi_0}^{\phi} \frac{1}{\phi} d\phi$$

$$c_p\left(p - p_0\right) = \ln \frac{\phi}{\phi_0}$$

$$e^{c_p(p-p_0)} = \frac{\phi}{\phi_0}$$

$$\phi = \phi^0 e^{c_p(p-p_0)} \approx \phi^0\left[1 + c_p\left(p - p_0\right)\right] \quad (6.14)$$

Namely,

$$\phi = \phi^0\left[1 + c_p\left(p - p_0\right)\right] \quad (6.15)$$

where ϕ^0 is the initial porosity at p^0, c_p is the pore volume compressibility, and p^0 is the initial pressure.

In a traditional reservoir simulator, it is assumed that the bulk volume is fixed and the reservoir rock is non-deformable. In such cases, pore volume compressibility can be approximated as:

$$c_f = c_p \approx \frac{1}{V_p}\left(\frac{\partial V_p}{\partial p}\right)_T \quad (6.16)$$

where V_p is the pore volume.

Therefore, Eq. 6.15 was rewritten using Eq. 6.16:

$$\phi = \phi^0\left[1 + c_f\left(p - p^0\right)\right] \quad (6.17)$$

where c_f is fluid compressibility.

Also, Eq. 6.15 was expressed by the following linear expression of rock compressibility, c_R, and pore pressure (Aziz & Settari, 1979; Pan, 2009):

$$\phi = \phi^0 \left[1 + c_R \left(p - p^0\right)\right] \quad \text{(6.18)}$$

where c_R is the rock compressibility.

Eqs. 6.17 and 6.18 represent the porosity relationship most widely used in traditional reservoir simulators (Tran, 2002; Minkoff et al., 2003; Ta, 2007; Pan, 2009).

However, because the mathematical equations in the geomechanics FEM were based on a deformable mesh with time, the porosity calculated by the geomechanics FEM could not be directly coupled with the fluid flow FDM. The porosity calculated by the geomechanics FEM was called "true porosity," and the porosity calculated by the fluid flow FDM was called "reservoir porosity." True porosity had to be converted into the reservoir porosity defined by the fixed bulk volume in the reservoir simulation in order to maintain numerical consistency.

Chin et al. (2002) proposed the following relationships between reservoir porosity and true porosity:

$$\begin{cases} \phi^* = 1 - \left(1 - \phi_0\right) e^{-\varepsilon_v} \\ \phi = \left(\dfrac{1 - \phi_0}{1 - \phi^*}\right) \phi^* \end{cases} \quad \text{(6.19)}$$

or

$$\begin{cases} \phi^* = 1 - \left(1 - \phi_0\right) e^{-\varepsilon_v} \\ \phi = \left(\dfrac{1 - \phi_0}{1 - \phi^*}\right) \phi^* = \left(\dfrac{1 - \phi_0}{\left(1 - \phi_0\right) e^{-\varepsilon_v}}\right) \left[1 - \left(1 - \phi_0\right) e^{-\varepsilon_v}\right] = e^{-\varepsilon_v} - \left(1 - \phi_0\right) \end{cases} \quad \text{(6.20)}$$

where ϕ denotes the reservoir porosity from the fluid flow FDM, and ϕ^* denotes the true porosity from the geomechanics FEM (Chin et al., 2002; Tran, 2002; Thomas et al., 2003; Pan, 2009).

The true porosity obtained from Eqs. 6.19 and 6.20 was determined from the volumetric strain calculated by the geomechanics FEM.

The equation for true porosity was derived from the mass balance equation (Verruijt, 1995; Lewis & Schrefler, 1998; Chin et al., 2002; Pan, 2009):

$$\frac{\partial}{\partial t}(1-\phi)\rho_s + \nabla \cdot (1-\phi)\rho_s v_s = 0 \quad \text{..... (6.21)}$$

where ρ_s is the solid density, and v_s is the solid velocity. Based on the basic theory, the solid particle was assumed to be incompressible and rearrangement of the solid particle resulted in deformation. Therefore, the solid density could be eliminated from Eq. 6.21, because it remained constant during the simulation. Then, Eq. 6.21 was rearranged as:

$$\frac{\partial}{\partial t}(1-\phi) + \nabla \cdot (1-\phi)v_s = 0 \quad \text{..... (6.22)}$$

$$\frac{\partial}{\partial t}(1-\phi) + v_s \cdot \nabla(1-\phi) + (1-\phi)\nabla \cdot v_s = 0 \quad \text{..... (6.23)}$$

Solid velocity could then be expressed as:

$$v_s = \frac{du_s}{dt} \quad \text{..... (6.24)}$$

where u_s is the solid displacement. Volumetric strain was expressed using the solid displacement, as follows:

$$\varepsilon_v = \nabla \cdot u_s \quad \text{..... (6.25)}$$

Using Eq. 6.25, the formulation of $\nabla \cdot v_s$ was rewritten as:

$$\nabla \cdot v_s = \nabla \cdot \frac{du_s}{dt} = \frac{d\varepsilon_v}{dt} \quad \text{..... (6.26)}$$

The definition of material derivatives was:

$$\frac{df}{dt} = \frac{\partial f}{\partial t} + v_s \cdot \nabla f \quad \text{..... (6.27)}$$

Using Eqs. 6.25 and 6.27, Eq. 6.23 was rewritten as:

$$\frac{\partial}{\partial t}(1-\phi) + v_s \cdot \nabla(1-\phi) + (1-\phi)\frac{d\varepsilon_v}{dt} = 0$$

$$\Rightarrow \frac{d}{dt}(1-\phi) + (1-\phi)\frac{d\varepsilon_v}{dt} = 0 \quad \text{..... (6.28)}$$

or

$$-\frac{1}{(1-\phi)}\frac{d(1-\phi)}{dt} = \frac{d\varepsilon_v}{dt} \quad \text{..... (6.29)}$$

This allowed both sides to be integrated as:

$$-\left[\ln\left(1-\phi^*\right)\right] + \left[\ln\left(1-\phi_0\right)\right] = \varepsilon_v - 0$$

$$\ln\left(\frac{1-\phi_0}{1-\phi^*}\right) = \varepsilon_v$$

$$1-\phi_0 = \left(1-\phi^*\right)e^{\varepsilon_v}$$

$$\phi^* = 1-(1-\phi_0)e^{-\varepsilon_v} \quad \text{(6.30)}$$

where ϕ^* is the porosity at time step t. Eq. 6.30 was the derivation of the true porosity formulation of Eqs. 6.19 and 6.20. The porosity of the coupling was calculated by Eq. 6.19. However, these equations had some limitations when applied in the low matrix permeability and fracture flow dominant reservoir simulations. In fracture flow dominant reservoir conditions, stress changes due to pore pressure changes mainly happen along the fractures. Therefore, in this study, fracture porosity changes were directly estimated from stress-induced aperture changing calculations at every time step.

6.3 Iterative Coupling Simulation

This study developed codes for a 2D iteratively-coupled fluid flow and geomechanics simulation using a Cartesian grid. As shown in Figure 1.1 (b), the estimated equivalent permeability data were passed to the FDM fluid flow simulator. The fluid flow in porous media was first solved by the FDM using the Newton-Raphson iteration algorithm. The advantages and disadvantages to using iterative coupling methods are outlined below.

Advantages:

1) **Independent simulation**. Because fluid and geomechanics properties are independently calculated in each simulator, there is no need to build a full matrix to simultaneously simulate both fluid and geomechanics.

2) **Flexibility and modularity**. In iterative coupling methods, the fluid and geomechanics simulators are coupled through the coupling module using coupling parameters. A geomechanics simulator can easily be coupled with a commercial flow simulator, and vice versa, with certain modifications.
3) **Coupling with different simulation methods**. Different simulation methods can easily be coupled through iterative coupling methods. For example, finite difference methods and finite volume methods for fluid flow simulation can be simply coupled with finite element methods for geomechanics.
4) **Easy convergence control**. Fluid flow and geomechanics are sequentially simulated, and the convergence of each simulation is independently reviewed. Therefore, the convergence problem can be more easily verified and controlled than with fully coupling methods.
5) **Accuracy** Iterative coupling methods can compute the same results as fully coupling methods if sufficient nonlinear convergence criteria for both coupled simulators are satisfied.

However, iterative coupling methods may require more computational time than fully coupling methods if one component of the coupling module is not properly converged. Because the iteration of each simulator is repeated until the convergence level is below the given tolerance level, proper convergence significantly affects the computational time.

In this study, the MATLAB Reservoir Simulation Toolbox (MRST) framework was used for the fluid flow simulator (Lie et al., 2011). Porosity was a convergence-checking parameter for the coupling simulation.

6.4 Kriging – Geostatistical Analysis

Geostatistics is a statistical method used to characterize and predict spatial variables. The main purpose of geostatistics is to describe the spatial patterns of the measuring variables and interpolate any uncertain variables at an unobserved location. There are several such geostatistical tools, but kriging is a one of the better-known geostatistics schemes. Krige (1951) first proposed this method to estimate mineral resources for the mining industry; Matheron (1963) named the method kriging. Kriging can be categorized as outlined below (Goovaerts, 1997).

- Simple Kriging (SK): the most basic kriging process. In this method, the data trend is assumed to be constant and the mean value is known. SK does not constrain the weights.
- Ordinary Kriging (OK): similar to SK. OK constrains the sum of the weights to be 1.0 and estimates the local constant mean of each estimation point.
- Universal kriging (UK): useful when the data have a strong and easily modeled trend.
- Co-kriging: an extended kriging that estimates one variable from two variables.

The main premise in kriging is that the neighboring measuring points have more weighted predictions that will improve the interpolation. In order to use kriging to

interpolate the target values at an unsampled location, the spatial pattern of the measuring samples is characterized by descriptive tools such as variograms or semivariograms.

A variogram shows the similarities between filed variables at two points; a semivariogram is half of a variogram. A variogram of the two random variables, $Z(x)$ and $Z(x+h)$, of two points, x and $x+h$, is calculated as:

$$2\gamma(h) = E\left[\left[Z(x+h) - Z(x)\right]^2\right] = Var\left[Z(x+h) - Z(x)\right] \quad (6.31)$$

And a semivariogram, $\gamma(h)$, is defined as:

$$\gamma(h) = \frac{1}{2} Var\left[Z(x+h) - Z(x)\right] \quad (6.32)$$

A semivariogram depends upon the distance, h, called "lag", between two spatial locations; it shows the decrease in similarity between two random variables as the lag, h, increases. A semivariogram is defined by the parameters described below :

- Range: the lag distance at which the spatial correlation is practically zero.
- Sill: the semivariogram value at the range where the curve levels off.
- Nugget: if the semivariogram value is not zero when the lag is close to zero, the initial semivariogram value is a nugget.

These parameters are illustrated in Figure 6.1. Figure 6.2 and Table 6.1show certain semivariogram models and equations.

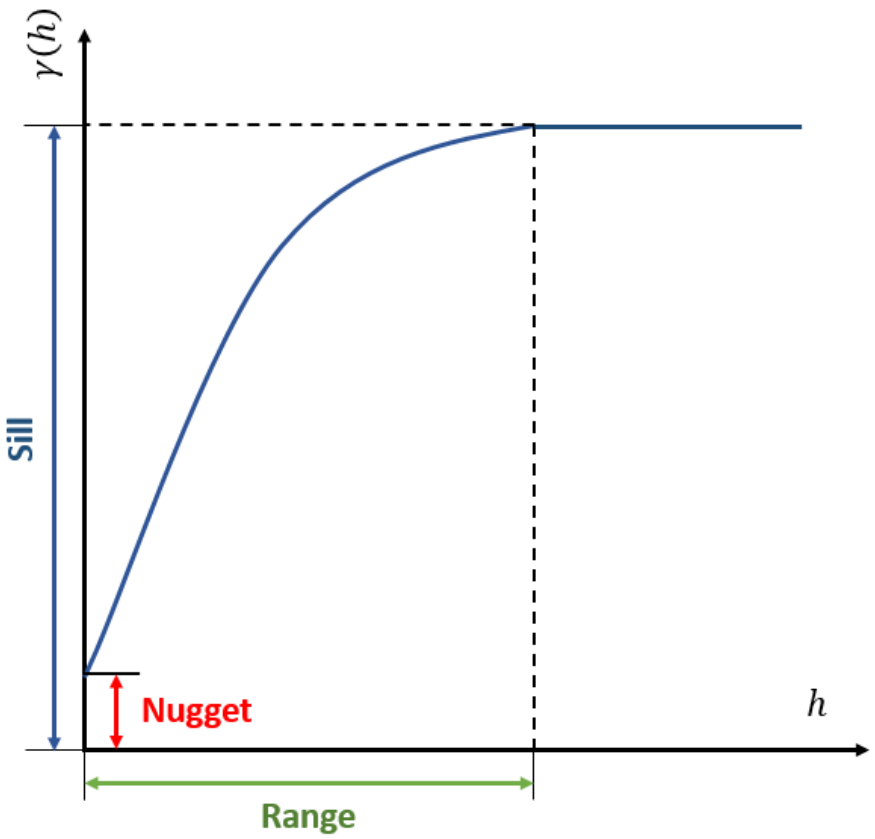

Figure 6.1 Parameters of semivariogram

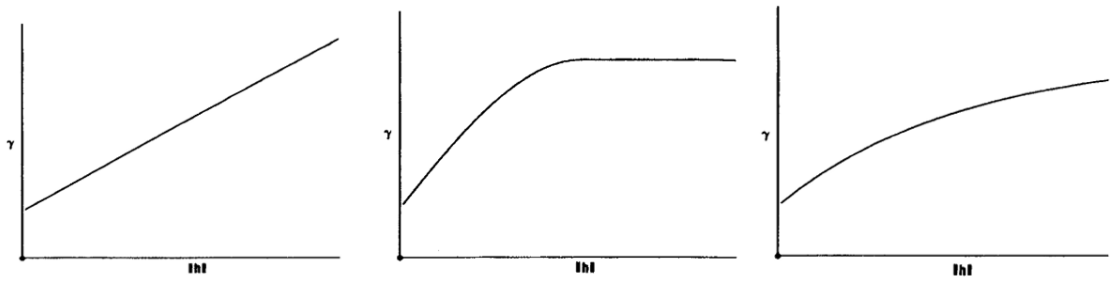

(a) Linear model (b) Spherical model (c) Exponential model

Figure 6.2 Semivariogram models

Table 6.1 Semivariogram models and equations

Variogram model	Semivariogram, $\gamma(h)$
Linear	$\gamma(h)=\begin{cases} Ch & ,h>0 \\ 0 & ,h=0 \end{cases}$
Spherical	$\gamma(h)=\begin{cases} C\left(\frac{3}{2}\frac{h}{a}-\frac{1}{2}\left(\frac{h}{a}\right)^3\right) & ,0\le h<a \\ C & ,a\le h \\ 0 & ,h=0 \end{cases}$
Exponential	$\gamma(h)=\begin{cases} C\left[1-\exp\left(-\left(\frac{h}{a}\right)^2\right)\right] & ,0\le h<a \\ 0 & ,h=0 \end{cases}$

6.5 Stress-Induced Aperture Changing Calculation

6.5.1 Stress Transformation

The normal and shear stresses at the middle points of the arbitrarily-inclined fracture segments were calculated from interpolated nodal stresses by the stress transformation wedge method, as shown in Figure 6.3.

The inclined angle of the fracture segment was measured to be a positive and counterclockwise angle from the x-axis, as shown in Figure 6.3 (a). In Figure 6.3 (b), σ_{nn} and τ_{nt} represent the normal and shear stresses, respectively, acting on the fracture plane. The force wedge in Figure 6.3 (c) was obtained by multiplying the stresses by the areas of the planes. Using the equilibrium of forces on the force wedge in the n-direction, the normal and shear stresses with the *n* and *t* coordinate system, σ_{nn} and τ_{nt}, were expressed as:

$$\sigma_{nn} = \sigma_{xx}\cos^2\theta + \sigma_{yy}\sin^2\theta + 2\tau_{xy}\sin\theta\cos\theta$$

$$\tau_{nt} = -\sigma_{xx}\cos\theta\sin\theta + \sigma_{yy}\sin\theta\cos\theta + \tau_{xy}\left(\cos^2\theta - \sin^2\theta\right) \quad \text{..... (6.33)}$$

Eq. 6.33 could then be rewritten in terms of the double angle, :

$$\sigma_{nn} = \frac{\sigma_{xx}+\sigma_{yy}}{2} + \frac{\sigma_{xx}-\sigma_{yy}}{2}\cos 2\theta + \tau_{xy}\sin 2\theta$$

$$\tau_{nt} = -\frac{\sigma_{xx}-\sigma_{yy}}{2}\sin 2\theta + \tau_{xy}\cos 2\theta \quad \text{..... (6.34)}$$

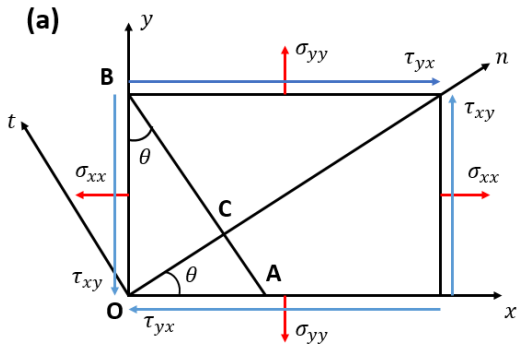

a) Stress cube

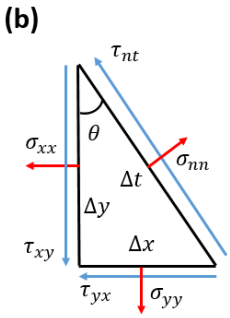

b) Stress wedge

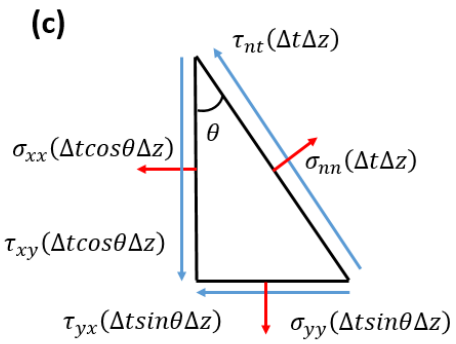

c) Force wedge

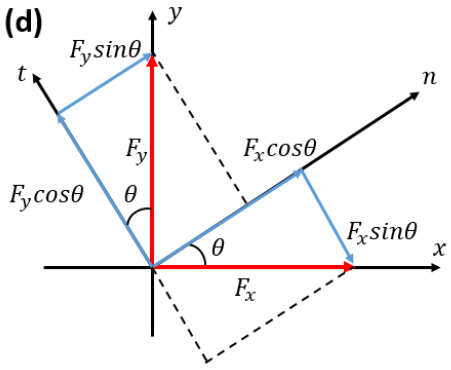

d) Resolution of force components

Figure 6.3 Stress transformation.

6.5.2 Calculation of the Stress-Induced Aperture Changes

The fracture aperture changes were divided into two parts: normal aperture changes by normal stiffness, k_n, which represented the rate of change in the normal stress, σ_n, to the normal displacement; and shear aperture changes by shear stiffness, k_s, which represented the rate of the change in shear stress, τ_n, to the shear displacement. It is known that pore pressure acts against normal aperture closings under normal compressive conditions (Bandis et al., 1983; Barton et al., 1985; Zhang, 2013). In other words, under the same in-situ confining stress conditions, decreasing the pore pressure results in an increase in the effective stress on the rock. This increase in effective stress causes a compaction of the rock and aperture closing.

Usually, normal aperture deformation shows nonlinear characteristics under normal stress conditions. Figure 6.4. illustrates the description of the relationship between normal stress and normal displacement of intact and jointed rock. In this research, because the rock joints/fractures were much weaker than the intact rocks, the jointed rock showed a larger displacement than the intact rock with the same normal stress conditions. The normal stiffness was a slope of the normal stress and displacement curve. As shown in Figure 6.4, the normal stiffness of the jointed rock, $k_{n,jointed}$, was smaller than the normal stiffness of the intact rock, $k_{n,intact}$. Because the effective stress changes could only affect the rock structure deformation, the normal stiffness was expressed using the effective stress and normal displacement:

$$k_n = \frac{\Delta\sigma'_n}{\Delta v_n} \quad \text{..... (6.35)}$$

where, Δ denotes an increment, σ'_n is the effective normal stress, and v_n is the normal displacement.

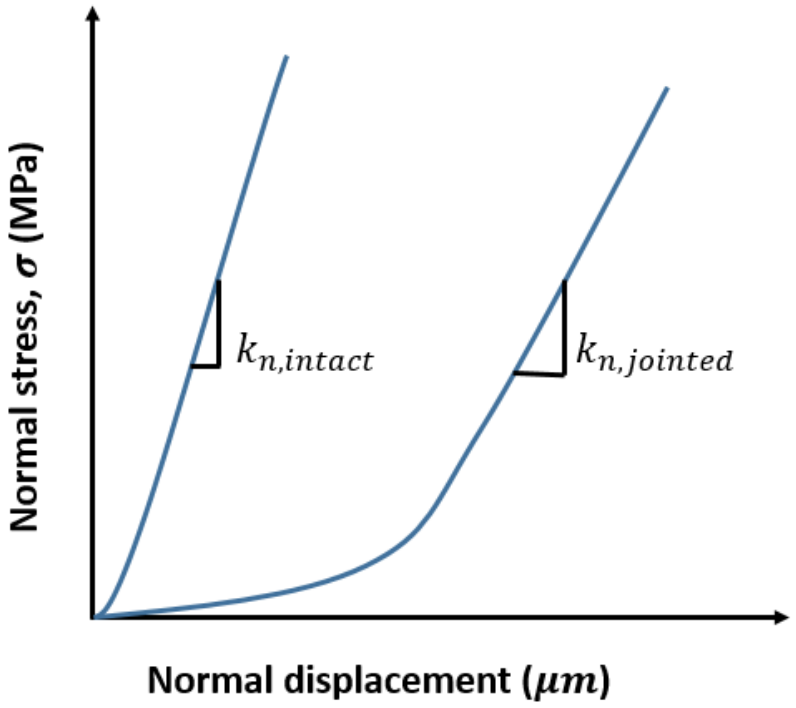

Figure 6.4 Normal stress and displacement relationship of intact and jointed rock.

Figure 6.4 also shows that the normal stiffness, k_n, was small with a low level of normal stress, but it increased rapidly as the normal stress increased. Goodman (1976) proposed the empirical relationship of the nonlinear normal aperture closure, v, to the normal stress, σ_n, as:

$$\sigma_n = \sigma_{ni}\left[1+\left(\frac{v}{v_m - v}\right)^t\right] \quad \text{..... (6.36)}$$

where σ_{ni} is the initial normal stress, v_m is the maximum possible fracture closure, and t is a dimensionless empirical exponent.

Bandis et al. (1983) propose`d a joint model that is now widely used for joint normal closure calculations. This model is described as:

$$\sigma'_n - \sigma'_{ni} = \frac{v}{a - bv} \quad \text{..... (6.37)}$$

where a and b are empirical constants. When v is equal to a/b, the denominator becomes zero and σ'_n has an infinite value. When σ'_n has an infinite value, v approaches the maximum value, v_m, and can be expressed as:

$$v = \frac{a}{b} = v_m \quad \text{..... (6.38)}$$

Bandis et al. (1983) expressed the normal stiffness, k_n, by taking the first derivation of σ'_n with respect to v to be:

$$k_n = \frac{\partial(\sigma'_n - \sigma'_{ni})}{\partial v} = \frac{1}{a\left(1-\frac{bv}{a}\right)^2} \quad \text{..... (6.39)}$$

Eq. 6.39 then be expressed as a function of the effective normal stress:

$$k_n = \frac{\left(\sigma'_n + k_{ni} v_m\right)^2}{k_{ni} v_m^2} \quad \text{..... (6.40)}$$

When v is zero, the initial normal stiffness, k_{ni}, can be expressed as $k_{ni} = \frac{1}{a}$.

Using Eq. 6.38, Eq. 6.37 can then be rewritten as:

$$\sigma'_n = \frac{k_{ni} v}{\left(1 - v / v_m\right)} = \frac{k_{ni} v \cdot v_m}{v_m - v} \quad \text{..... (6.41)}$$

where σ'_n is the effective stress and k_{ni} is the initial normal stiffness. The normal displacement, v, can then be rewritten as:

$$v = \left(\frac{k_{ni}}{\sigma'_n} + \frac{1}{v_m}\right)^{-1} \quad \text{..... (6.42)}$$

Bandis et al. (1983) proposed the relationship of the initial normal stiffness, k_{ni}, as follows:

$$k_{ni} \approx -7.155 + 1.748 JRC + 0.0178\left[\frac{JCS}{v_i}\right] \quad \text{..... (6.43)}$$

where k_{ni} has a unit of MPa/mm, JCS is the joint roughness coefficient, JCS is the joint wall compressive strength in Mpa and v_i is the initial aperture in mm at the beginning of the loading. The variable v_i can then be estimated by:

$$v_i = JRC\left(\frac{0.04\sigma_c}{JCS} - 0.02\right) \quad \text{..... (6.44)}$$

where σ_c is the unconfined compressive strength of the rock. The maximum allowable closure in mm can be estimated by:

$$v_m = -0.296 - 0.0056JRC + 2.241\left(\frac{JCS}{v_i}\right)^{-0.245} \quad \text{..... (6.45)}$$

JRC is the number showing the appearance of the joint surface; the value was estimated with scale corrections. Barton and Choubey (1977) described the typical discontinuity roughness profiles and associated JRC values.

If the joint was not weathered, the JCS was equal to the unconfined compressive strength of the rock, σ_c. If there was weathering along the joint, the JCS was less than σ_c. Barton and Choubey (1977) suggested an empirical expression to estimate the JCS, using the Schmidt hammer rebound test. This expression is as follows:

$$\log JCS \approx 0.88\gamma R_{n(L)} + 1.01 \quad \text{..... (6.46)}$$

where γ is the unit weight of the rock $\left(MN/m^3\right)$ and $R_{n(L)}$ is the rebound number from the L-type Schmitt hammer test on the joint surface. The JCS variable has a unit of MPa and a range of 20 to 300 MPa.

Bandis et al. (1983) described the deformation characteristics of five different kinds of rock joints. They defined the non-linear behavior of a fracture's normal deformability through various loading/unloading laboratory tests with fresh and weathered joints, and then argued that fracture deformation was controlled by the

aperture, Joint Roughness Coefficient (JRC), and Joint Compressive Strength (JCS). They compared the test results of the intact rock and rock joint, and then described the relationship of the normal stress, σ_n, with the normal fracture deformation, ΔV. The slope of the curve represents the normal stiffness, k_n. They also compared test results for different kinds of fresh and weathered rock joints, and illustrated the relationship between the normal stress and displacement. It can be seen that clean joints showed similar curve behaviors under loading and unloading conditions, whereas weathered joints showed a significant difference, especially under low stress. Therefore, in this study, a clean joint condition was assumed and the same normal stiffness was used for the aperture opening/closing calculation.

6.6 The Belridge and Lost Hills (LH) Oil Fields in California

For the stress-sensitive reservoir case study, I considered the Belridge and Lost Hills (LH) oil fields in California, as shown in Figure 6.5. The Belridge and LH fields have suffered from large production-induced subsidence problems. For example, in 1995, LH showed about a $0.5\ ft$ subsidence during 100 days, and a total $30\ ft$ subsidence from 1925 to 1977 (Bruno & Bovberg, 1992; Xu, 2002). Large numbers of wells in the Belridge and LH fields have failed due to such significant subsidence. However, diatomite, the main reservoir source rock, is a unique rock; so far, it is very challenging work to investigate its characteristics and subsidence mechanisms. It was very difficult to obtain the total reservoir property data relating to the Belridge and LH fields through a

literature review. Some of the literature provided only a wide range of values for some of the diatomite properties. Table 6.2 shows some of the key parameters of the diatomite reservoirs at the Belridge and LH fields. The fields showed low matrix permeability and low Young's modulus. Therefore, I tried to choose reasonable property values for this study, based on the literature.

Table 6.2 Key parameters of the diatomite reservoirs of the Belridge and LH fields

	Young's modulus $[psi]$	Permeability $[mD]$	Oil viscosity $[cp]$	Reservoir pressure $[psi]$	Poisson ratio
(Bruno & Bovberg, 1992)	$1.0E5$				0.16 ~ 0.25
(Fast et al., 1994)	$1.8E5 \sim 2.7E5$				0.3 ~ 0.35
(Wright et al., 1995)	$5E4 \sim 2E5$	0.1 ~ 2			
(Xu, 2002)	$7.3E3$	1.5 ~ 2000	1 ~ 96	50 ~ 850	
(Dobson, 2014)	$2E4 \sim 5E5$	0.03 ~ 103			

	Fluid compressibility $\left[psi^{-1}\right]$	Pore volume compressibility $\left[psi^{-1}\right]$	Bulk compressibility $\left[psi^{-1}\right]$	Porosity
(Bruno & Bovberg, 1992)		$20 \sim 200E-6$	$18 \sim 30E-6$	
(Fast et al., 1994)				
(Wright et al., 1995)				0.4 ~ 0.6
(Xu, 2002)	$5.5E-6$			0.25 ~ 0.4
(Dobson, 2014)				0.36 ~ 0.7

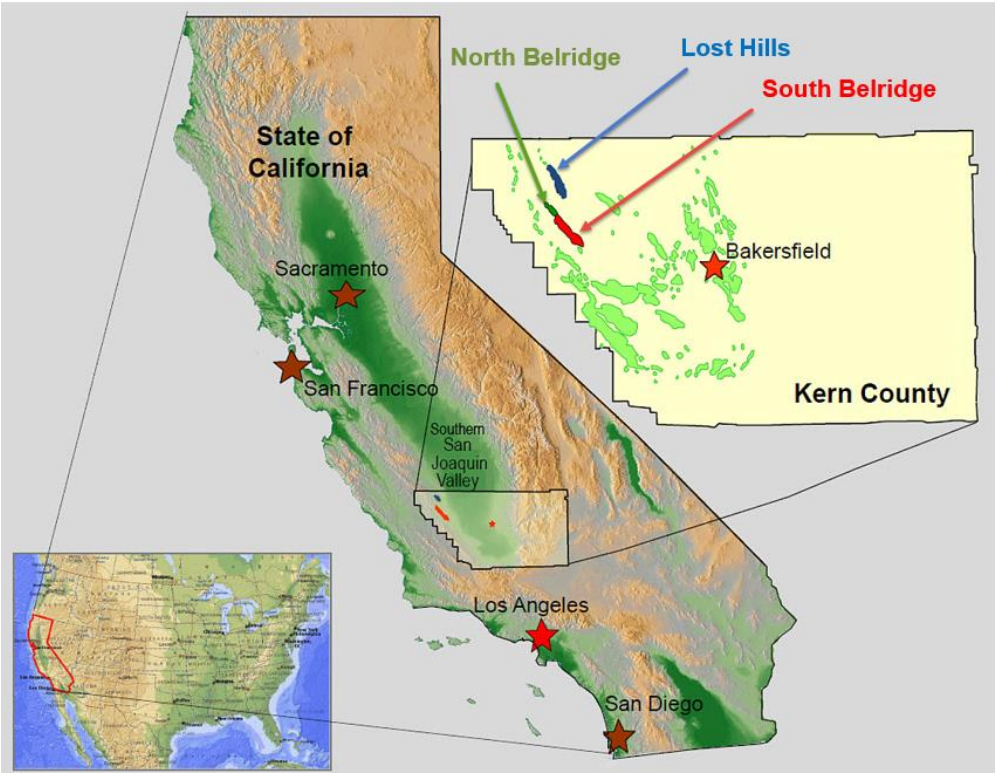

Figure 6.5 Belridge and Lost Hills oil fields in California

However, because the initial normal stiffness, k_{ni}, and JCS data of for diatomite were not available, the normal stiffness could not be estimated using Eq. 6.40. As an alternative, even though it was not associated with the diatomite field in California, I considered Yamamoto et al. (2007). These researchers investigated the geological properties of a diatomaceous siliceous Koetoi formation in Japan, and their research provided useful unconfined compressive strength data. Some of the key parameters are listed in Table 6.3. They showed that the unconfined compressive strength ranged 3 and 24 *Mpa* along the depth.

Table 6.3 Key parameters of diatomaceous siliceous sediments of a Koetoi formation in Japan

Young's modulus $[psi]$	Porosity	Unconfined compressive strength $[Mpa]$
$2.9E4 \sim 5.8E5$	$0.4 \sim 0.65$	$2 \sim 23$

Even though the listed properties of the diatomaceous rock of Japan were not enough numbers to prove that diatomaceous rock of Japan is similar with diatomite rock of California, they showed similar range of Young's modulus and porosity values as shown in Table 6.2. Therefore, I adopted these unconfined compressive strength values for the SIPC coupling simulation. For that, instead of using single value, I assumed 5 different JCS values as 5, 10, 20, 30 and 40 Mpa in Stress-Induced Permeability Changing (hereafter referred to as the SIPC) coupling simulation.

In this study, if the curve of the normal stress and displacement was not available; the normal stiffness, k_n, of the joint was calculated using Eq. 6.40. Then, the aperture changes were determined using kriging interpolated stresses and the estimated normal stiffness.

For the SIPC coupling simulation, it was assumed that the stress of the middle point of the fracture segment represented the stress condition along the plane of the fracture, and was equally deformed in each sub-domain. Also, the JRC and JCS of the fracture were assumed to be uniform for all the fractures.

6.7 Coupling Simulation Procedure

1. The fluid flow in the porous media was computed by the fluid flow FDM using the Newton-Raphson iteration. The MRST was used for the fluid flow simulator.
2. The pore pressure data calculated by the MRST were passed to the geomechanics FEM simulator to calculate the stress and volumetric strain changes. A Q4 rectangular element and the same shaped functions were used to calculate the pore pressure and displacement.
3. In the coupling simulation, true porosity was calculated by the geomechanics FEM; Eq. 6.19 was used to convert the volumetric strain change to the reservoir porosity for coupling with the fluid flow FDM simulator. In the stress-induced aperture-changing coupling simulation, the fracture porosity was calculated using stress-induced aperture deformation and fracture geometry data.
4. Porosity was the coupling parameter; the iteration was repeated until the convergence level was below the desired tolerance level. If the porosity was not converged, the porosity data were passed to the MRST fluid flow simulator.
5. In the SIPC simulation, the normal and shear stresses at these middle points of the fracture segments in each grid were interpolated from the calculated nodal stresses using an ordinary kriging scheme. The initial normal stiffness and maximum allowable deformation were calculated using the initial aperture distribution data. Then, the normal stiffness values of the fracture and rock were calculated using the interpolated normal stress of each fracture segment.

6. In the coupling simulation, the equivalent permeability was updated using Eq. 6.11. In the SIPC simulation, the aperture openings/closings were calculated using the estimated normal stiffness and normal stress data. Then, the directional equivalent permeability values were calculated via the Oda method, using updated aperture and fracture geometry data.

CHAPTER VII

NUMERICAL EXPERIMENTS

7.1 Case I - Verification of the Coupling Simulator

To verify the coupling codes, Terzaghi's one-dimensional, one-way drained consolidation problem was simulated.

The basic assumptions of Terzaghi's 1D consolidation problem are:

1. The soil is homogeneous and fully saturated.
2. The solid particles and fluid are incompressible.
3. The fluid flow and soil compression are one-dimensional (vertical).
4. Darcy's law is valid and the strains are small.
5. Permeability and volume compressibility are constant.

The governing differential equation of Terzaghi's 1D consolidation is expressed as (Karl Terzaghi, 1926; 1943; Verruijt, 2001; Pan, 2009):

$$\frac{\partial p}{\partial t} = C_v \frac{\partial^2 p}{\partial z^2} \quad \text{..... (7.1)}$$

In this equation:

$$C_v = \frac{k}{r_w m_v} \quad \text{..... (7.2)}$$

$$m_v = \frac{a_v}{1+e} \quad \text{..... (7.3)}$$

$$a_v = -\frac{\partial e}{\partial \sigma'} \quad \text{..... (7.4)}$$

where C_v is the coefficient of the consolidation, z is the drainage distance, m_v is the volume compressibility coefficient, a_v is the coefficient of compressibility, and e is the void ratio.

The analytical solution to Terzaghi's 1D consolidation problem was described by Verruijt Verruijt (1995). The relationship between drainage distance and total height is shown in Figure 7.1, below.

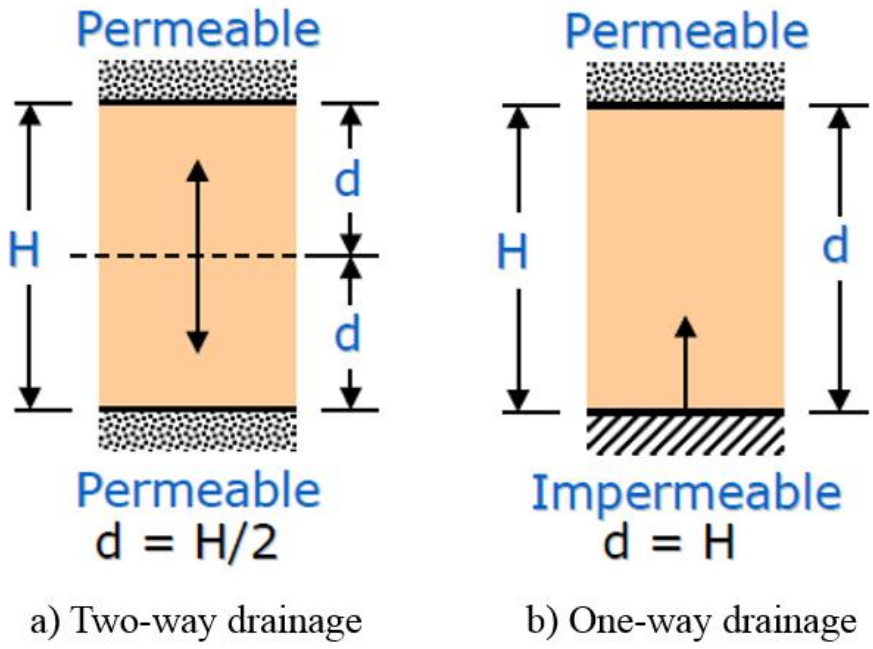

Figure 7.1 Drainage distance vs. total height.

The analytical solutions with double and single drainage are given in Figures 7.2 (a) and (b), respectively.

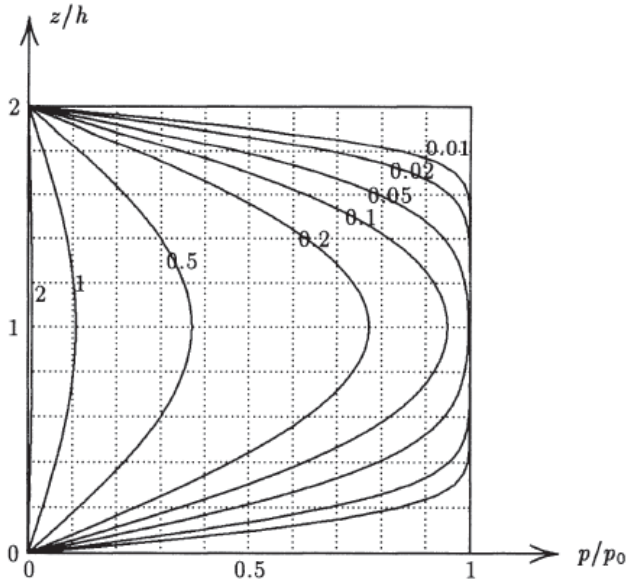

a) Analytical solution to Terzaghi's consolidation problem with two-way drainage

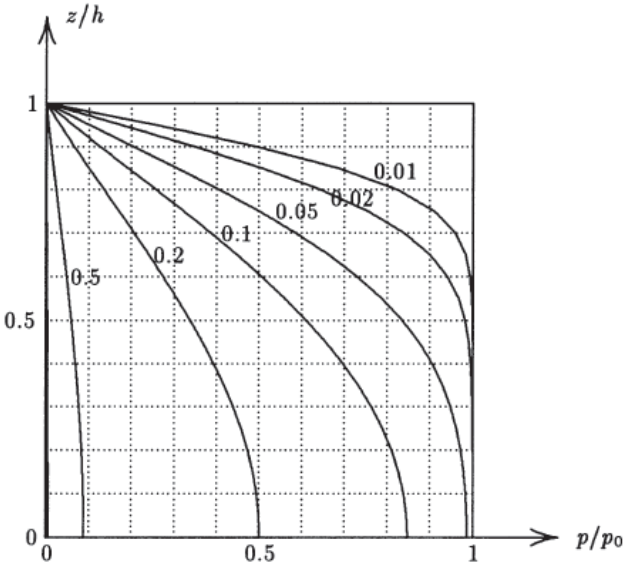

b) Analytical solution to Terzaghi's consolidation problem with one-way drainage

Figure 7.2 Analytical solution to Terzaghi's 1D consolidation problem.

As shown in Figure 7.3, a comparison of the numerical and analytical solutions showed a good match.

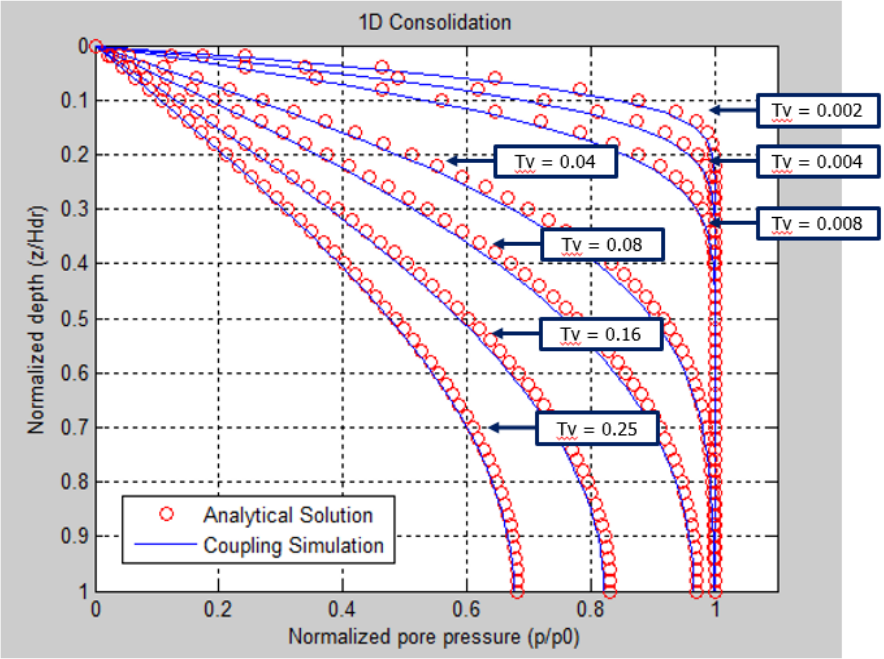

Figure 7.3 Comparison of the numerical and analytical solutions to Terzaghi's 1D consolidation problem with one-way drainage.

In the results, time factor, T_v, is expressed as:

$$T_v = \frac{C_v t}{d^2} \quad \text{(7.5)}$$

7.2 Case II – Fracture Geometry Effect on Equivalent Permeability Estimation

In order to study fracture geometry's effect on the permeability estimation, the x- and y-directional equivalent permeability distributions were calculated with different fracture network orientations.

To testify to the anisotropy of the fracture permeability, I considered more y-directional than x-directional fractures; the y-directional permeability was expected to be larger than the x-directional permeability, due to fracture geometry. I generated three differently oriented fracture sets. The first had a $20°$ fracture orientation and 40% existence probability. The second had an $80°$ fracture orientation and 30% probability. The third had a $110°$ fracture orientation and 20% existence probability. The aperture distributions followed a normal distribution; the mean aperture was 1 mm and the standard deviation was 0.3 mm. In this study, a metric unit was used for the aperture distribution because the modified Oda's algorithm used a metric unit to calculate the equivalent permeability. The input data for the Fractal Discrete Fracture Network (FDFN) generation are given in Table 7.1.

Table 7.1 Input data for the FDFN generation

Domain size	1000×1000	*ft*
Minimum fracture length	15	*ft*
Fractal center dimension, FD_c	1.9	
Fractal length dimension, FD_l	1.3	
Fracture density term, α	0.35	
Aperture (Normal distribution)		
Mean	1	*mm*
Standard deviation	0.3	*mm*
Fracture set 1		
Fracture orientation	20°	
Probability	0.4	
Fracture set 2		
Fracture orientation	80°	
Probability	0.3	
Fracture set 3		
Fracture orientation	110°	
Probability	0.3	

Because the FDFN codes used fractal and statistical methods, they generated different fracture network distributions in each simulation, even though the same input data were used. Therefore, I used a 1,000-times Monte Carlo simulation to generate the FDFN; the fracture density and fracture numbers for each generated fracture network were calculated to generate a Cumulative Distribution Function (CDF) plot. From the CDF plot, I selected P10, P50, and P90 fracture network distribution maps, as shown in Figure 7.4. The P50 fracture map was selected to represent the fracture network condition of the reservoir, and was used to calculate the equivalent permeability distributions. The number of generated fractures in the P50 fracture map was 2,347.

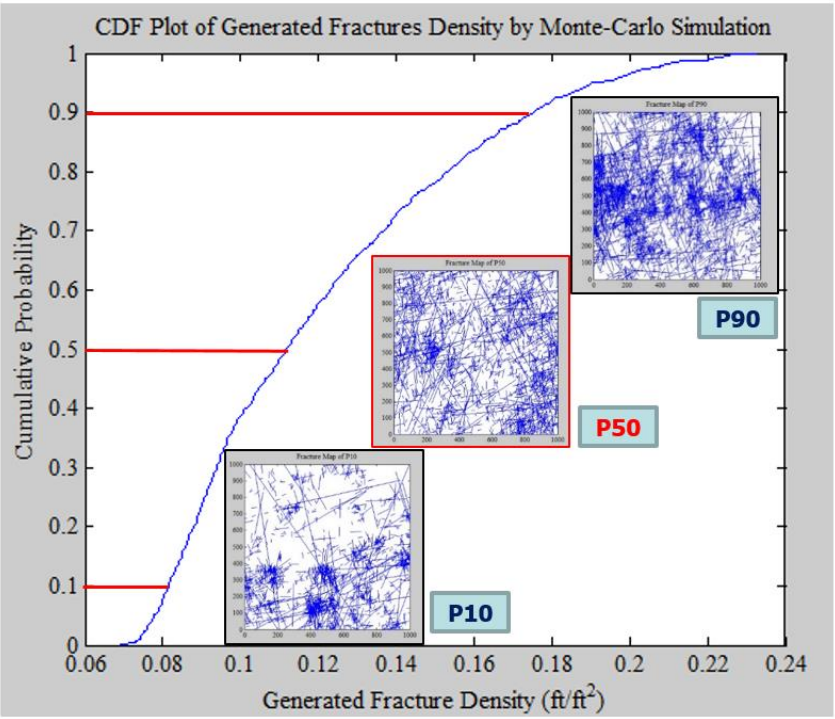

Figure 7.4 CDF plot of the fracture density generated by the Monte Carlo simulation.

Figure 7.5 shows the sampled fractures array with aperture segment numbers. Ten of the generated 2,347 fractures were randomly selected and equally arranged along a y-axis such that they did not overlap with one another, and so the x-axis showed the numbers of aperture segments distributed along each fracture.

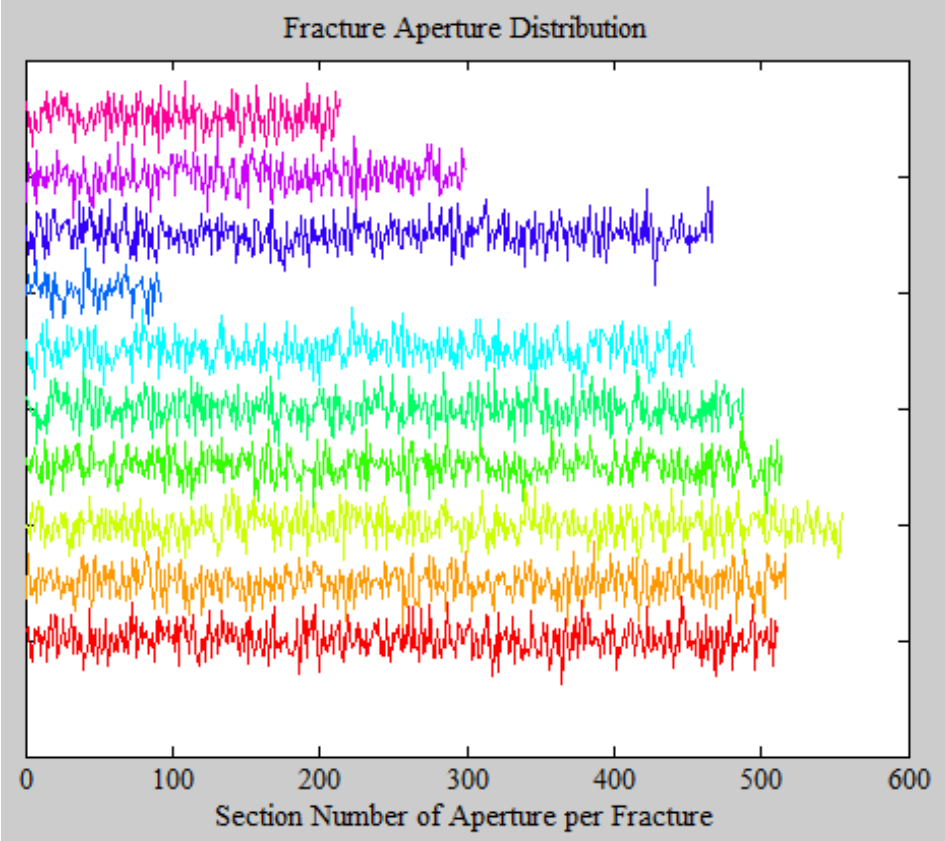

Figure 7.5 Aperture distribution of fractures generated by FDFN codes.

The natural-like aperture distribution was simplified as a set of consecutive rectangular cells, and the fracture porosity was calculated using the aperture distribution and fracture length data. After that, a single averaged aperture value for each fracture

was calculated and assigned to the equivalent permeability estimation for the case study. Each fracture had a different single averaged aperture value, depending upon the fracture geometry, but the distribution of the total averaged apertures of all of the fracture networks also followed a normal distribution, as shown in Figure 7.6. The calculated fracture porosity was 0.002; this value was added to the matrix porosity for the coupling simulation.

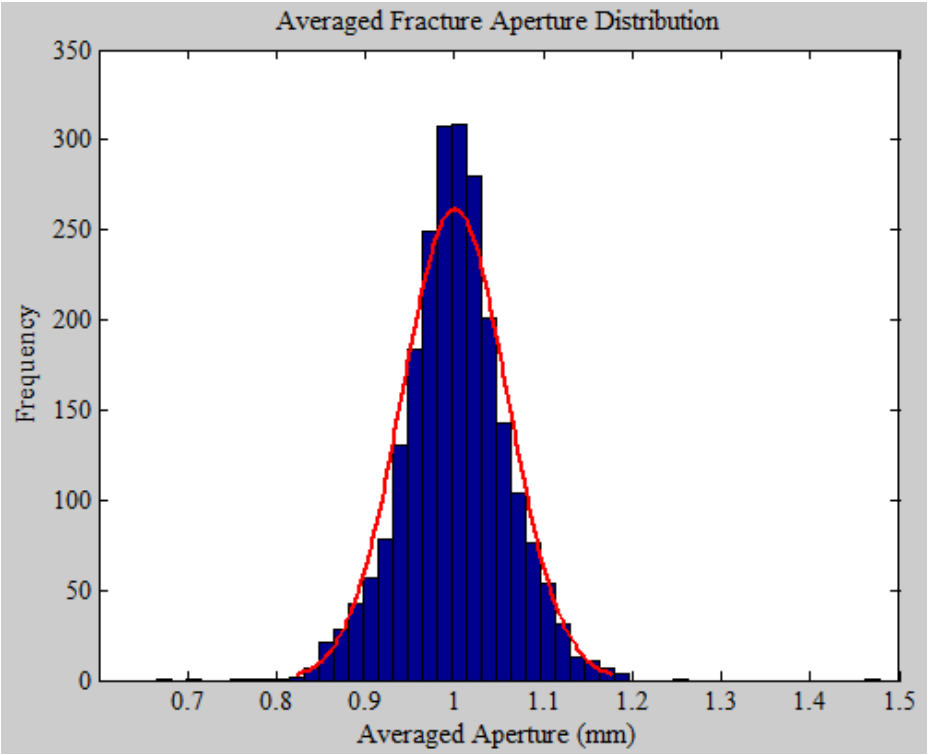

Figure 7.6 Averaged aperture distribution of the P50 fracture map.

To select the domain size for the simulation, I performed a REV simulation. For the REV, the lateral size of the screen window (the red square) located in the middle of the domain was expanded from 1 to the domain's side length, 1000 ft, as shown in

Figure 7.7. Then, the x- and y-directional equivalent permeability distributions for each screen window were calculated and plotted together. As shown in Figure 7.8, a $950\times950\ ft$ screen window had a REV, and a $950\times950\ ft$ domain was selected for the simulation. As was previously expected, the y-directional equivalent permeability was larger than the x-directional value, due to the fracture network geometry effect. The REV simulation result showed approximately a $1100\ mD$ average permeability difference between the x- and y-directional permeabilities.

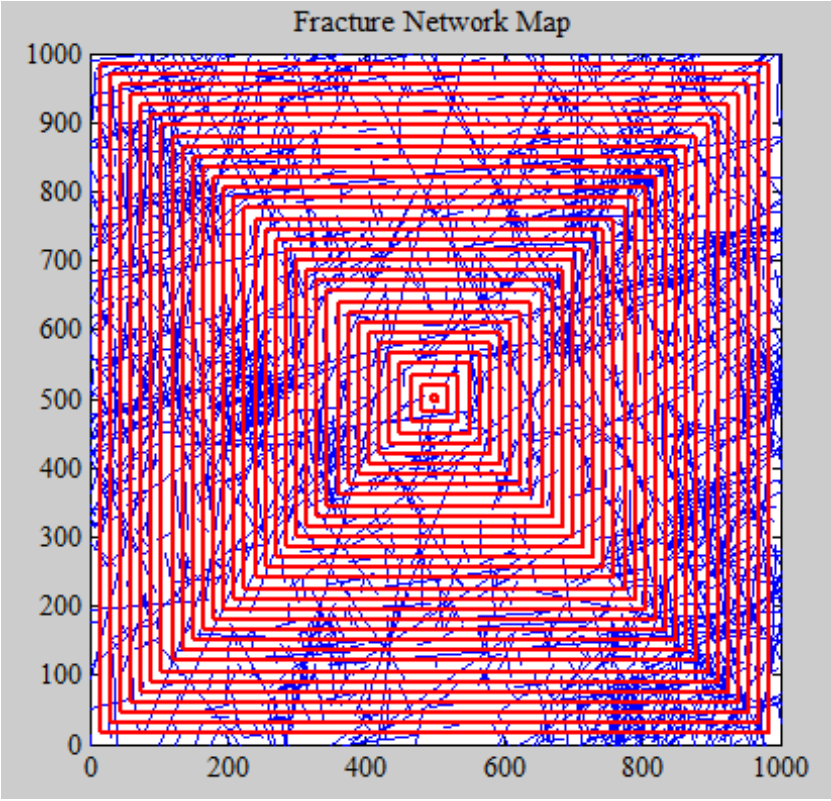

Figure 7.7 Screen widow expansion for REV calculation

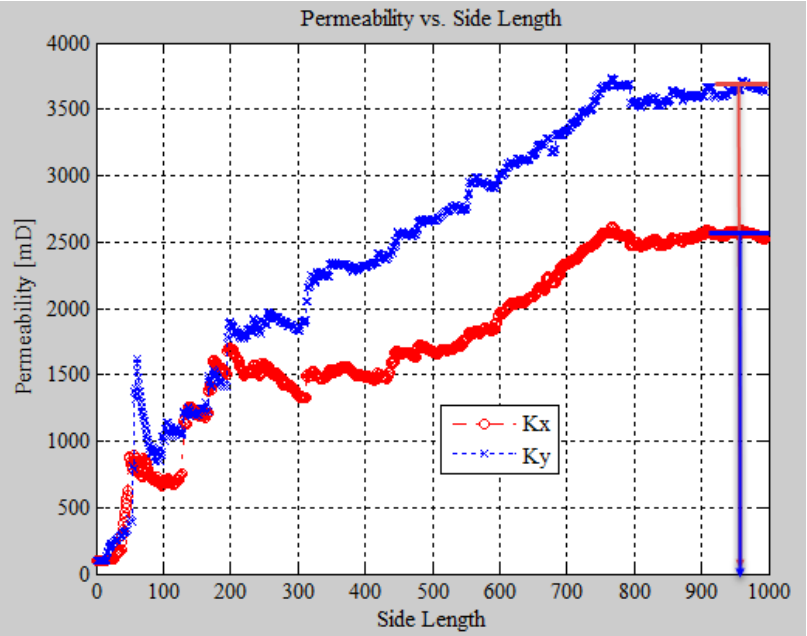

Figure 7.8 The x- and y-directional equivalent permeability calculation with a different screen window size.

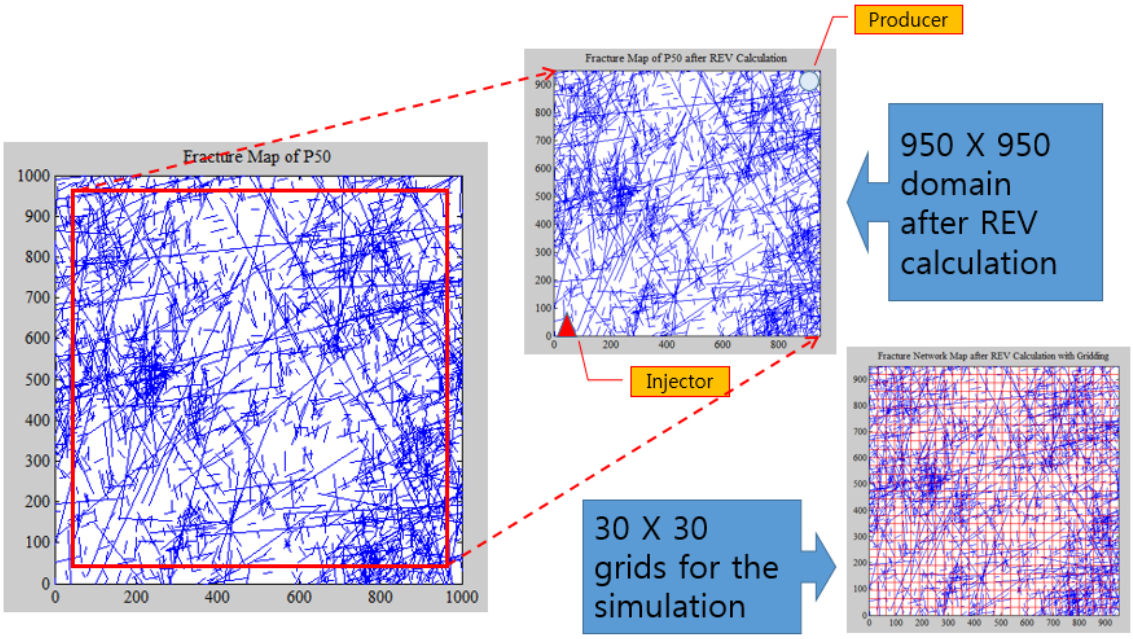

Figure 7.9 Selected domain size and grid numbers for the simulation.

I used 30×30 grids to calculate the equivalent permeability. Figure 7.9 shows the selected domain size by the REV and grid numbers for the simulation.

Figures 7.10 and 7.11 show the calculated regular and log-scaled directional equivalent permeability distributions with 30×30 grids, respectively. I calculated the log-scaled permeability distribution, as shown in Figure 7.11, to emphasize the permeability difference. I also highlighted the high permeability zones and linked them with the fracture domain map. As shown in the results, the equivalent permeability simulation successfully reflected the heterogeneous characteristics of the fracture geometry and fracture clustering. The simulation results also indicated a larger y-directional permeability distribution than the x-directional value.

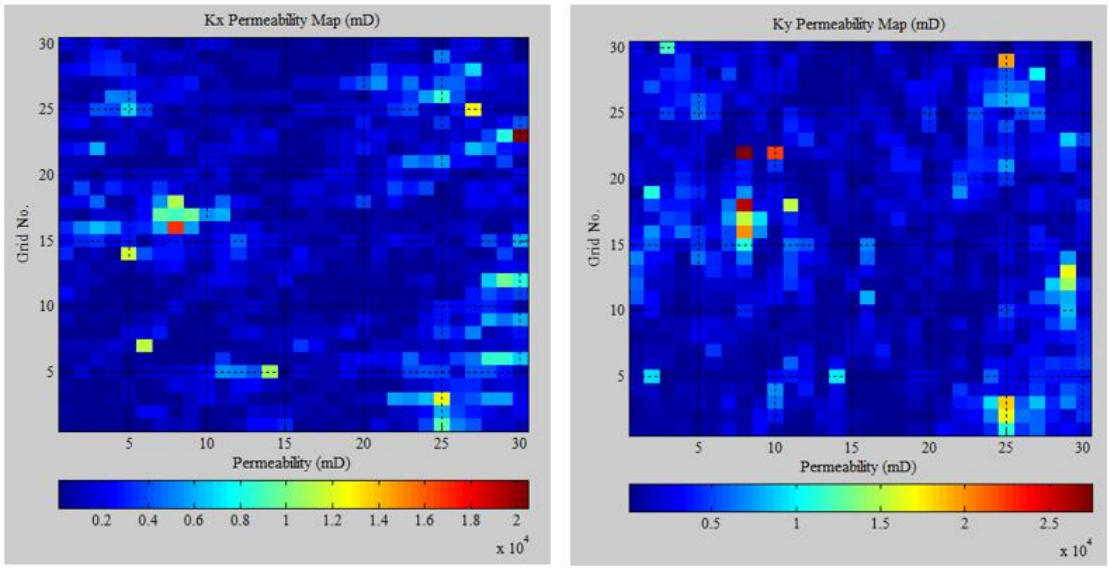

e) x-directional permeability f) y-directional permeability

Figure 7.10 The x- and y-directional equivalent permeability calculation results using FDFN information.

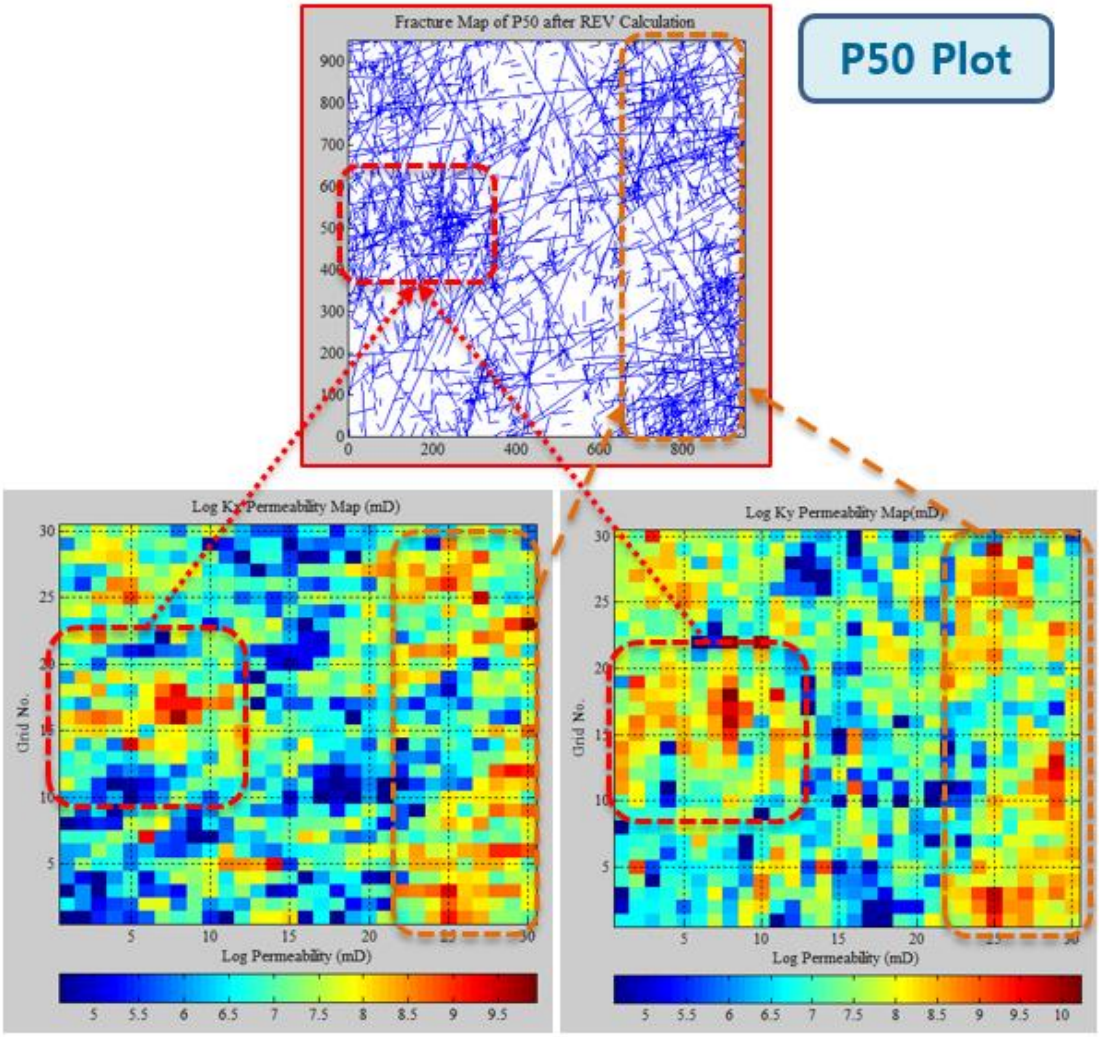

Figure 7.11 Log-scaled x- and y-directional equivalent permeability calculation results using FDFN information.

7.3 Case III – 2D 5-Spot Pattern Flow Simulation with More X-Directional Fracture Sets

In this case study, a two-dimensional 5-spot pattern two-phase fluid flow was simulated. Equivalent permeability was estimated by a modified Oda's algorithm, and

more x-directional fractures were considered. I used two differently oriented fracture sets. One had a $10°$ fracture orientation and 50% existence probability, and the other had a $170°$ fracture orientation and 50% probability. Figure 7.12 shows a rose diagram of the generated fractures. The aperture distribution followed a normal distribution with a 0.5 mm mean aperture and 0.25 mm standard deviation, as shown in Figure 7.13. Figure 7.14 shows a sampled fractures array with aperture segment numbers. For the sake of simplicity, a lower aperture density was considered for the SIPC coupling simulation. Input data for the FDFN generation are given in Table 7.2.

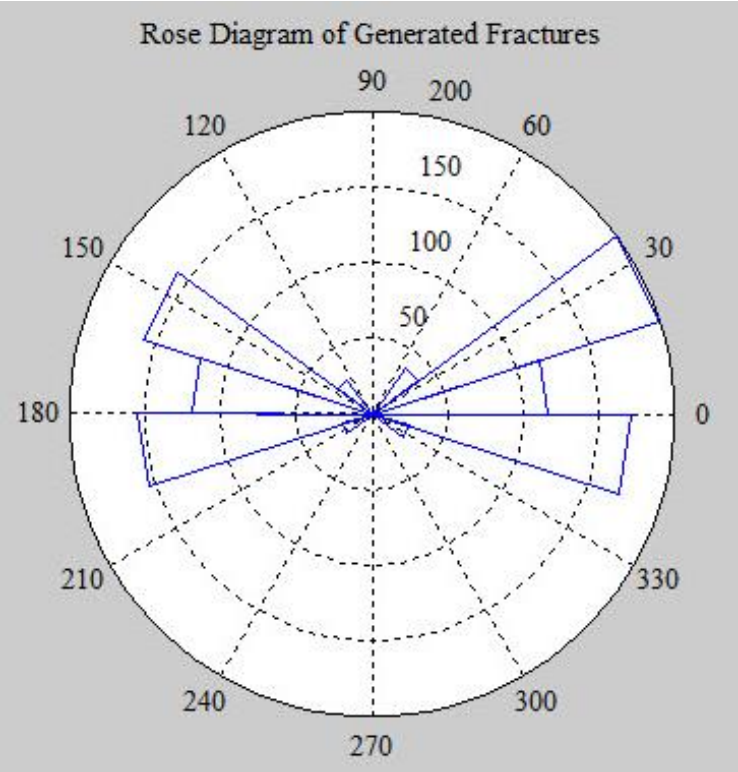

Figure 7.12 Rose diagram of the generated fractures.

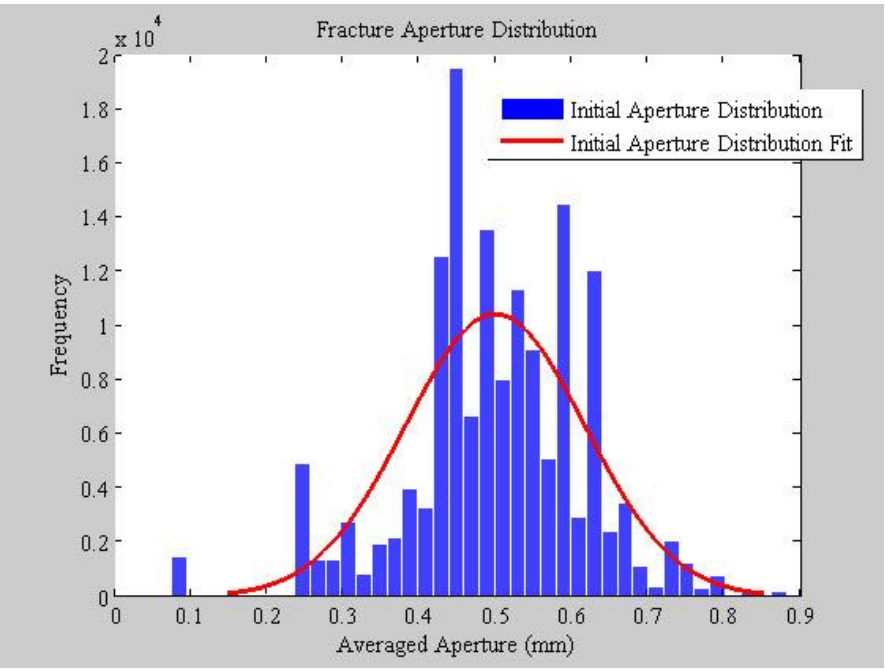

Figure 7.13 Initial aperture distribution.

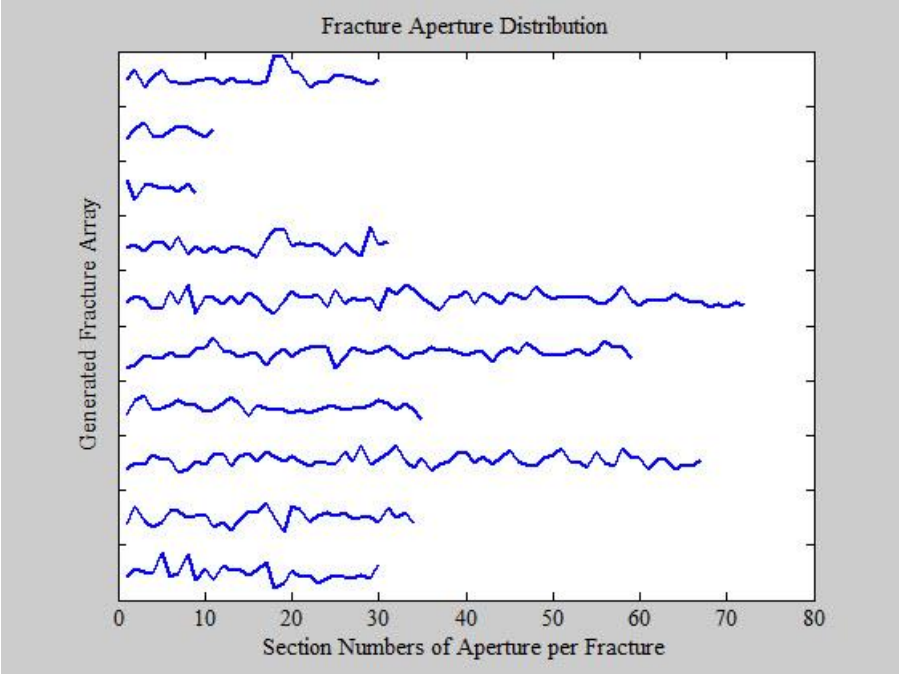

Figure 7.14 Array of ten sampled fractures with aperture distributions.

Table 7.2 Input data for the FDFN generation of the 5-spot pattern simulation

Domain size	700×700	*ft*
Minimum fracture length	10	*ft*
Fractal center dimension, FD_c	1.9	
Fractal length dimension, FD_l	1.5	
Fracture density term, α	0.5	
Aperture (Normal distribution)		
Mean	0.5	*mm*
Standard deviation	0.25	*mm*
Fracture set 1		
Fracture orientation	10°	
Probability	50	%
Fracture set 2		
Fracture orientation	170°	
Probability	50	%

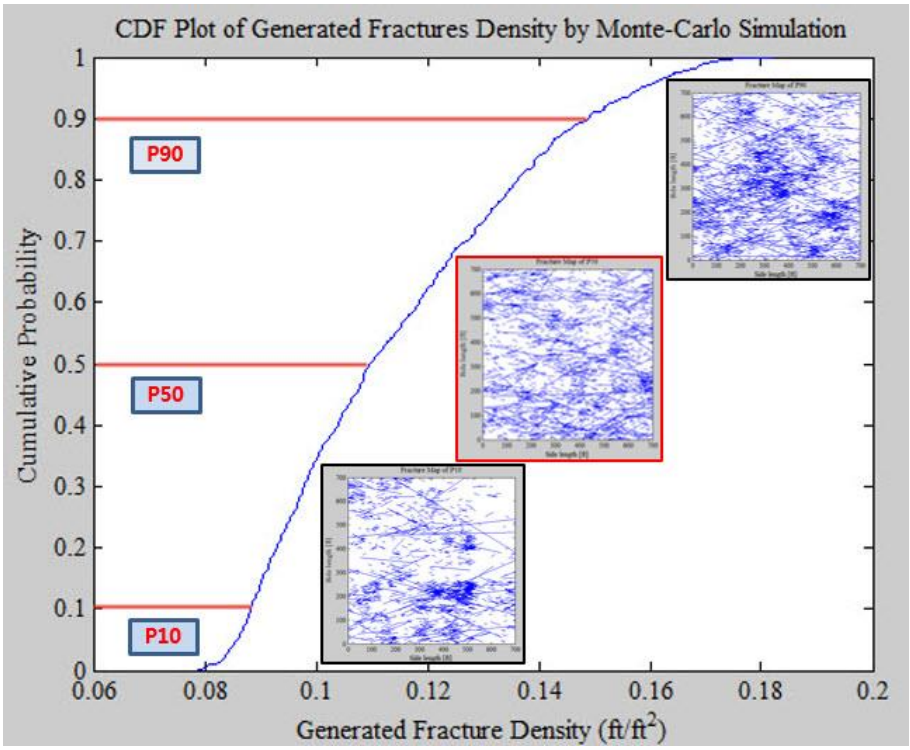

Figure 7.15 CDF plot of the fracture density generated by the Monte Carlo simulation.

After a 1,000-time Monte Carlo simulation, the CDF plot of the fracture networks was calculated, and P10, P50, and P90 fracture network distribution maps were estimated, as shown in Figure 7.15. The P50 fracture network was selected for the simulation and the REV was calculated to determine the domain size. As shown in Figure 7.16, a $500 \times 500\ ft$ domain had a REV and was selected for the simulation. Figure 7.17 shows the selected fracture network from the REV calculation. I used 55×55 grids for this 5-spot pattern simulation. Four water injectors were located at the four corners and the producer was located at the center of the domain, as shown in Figure 7.18. Figure 7.19 shows the calculated log-scaled x- and y-directional equivalent permeability distributions; it also reflects the heterogeneous characteristics of the fracture geometry and fracture clustering.

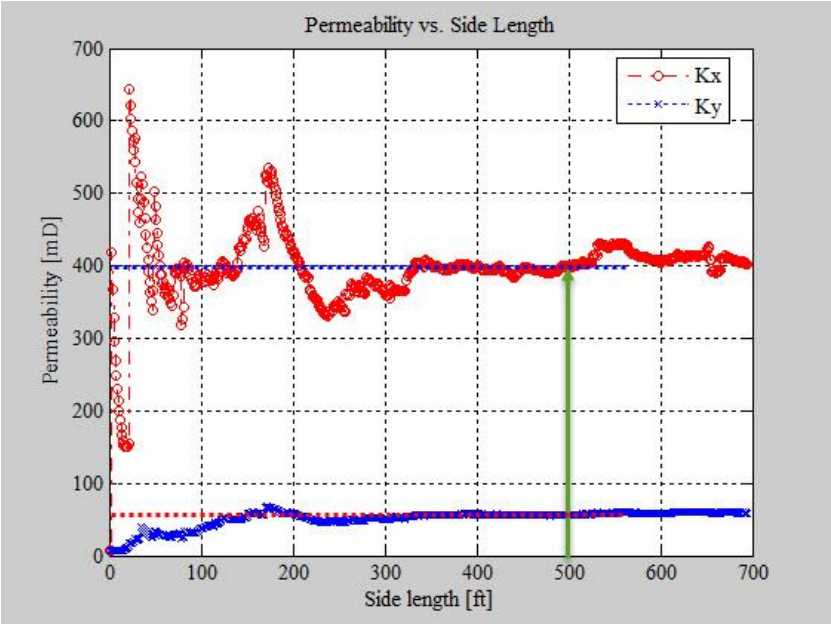

Figure 7.16 The x- and y-directional equivalent permeability calculations with a different screen window size.

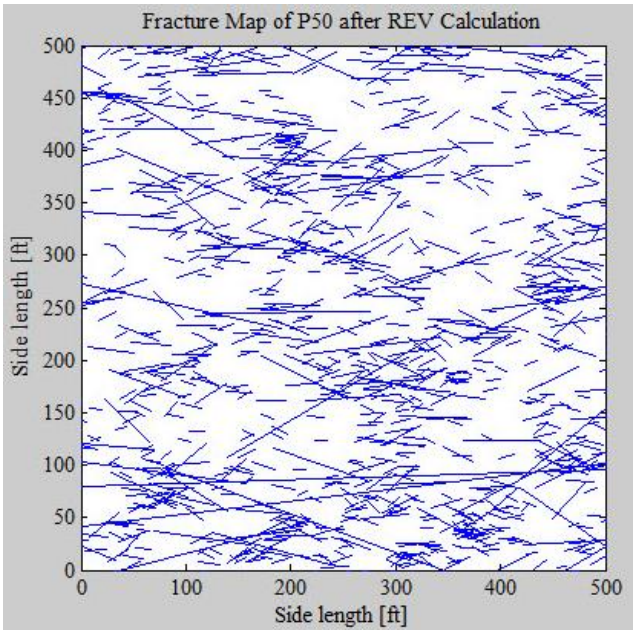

Figure 7.17 P50 fracture map after the REV calculation.

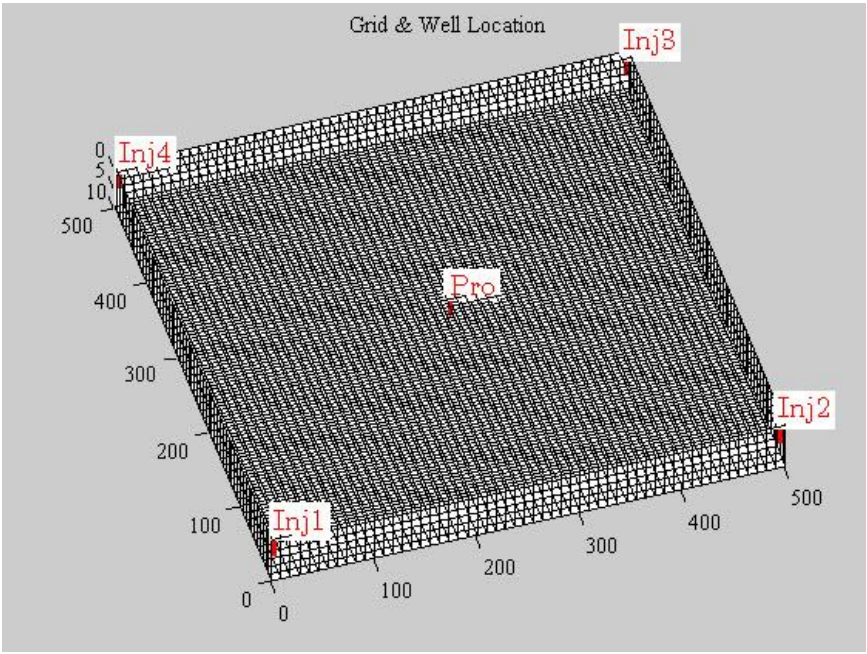

Figure 7.18 Grid and well locations for the 5-spot pattern simulation.

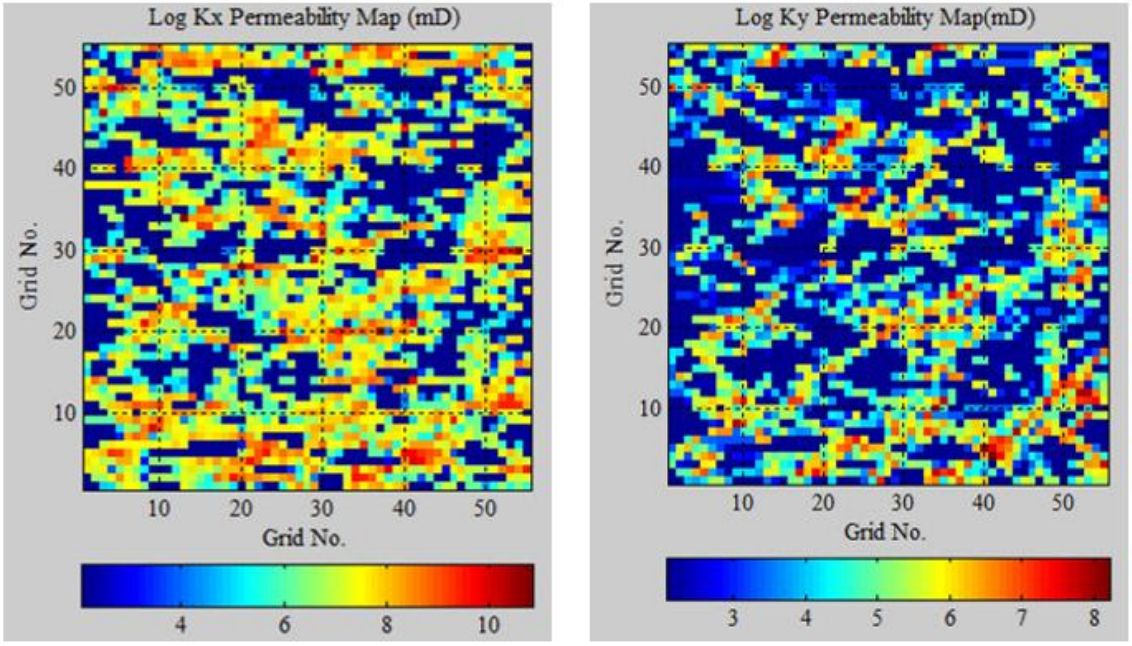

Figure 7.19 Log-scaled x- and y-directional equivalent permeability calculation results using FDFN information.

Table 7.3 Input data for the 5-spot pattern coupling simulation with more x-directional fracture sets

Domain size	500×500	*ft*
Grid block numbers (x, y, z)	55×55×1	
Production time	200	*days*
Injector 1 coordinates (x, y)	(1, 1)	
Injector 2 coordinates (x, y)	(55, 1)	
Injector 3 coordinates (x, y)	(55, 55)	
Injector 4 coordinates (x, y)	(1, 55)	
Production well coordinates (x, y)	(28, 28)	
Well radius	0.35	*ft*
Matrix porosity	0.18	
Water viscosity	1	*cp*
Oil viscosity	2	*cp*
Fluid compressibility	4.0E-06	$1/psi$
Rock compressibility	1.0E-07	$1/psi$
Matrix permeability	8	mD
Oil density	45	lb/ft^3

Table 7.3 Continued

Water density	62.4	lb/ft^3
Initial water saturation	0.2	
Initial pressure	700	psi
Water injection rate	200	bbl/day
Producer bottom hole pressure (BHP)	600	psi
Young's modulus	$1.5E4$	psi
Joint roughness coefficient (JRC)	5	
Joint compressive strength (JCS)	5, 10, 20, 30, 40	Mpa
X-directional confining pressure	7000	Kpa
Y-directional confining pressure	4000	Kpa
Four node rectangular element for solid (Q4)		
Four node rectangular element for pore pressure (Q4)		

The input data used for the 5-spot pattern flow simulation are given in Table 7.3.

In both the iterative and SIPC coupling simulations, biaxial confining pressures were imposed and four node rectangular elements were employed for the displacement and pore pressure calculations. A larger x-directional confining pressure was applied than y-directional confining pressure, considering the parallel with the x-directional fracture orientation.

In the SIPC coupling simulation, the fractures were divided into fracture segments corresponding to the 55×55 sub-domains; then, the middle points of the fracture segments in each sub-domain were calculated. The x- and y-directional effective stresses of each fracture segment were interpolated from the x- and y-directional effective stresses of the grid nodal points via a kriging method. Figure 7.20 shows an example of the calculated x-directional effective nodal stress change, $\Delta\sigma'_x$, using grid nodal points. Figure 7.21 shows the interpolated x-directional effective stress by the kriging method and considered middle points of the fracture segments.

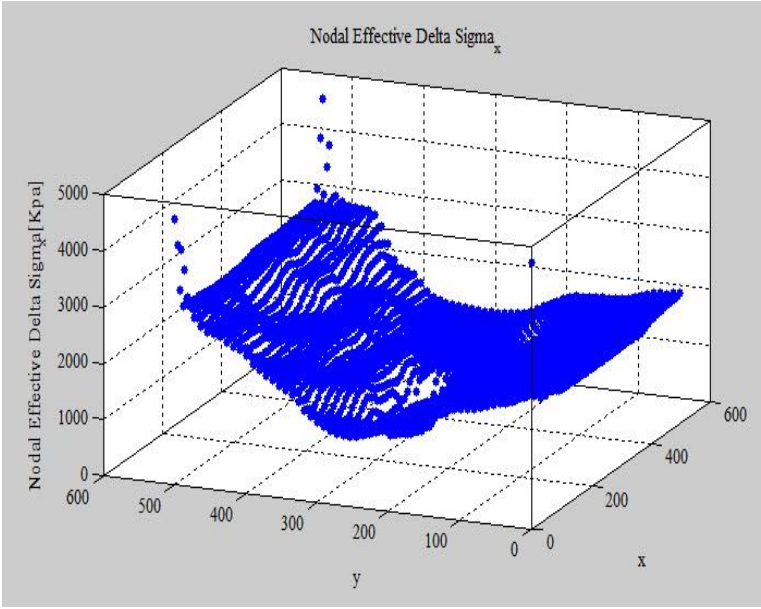

a) Calculated nodal $\Delta\sigma'_x$ by SIPC coupling simulation

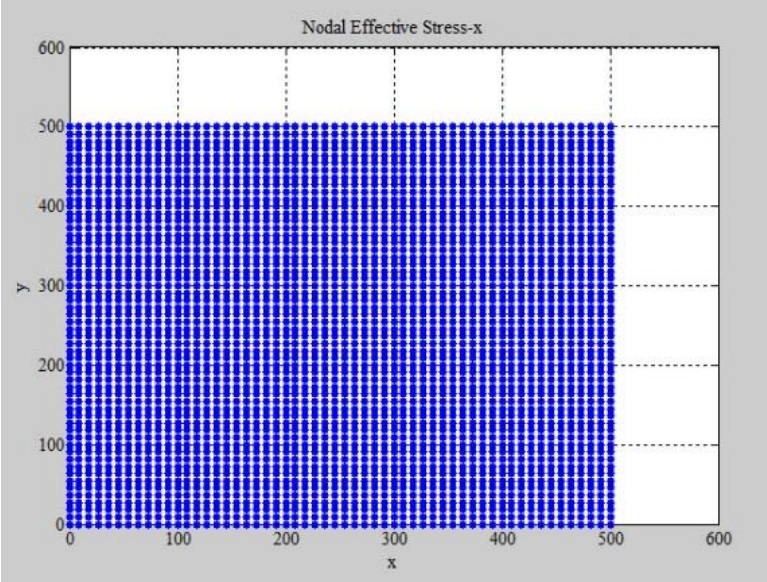

b) Nodal points

Figure 7.20 Calculated nodal $\Delta\sigma'_x$ and simulated nodal points.

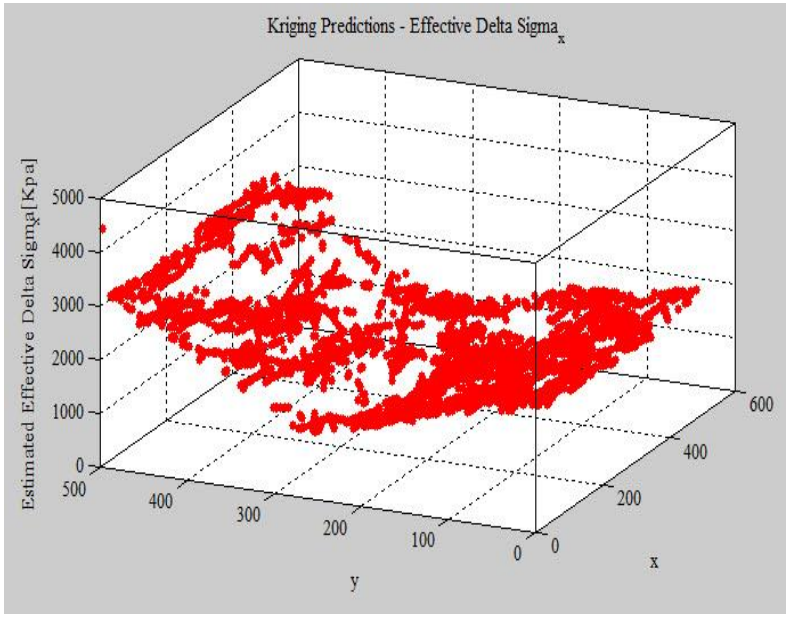

a) Interpolated $\Delta\sigma'_x$ of the middle of the fracture segments by the kriging method

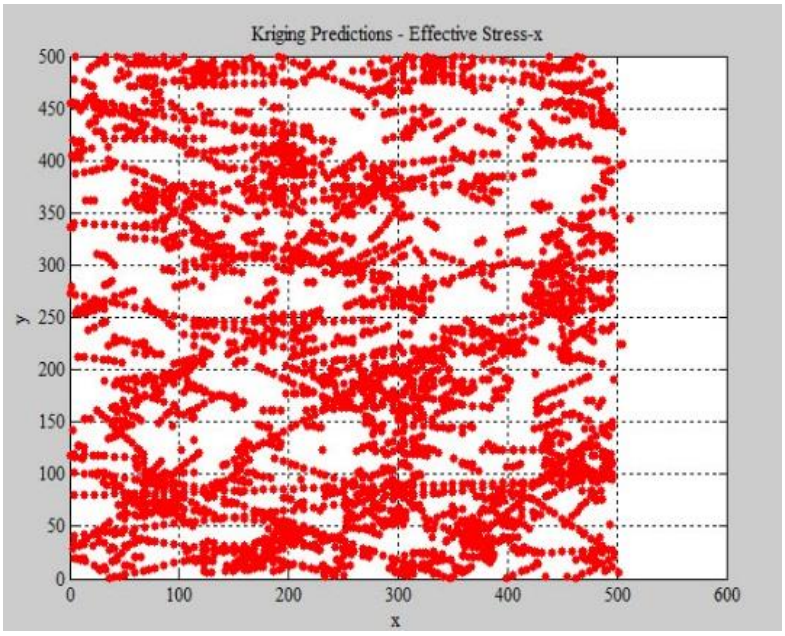

b) Middle points of the fracture segments

Figure 7.21 Interpolated $\Delta\sigma'_x$ of the fracture segments and their middle points.

Then, the effective normal stress in the middle of each fracture segment was calculated using a stress transformation equation, Eq. 6.34. After the kriging calculation of the effective normal stress changes in the fractures, a normal stiffness, k_n, was calculated to determine the stress-induced aperture deformation.

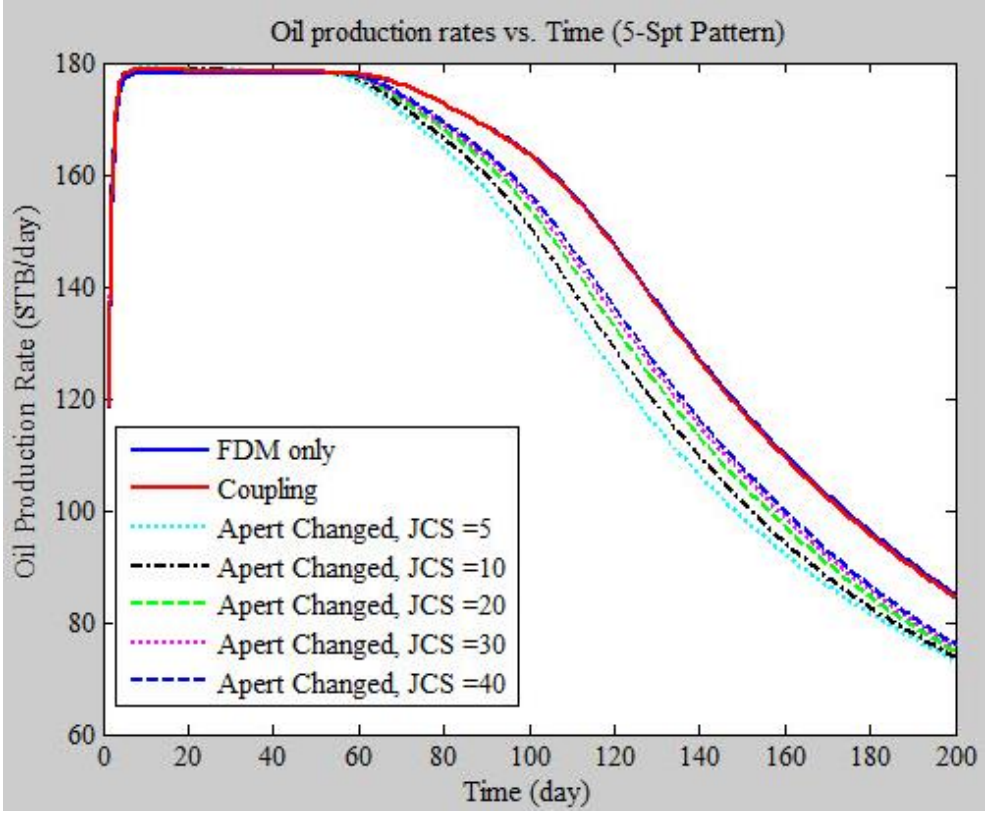

Figure 7.22 Oil production rate by FDM, iterative coupling and SIPC coupling simulations.

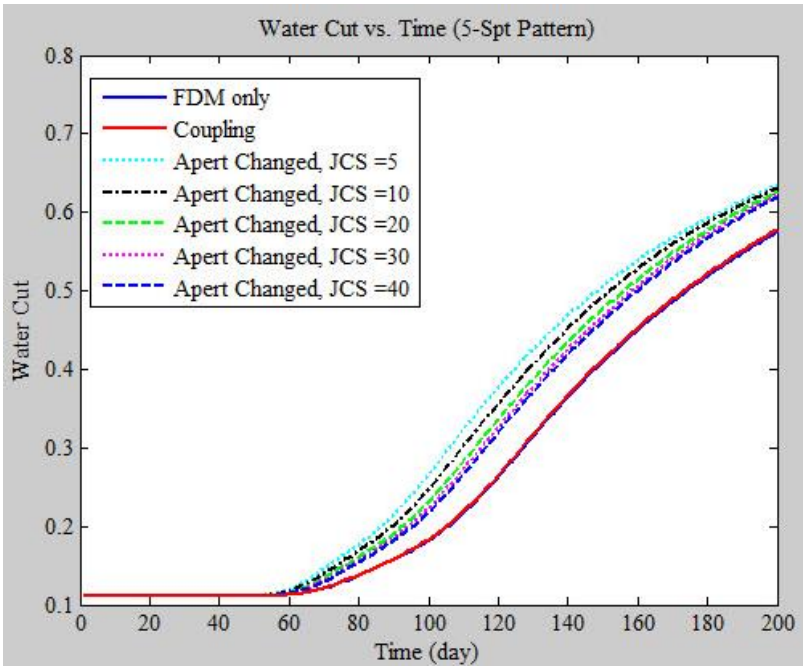

Figure 7.23 Water cut by FDM, iterative coupling and SIPC coupling simulations.

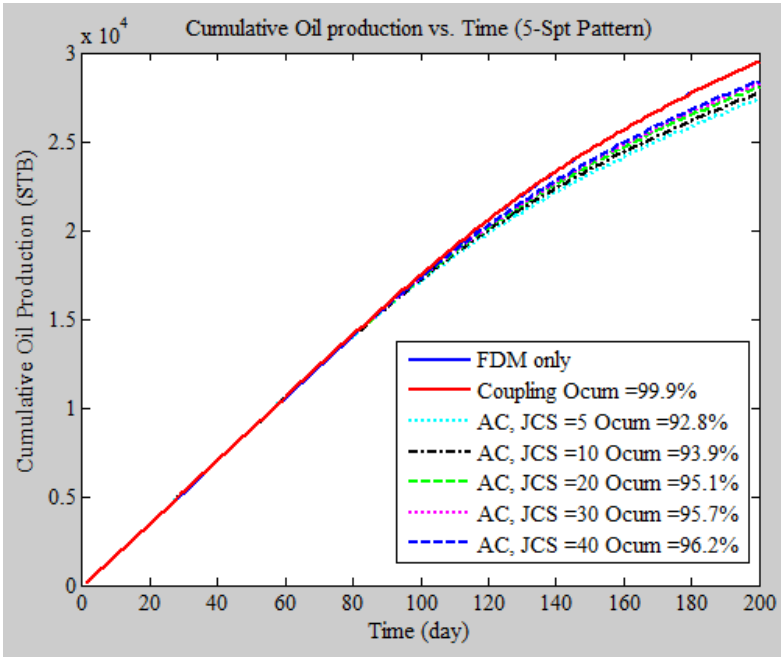

Figure 7.24 Cumulative oil production by FDM, iterative coupling and SIPC coupling simulations.

Figures 7.22 to 7.24 show the simulation results of oil production rate, water cut, and cumulative oil production by the FDM, iterative coupling, and SIPC coupling simulations. As shown in simulation results, the FDM and iterative coupling simulations showed similar production performances, but the SIPC coupling simulation exhibited different behavior, depending on the JCS value. Even though the FDM and iterative coupling simulations displayed similar behaviors with regards to oil production rate and water saturation, the calculated pore pressure distribution results were different. The percentage in Figure 7.24 represents the rate of cumulative oil production by coupling simulation compared with FDM simulation results under the same condition. After 200 days of simulation, SIPC coupling simulation showed the difference rate range from 92.7 % to 96.2 %. The cumulative oil production rate by the SIPC coupling simulation decreased as production time passed in this case study.

Figures 7.25 to 7.27 show the calculated pore pressure distributions, and Figures 7.28 to 7.30 show the calculated water saturation maps by each simulation method. Reservoir pore pressure increased due to the water injection, and the overall pore pressure was larger than the initial pore pressure value given in Table 7.3. This increase in pore pressure resulted in extensional volumetric strain changes and an increases in porosity. This change affected the equivalent permeability calculation.

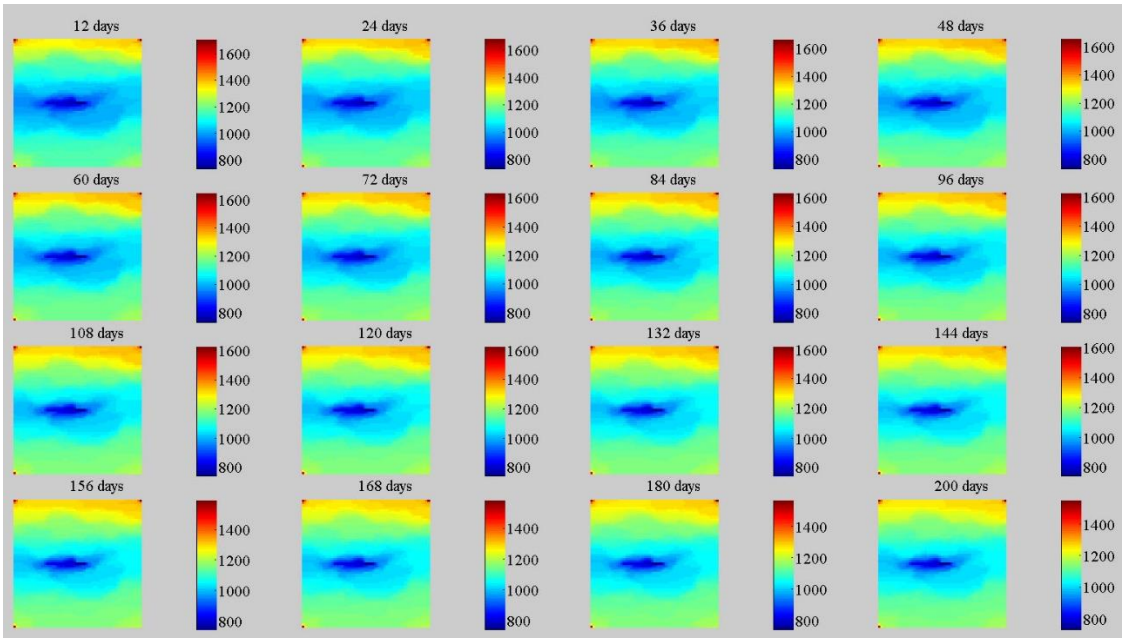

Figure 7.25 Pore pressure distribution by FDM simulation.

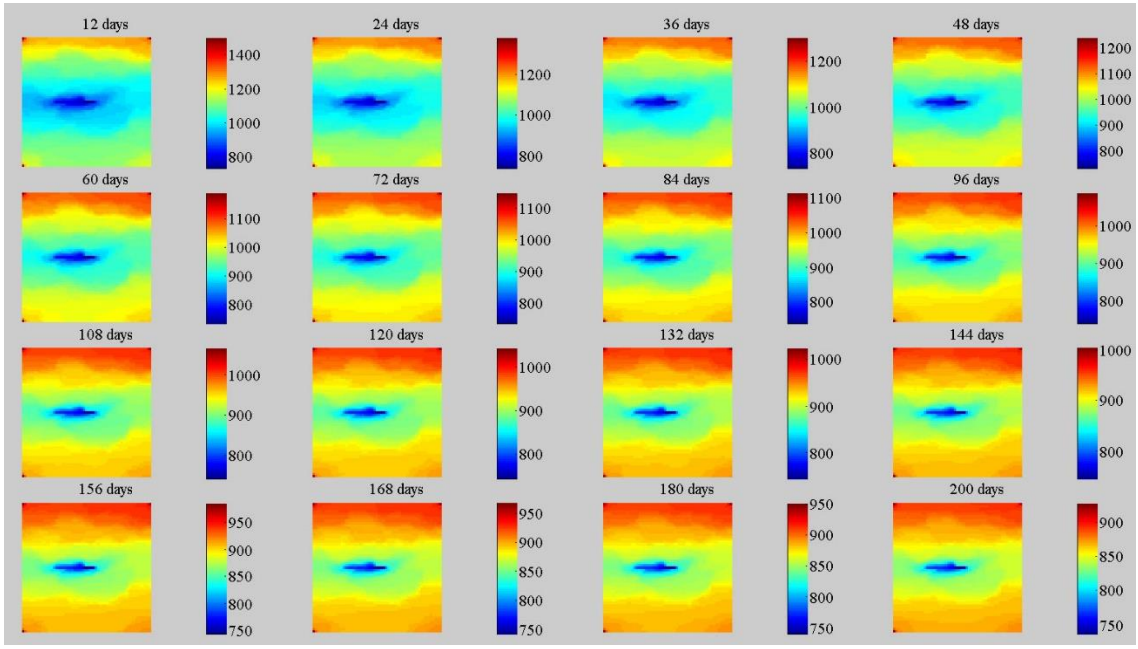

Figure 7.26 Pore pressure distribution by iterative coupling simulation.

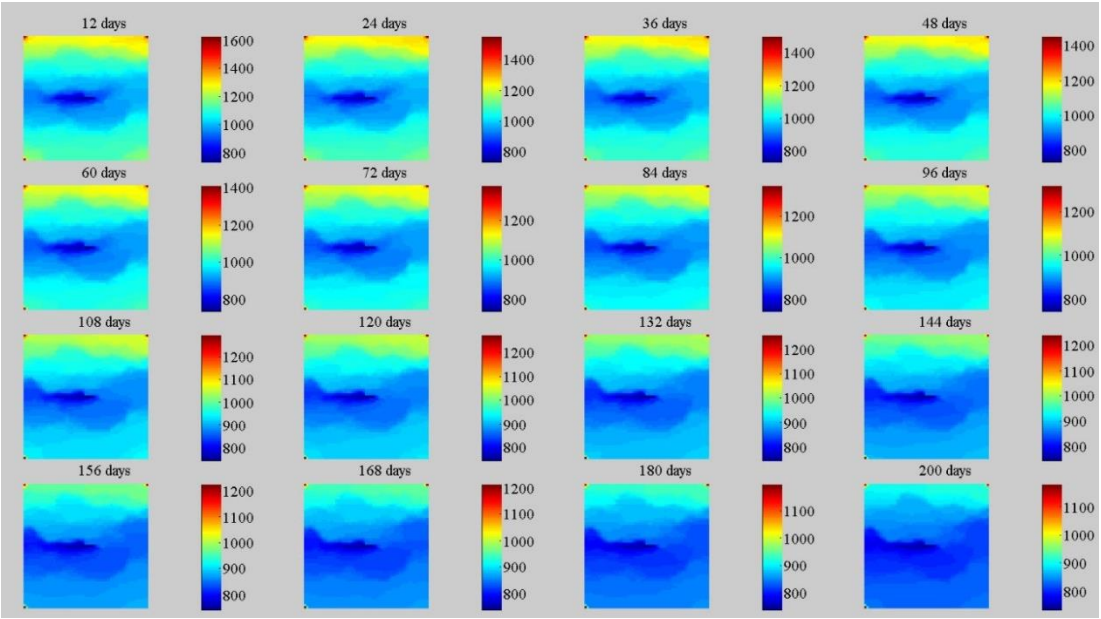

Figure 7.27 Pore pressure distribution by SIPC coupling simulation.

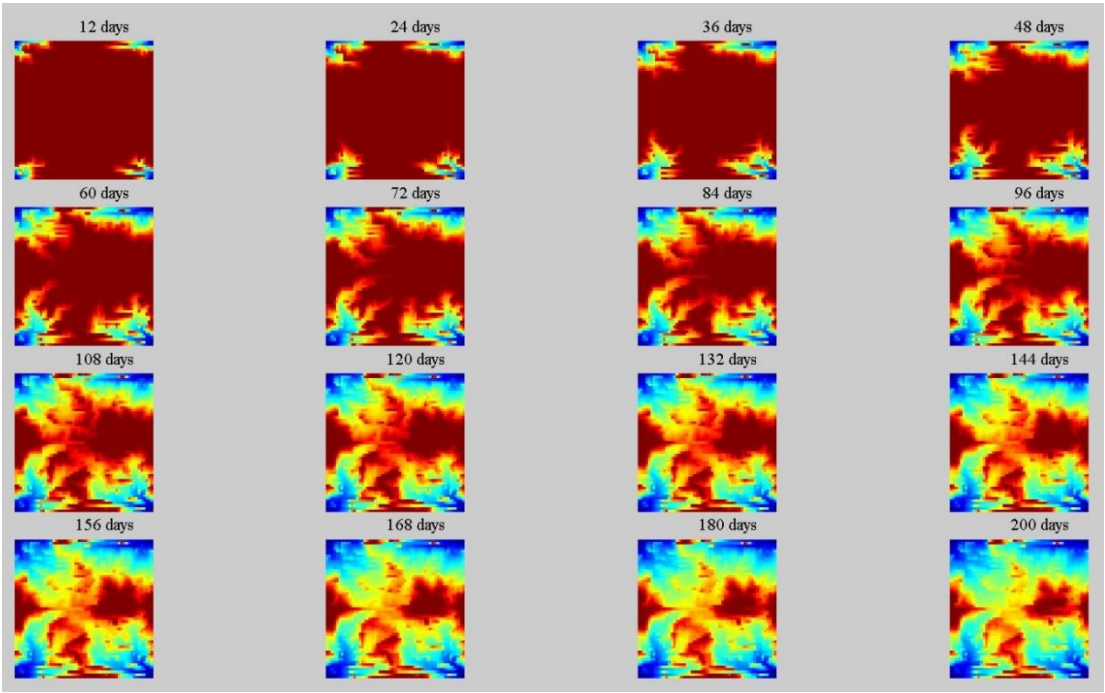

Figure 7.28 Water saturation by FDM simulation.

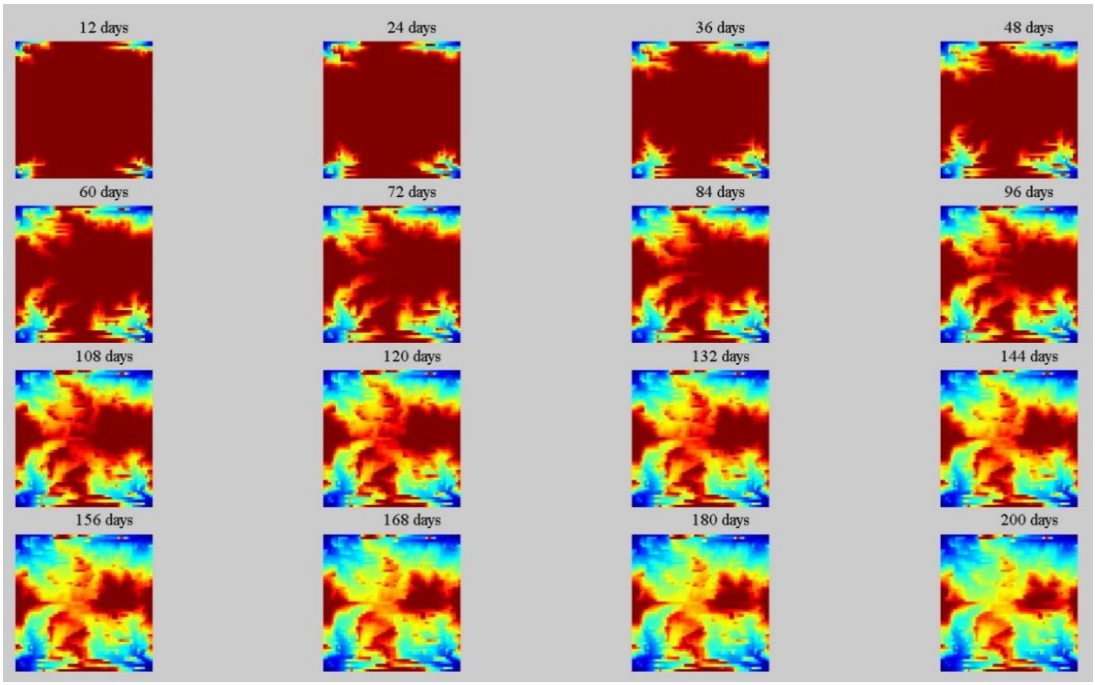

Figure 7.29 Water saturation by iterative coupling simulation.

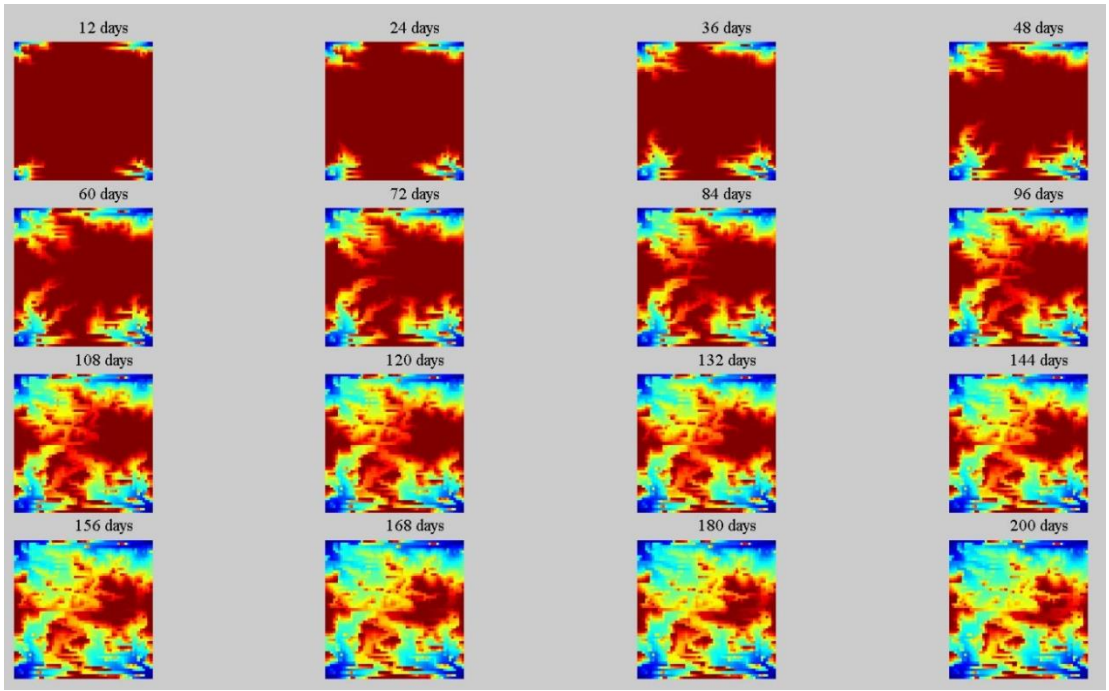

Figure 7.30 Water saturation by SIPC coupling simulation.

During the FDM simulation, the x- and y-directional equivalent permeabilities were constant. However, during the coupling simulations, the x- and y-directional equivalent permeabilities were updated at every time step. Figures 7.31 and 7.32 show the updated x- and y-directional permeabilities after 200 days of water flooding. Table 7.4 shows the Changing Rates (CRs) of the minimum and maximum values of the x- and y-directional permeabilities, as compared with the initial permeability values. As shown in the simulation results, both the x- and y-directional permeabilities increased after the coupling simulation. With regards to iterative coupling, it was observed that the equivalent permeability increased, not only in the fractured zone but also in the non-fractured zone. In addition, isotopic and proportional changing behaviors were observed in both directions of permeability. This was why the iterative coupling simulation estimated equivalent permeability using the empirical relationships controlled by the volumetric strain, saturation, and/or porosity changes. In this case study, the iterative coupling simulation showed the overall increase in permeability in the entire reservoir. However, these empirical equations had certain limitations preventing them from adequately describing the anisotropic characteristics of directional permeability change. Also, even though the fluid and geomechanics properties were considered in the coupling simulation, the EC scheme was problematic for use in describing the fracture flow effect on the simulation, due to certain inherent characteristics of EC scheme.

Therefore, I proposed a combined EC and DFN scheme in order to better describe the anisotropic behavior and more accurately reflect the geomechanics characteristics in the coupling simulation. In the SIPC coupling simulation, the FDFN

geometry data were imported to the SIPC simulator to calculate the coordinate data of the fracture segments and distributed aperture data of the corresponding sub-domain. After the stress-induced aperture deformation calculation, the directional equivalent permeabilities were estimated by a modified Oda's method.

In the SIPC simulation, the equivalent permeability of the non-fractured zone didn't increase because the permeability was directly calculated by a modified Oda's algorithm using the stress-induced aperture deformation data. Therefore, the minimum values of the x- and y-directional equivalent permeabilities of the iterative coupling were larger than those of the SIPC simulation, whereas the maximum values of the iterative coupling were smaller than those of the SIPC simulation, as shown in the results. The SIPC simulation described a larger equivalent permeability change at the fracture zones and no permeability change at the non-fractured zones. If the matrix flow is also an important parameter, the matrix permeability increase should be considered in the SIPC coupling simulation.

Table 7.4 The changing rates of the minimum and maximum values of the x- and y-directional permeabilities by 5-spot pattern simulation

	X-directional permeability, k_x		Y-directional permeability, k_y	
	CR of the minimum k_x	CR of the maximum k_x	CR of the minimum k_y	CR of the maximum k_y
Iterative Coupling (IC)	243.9 %	463.5 %	223.1 %	478.8 %
SIPC coupling	100 %	699.5 %	100 %	655.3 %
Relative CR (SIPC / IC)	41.0 %	150.9 %	44.8 %	136.9 %

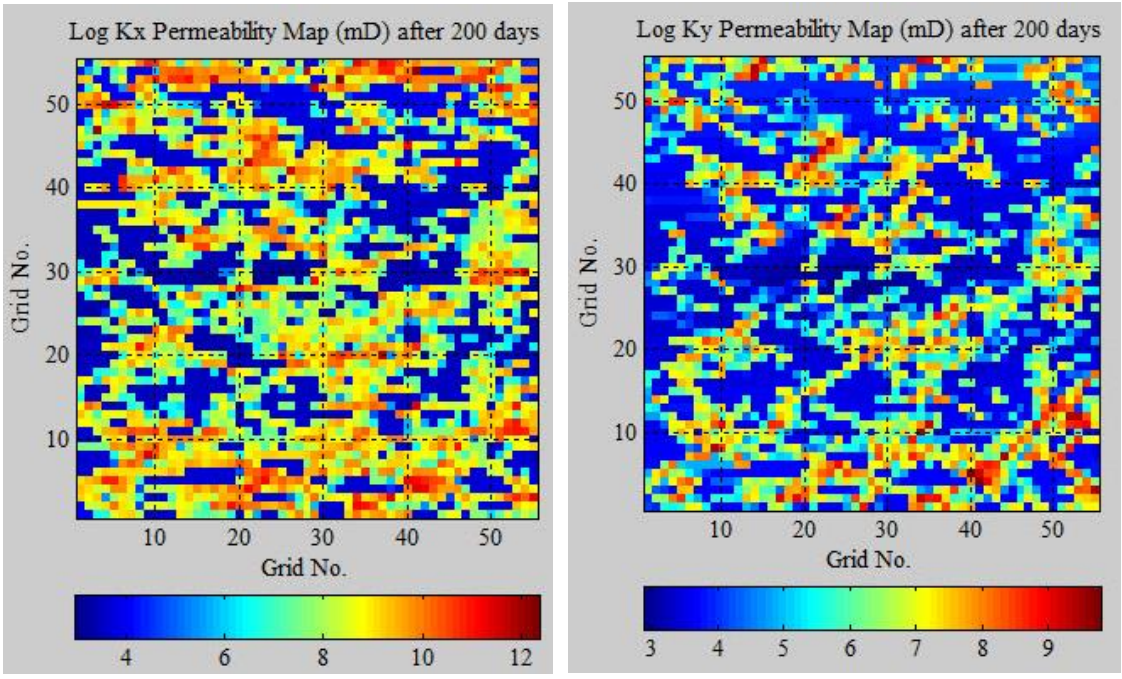

Figure 7.31 The x- and y-directional permeabilities by iterative coupling after 200 days.

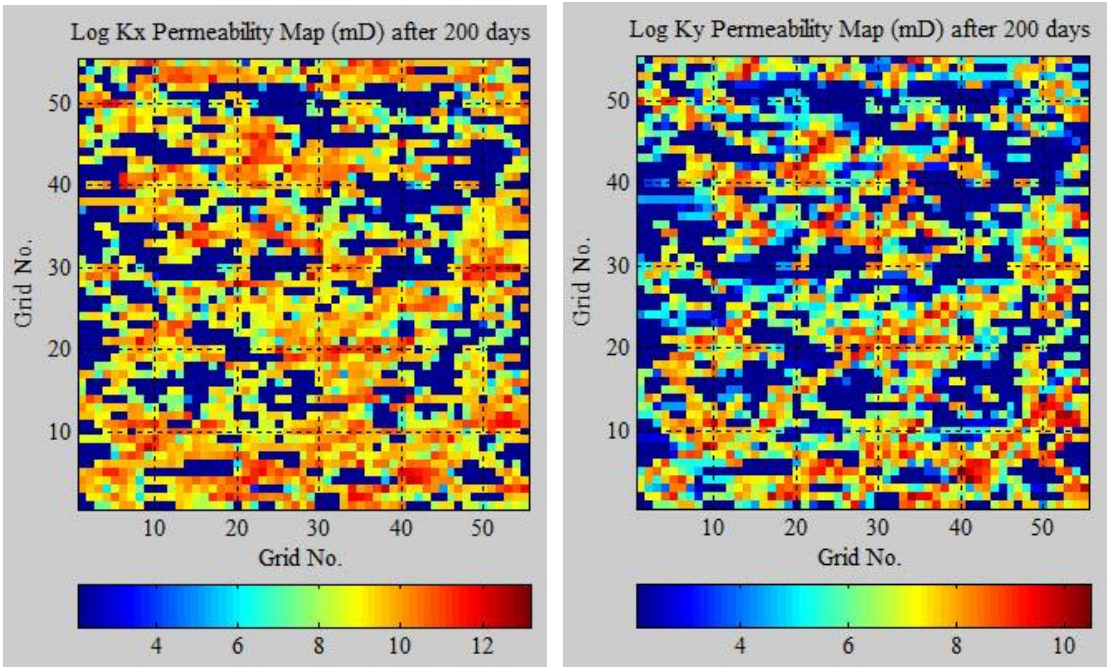

Figure 7.32 The x- and y-directional permeabilities by SIPC coupling after 200 days.

In the SIPC coupling simulation, it was assumed that the stress of the middle point of the fracture segment represented the stress condition along the plane of the fracture segment. Also, the JRC and JCS of the fracture were assumed to be uniform for all of the fractures. Then, the deformation of each aperture segment was calculated by Eq. 6.42, considering the initial aperture value. Figure 7.33 shows the updated aperture distributions after the SIPC coupling simulation. As shown in this Figure, the fracture network showed a larger aperture deformation; it had a lower JCS value, and the changed aperture distribution also followed a normal distribution. The overall increase of reservoir pore pressure resulted in the aperture opening of all of the fractures. Table 7.5 shows the changing rates of the mean value of the updated aperture distribution, as compared with the mean value of the initial aperture distribution.

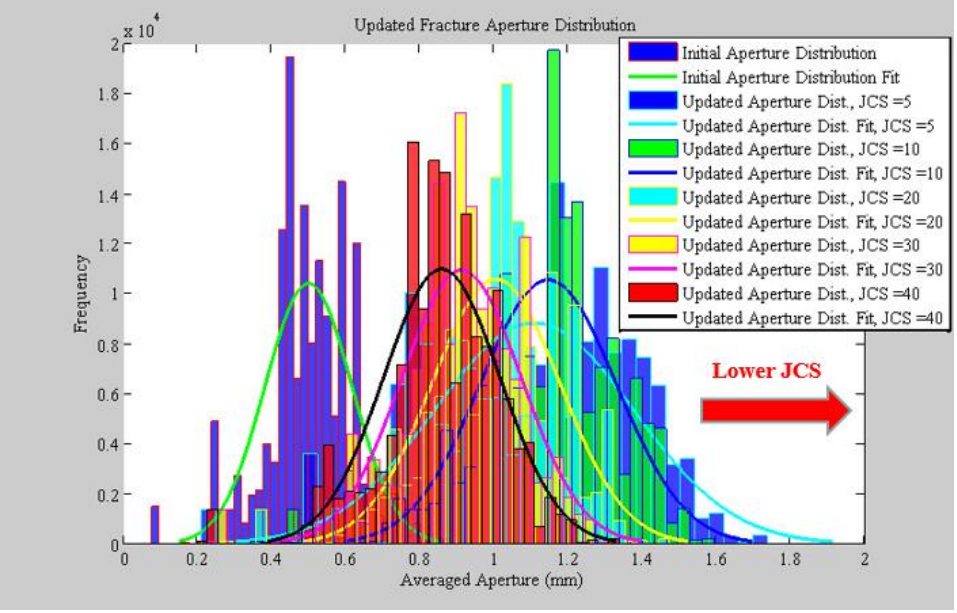

Figure 7.33 Updated aperture distributions after the SIPC coupling simulation.

Table 7.5 The changing rates of the mean value of the updated aperture distribution

JCS	5	10	20	30	40
Changing rate of the mean value	249 %	229.8 %	201.5 %	182.9 %	179.2 %

7.4 Case IV – 2D Horizontal Well Flow Simulation with More X-Directional Fracture Sets

In this case study, a case with a two-dimensional horizontal production well and two vertical water injection wells was simulated. More x-directional fractures were also considered. In order to generate the FDFN, I used almost the same input data as was used in the previous case study. The only difference was that the domain size was $100\ ft$ and the minimum fracture length was one one-hundredth of the domain size length, $0.01 \times L$. The input data are given in Table 7.6. The aperture distribution also followed the normal distribution, with a 0.5 mm mean aperture and a 0.25 mm standard deviation.

Table 7.6 Input data for the FDFN generation of a horizontal well simulation

Domain size	100×100	*ft*
Minimum fracture length	1	*ft*
Fractal center dimension, FD_c	1.9	
Fractal length dimension, FD_l	1.5	
Fracture density term, α	0.5	
Aperture (Normal distribution)		
Mean	0.5	*mm*
Standard deviation	0.25	*mm*
Fracture set 1		
Fracture orientation	10°	
Probability	50	%
Fracture set 2		
Fracture orientation	170°	
Probability	50	%

Figure 7.34 shows the generated aperture distribution and Figure 7.35 includes a rose diagram of the generated fractures. As mentioned above, because the FDFN generates codes using fractal and statistical methods, the generated fracture networks were different from those of the previous case study, even though nearly the same input data were used. Figure 7.36 includes a sampled fractures array with aperture segment numbers.

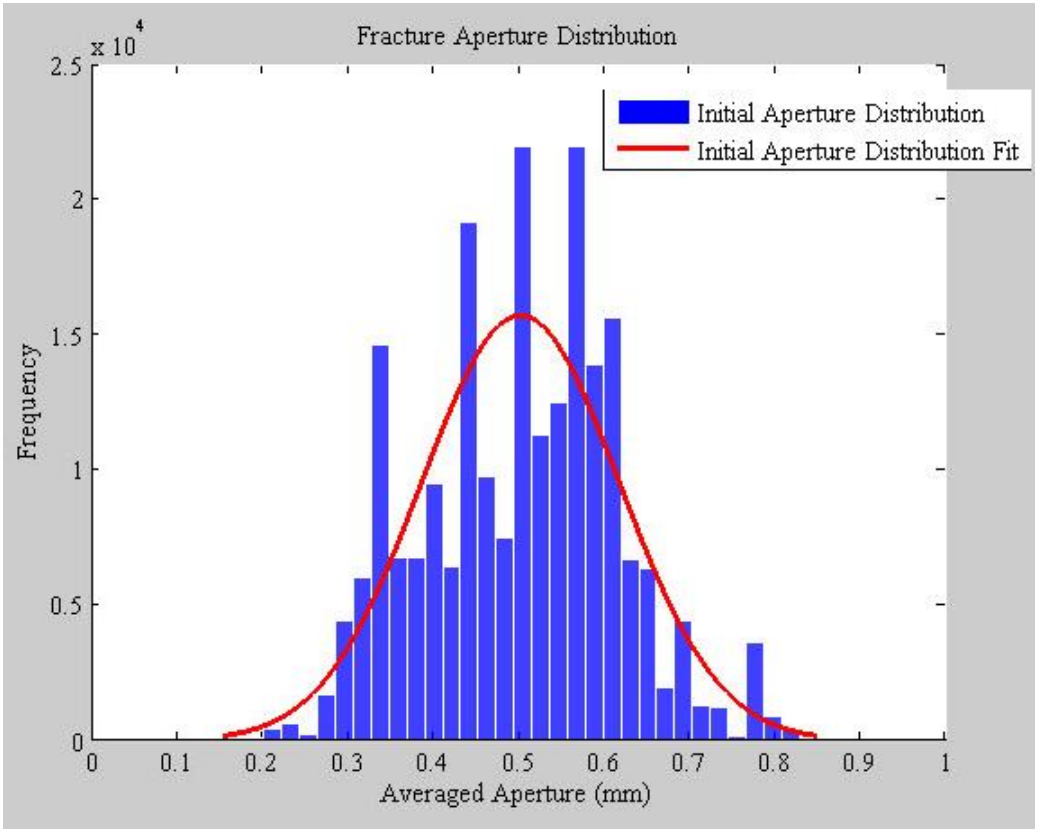

Figure 7.34 Initial aperture distribution.

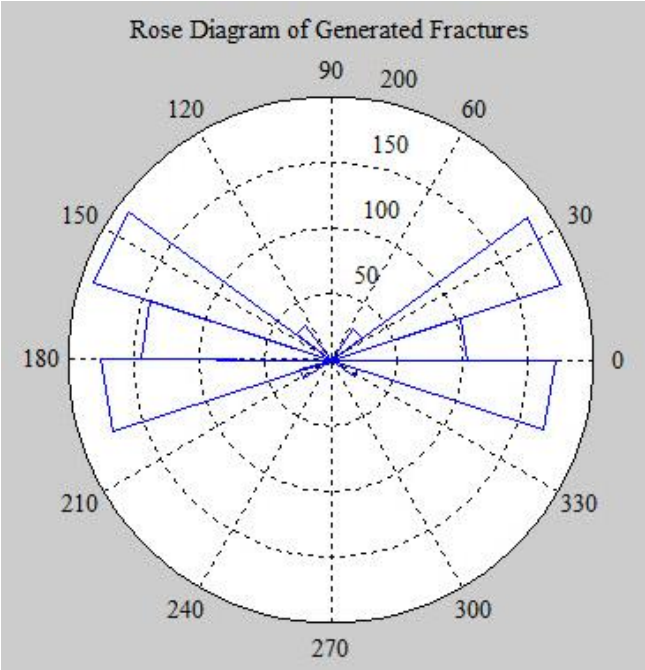

Figure 7.35 Rose diagram of generated fractures.

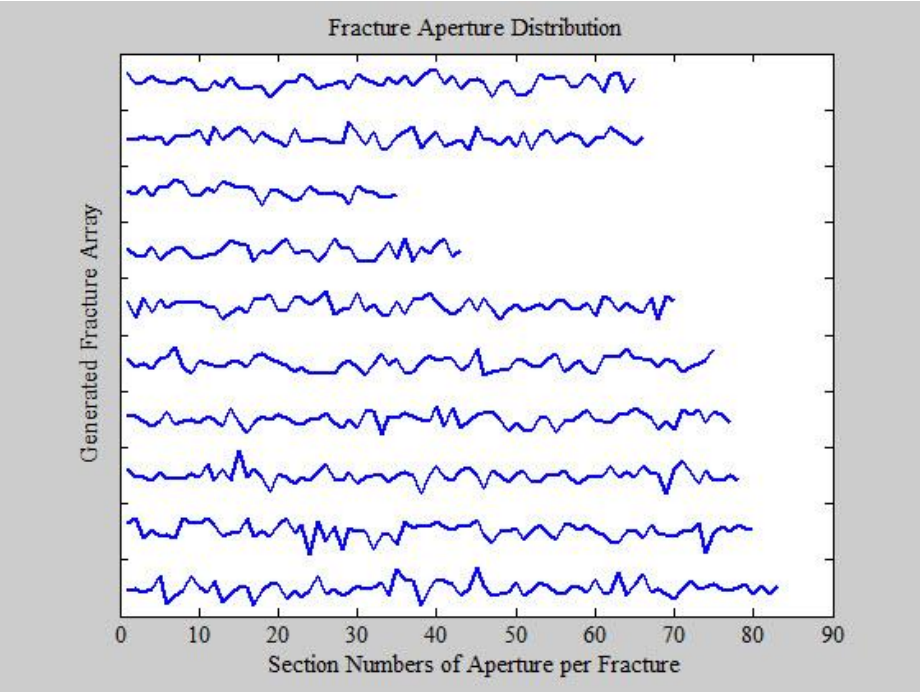

Figure 7.36 Array of ten sampled fractures with aperture distributions.

After a 1,000-time Monte Carlo simulation, the CDF plot of the fracture networks was calculated, and the P50 fracture networks map was estimated. Figure 7.37 shows the calculated CDF plot and estimated P10, P50, and P90 fracture maps.

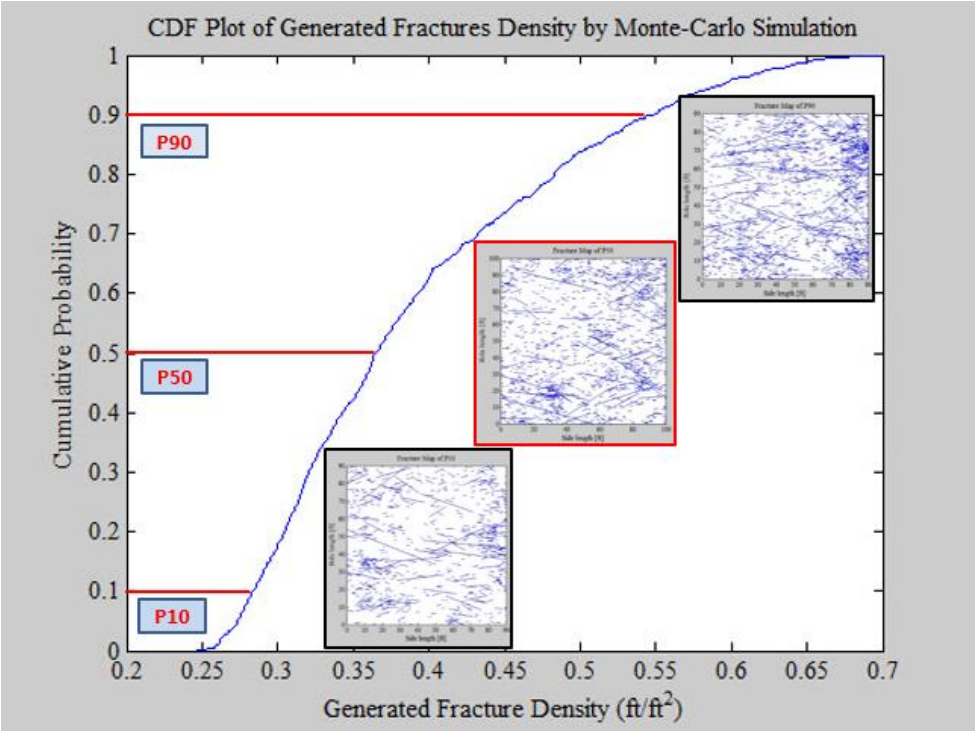

Figure 7.37 CDF plot of the generated fracture density by Monte Carlo simulation.

From the REV calculation, a $90\ ft$ domain size was selected, as shown in Figure 7.38, and Figure 7.39 shows the selected P50 fracture network map.

As opposed to the previous 5-pattern well case study, this case study was simulated with finer grids: 80×80 for the smaller area. A smaller Young's modulus, water injection rate, and matrix permeability were also considered in order to investigate

the clearer stress-induced aperture change effect on the equivalent permeability estimation and production performance. Two water injectors were located at the top-right and bottom-right corners, and the horizontal production well was located at the left side of the domain, as shown in Figure 7.40. Figure 7.41 shows the calculated log-scaled x- and y-directional equivalent permeability distributions.

The input data are given in Table 7.7.

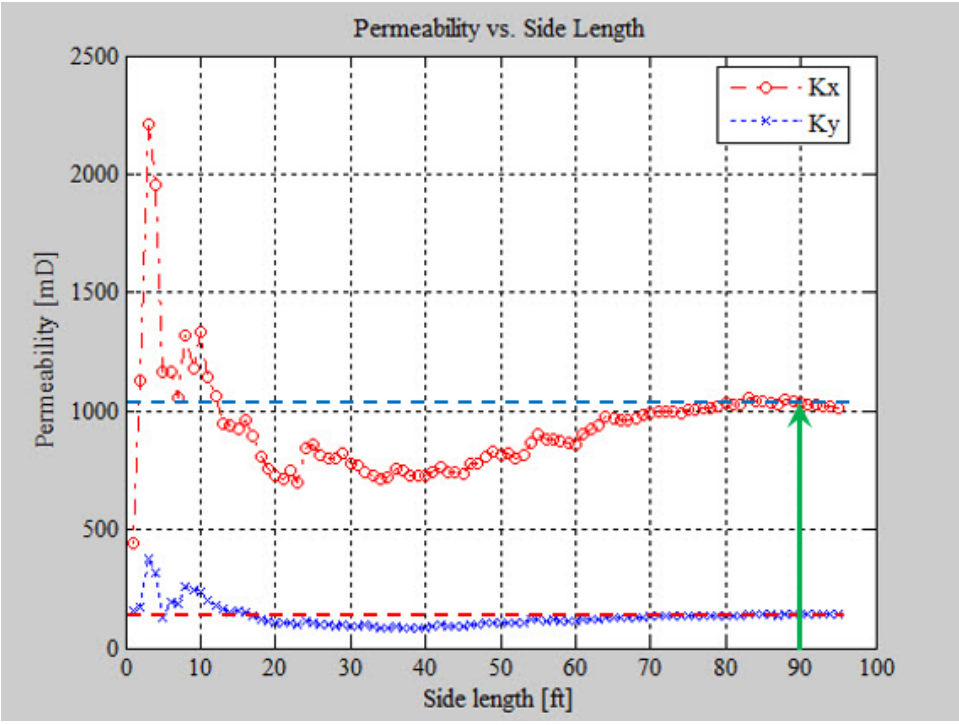

Figure 7.38 The x- and y-directional equivalent permeabilities with a different screen window size for the REV calculation.

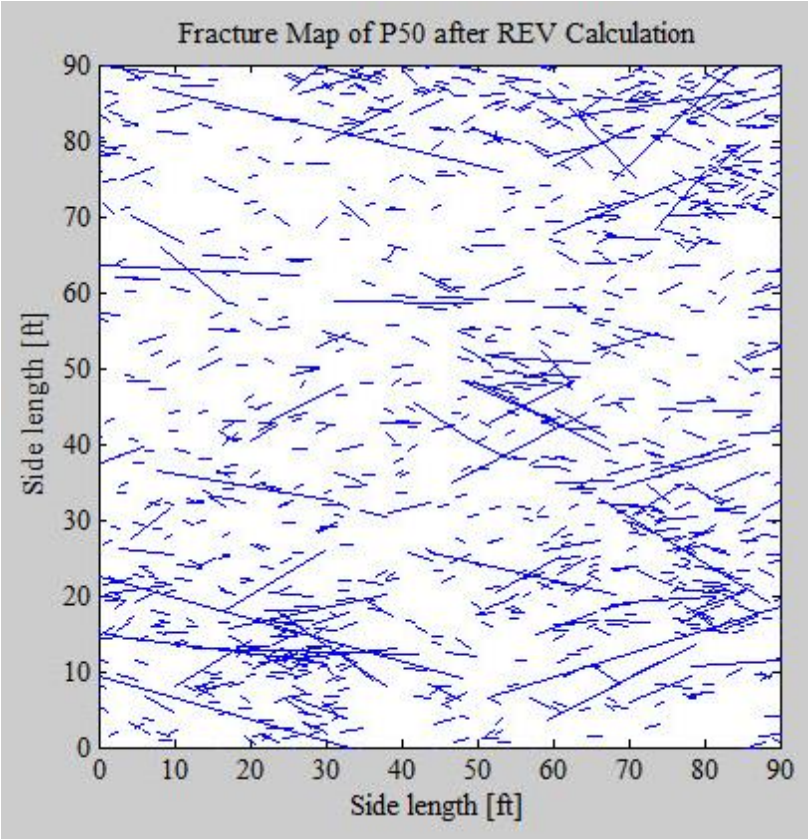

Figure 7.39 P50 fracture map after the REV calculation.

Table 7.7 Input data for the horizontal well simulation with more x-directional fracture sets

Domain size	90×90	*ft*
Grid block numbers (x, y, z)	$80 \times 80 \times 1$	
Production time	100	*days*
Injector 1 coordinates (x, y)	(80, 1)	
Injector 2 coordinates (x, y)	(80, 80)	
Production well start coordinates (x, y)	(8, 20)	
Production well end coordinates (x, y)	(8, 60)	
Well radius	0.25	*ft*
Matrix porosity	0.16	
Water viscosity	1	*cp*
Oil viscosity	2	*cp*
Fluid compressibility	4.0E-06	1/ *psi*

Table 7.7 Continued

Rock compressibility	1.0E-07	$1/psi$
Matrix permeability	2	mD
Oil density	45	lb/ft^3
Water density	62.4	lb/ft^3
Initial water saturation	0.2	
Initial pressure	900	psi
Water injection rate	20	bbl/day
Producer bottom hole pressure (BHP)	820	psi
Young's modulus	1.5E3	psi
Joint roughness coefficient (JRC)	5	
Joint compressive strength (JCS)	5, 10, 20, 30, 40	Mpa
X-directional confining pressure	6000	Kpa
Y-directional confining pressure	3000	Kpa
Four node rectangular element for solid (Q4)		
Four node rectangular element for pore pressure (Q4)		

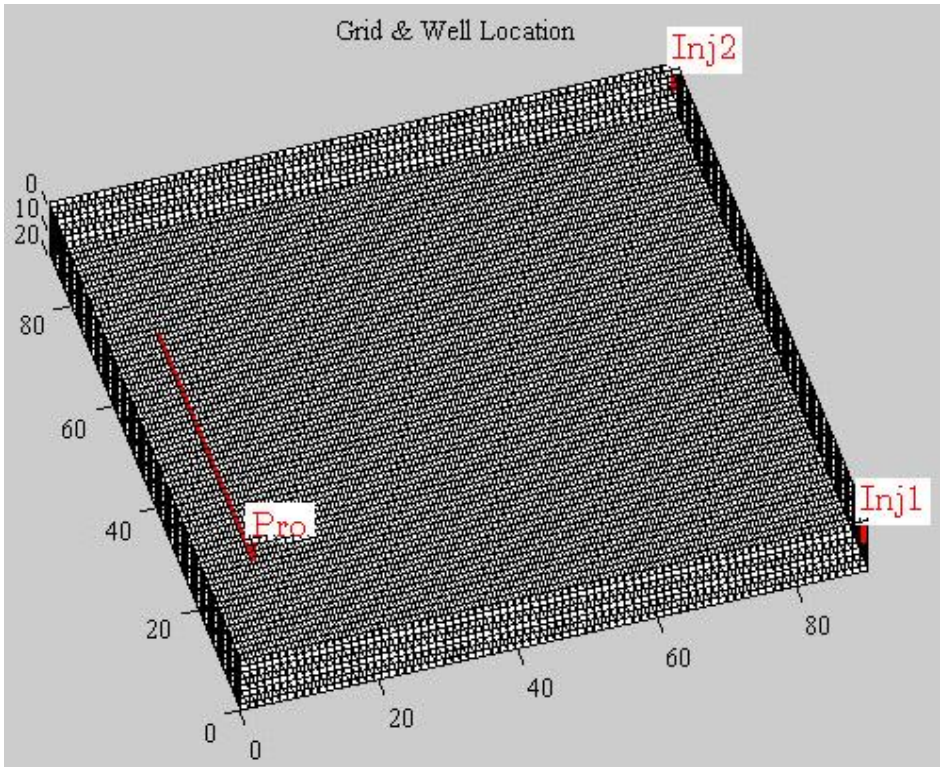

Figure 7.40 Grid and well locations for the horizontal well simulation.

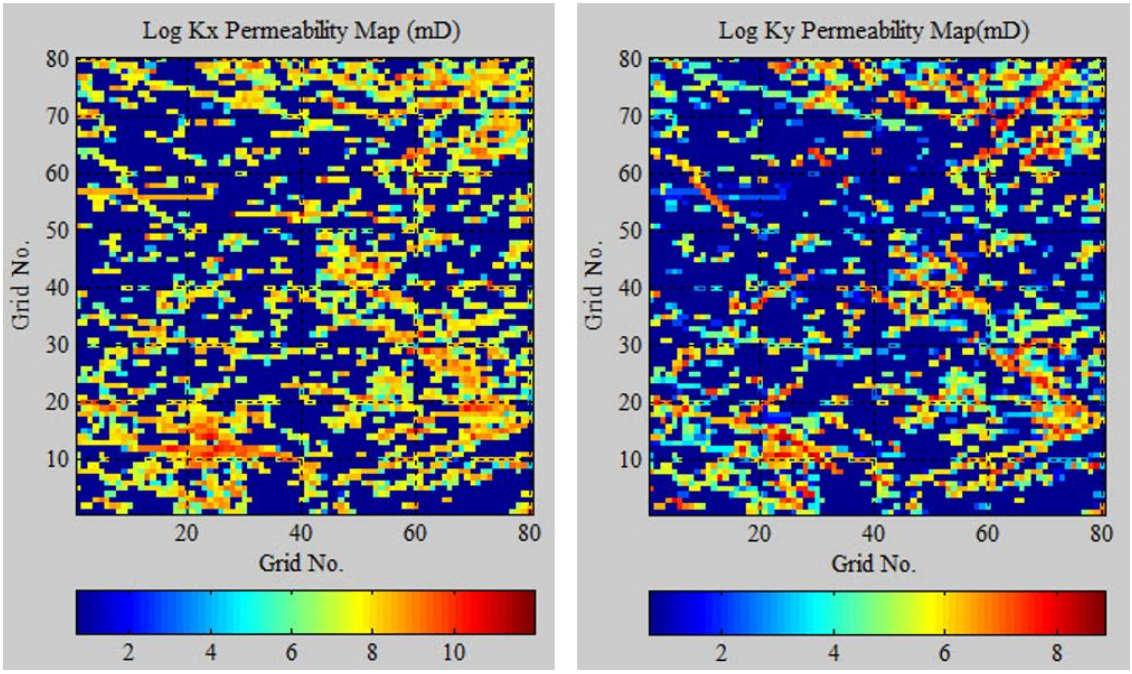

Figure 7.41 Log-scaled x- and y-directional equivalent permeability calculation results using FDFN information.

The calculated pore pressure distributions by each simulation method are shown in Figures 7.42 to 7.44. The black line represents the horizontal well. The simulation results show that the pore pressure of the reservoir was higher than the initial pore pressure, except near the horizontal well area; this resulted in an effective stress reduction and fracture aperture opening. The pore pressure of the near-horizontal production well was lower than the initial pore pressure and resulted in an effective stress increase and fracture aperture closing. The iterative coupling results also showed the quickest and largest pressure dissipation, as was also the case in the previous case study.

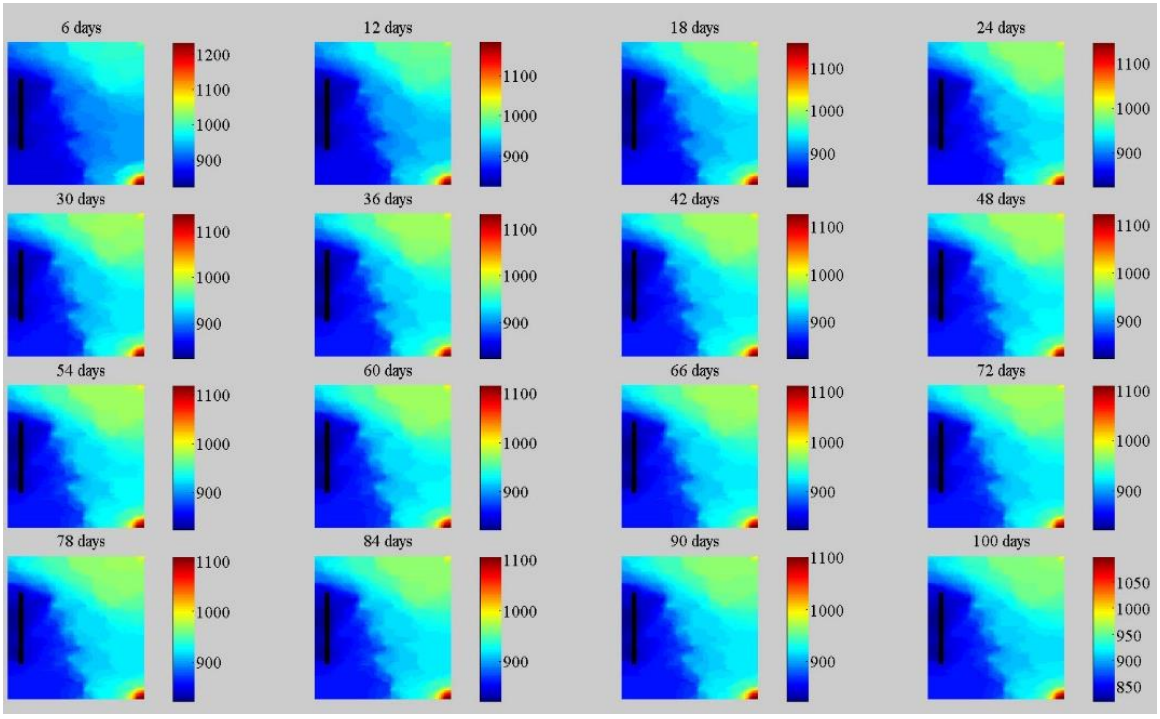

Figure 7.42 Pore pressure distribution by FDM simulation.

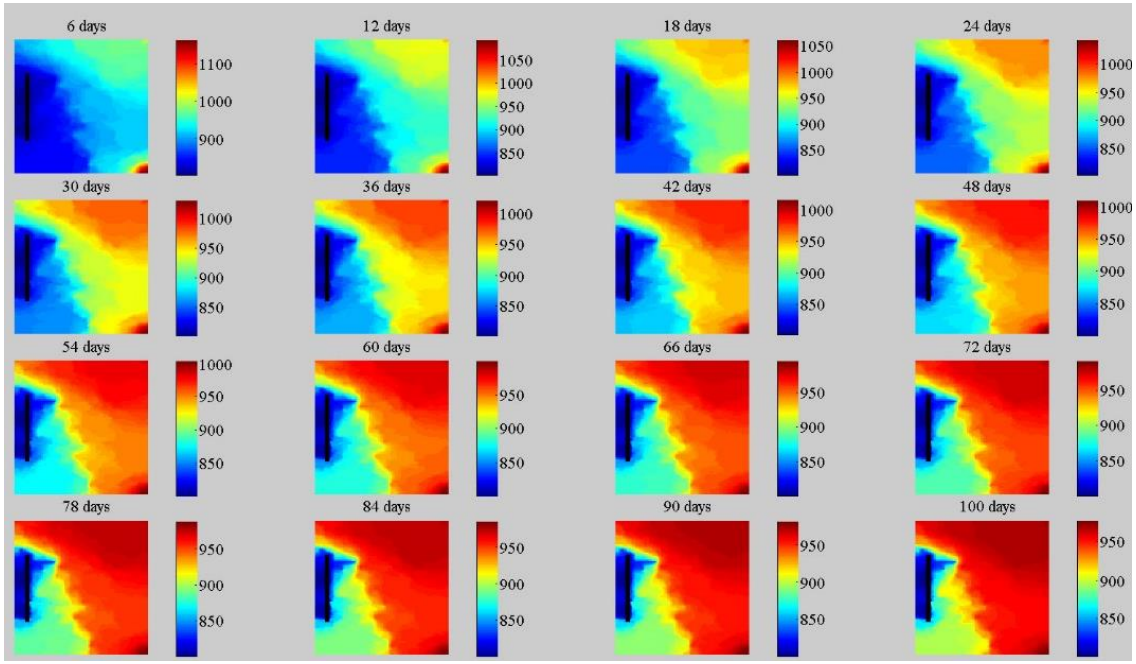

Figure 7.43 Pore pressure distribution by iterative coupling simulation.

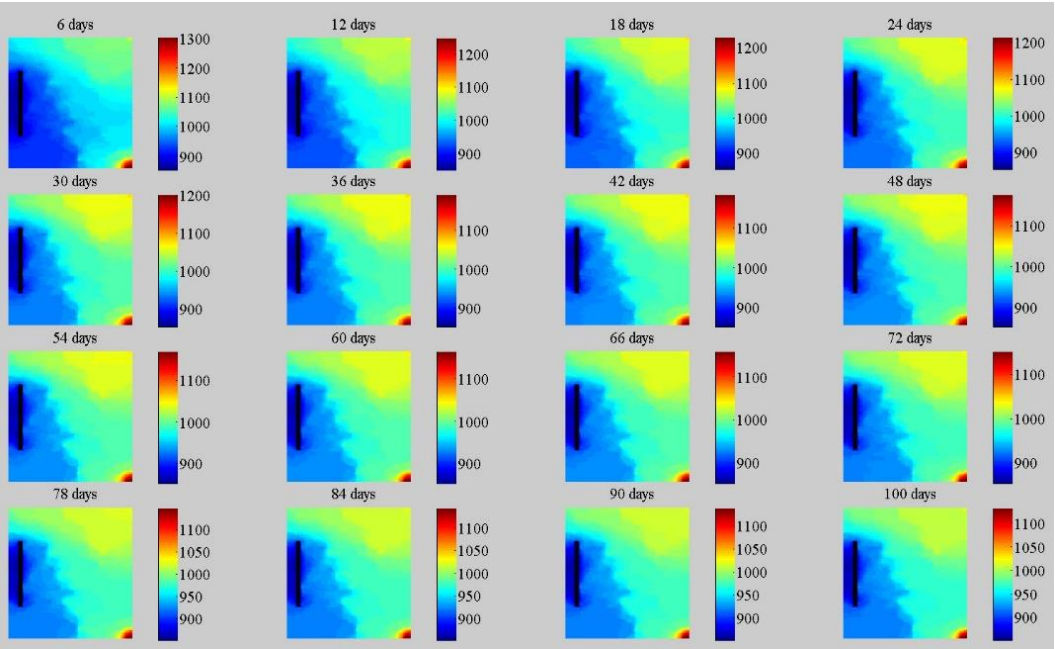

Figure 7.44 Pore pressure distribution by SIPC coupling simulation.

The iterative coupling simulation also illustrated the equivalent permeability changes over the entire reservoir area. Figures 7.45 and 7.46 show updated x- and y-directional permeabilities, after the simulation. Table 7.8 shows the changing rates of the minimum and maximum values of x- and y-directional permeability compared with initial permeability values. The minimum values for the x- and y-directional equivalent permeabilities in the iterative coupling were much smaller than those in the SIPC simulation. This was why the simulation results by empirical relationship showed proportionally changing behavior in permeability calculation. Therefore, iterative simulation showed significant decrease of equivalent permeability even though water was not saturated, and pore pressure didn’t change much compared with initial pore pressure. This could result in excessive permeability estimation in fracture flow

dominant reservoir. Even though the iterative coupling simulation also showed a permeability decrease near the horizontal well area, it was noticeable that the SIPC simulation better reflected the stress-induced aperture change and clearly showed the closed aperture effect in the permeability calculation near the horizontal well area.

The results of the maximum equivalent permeability calculation were somewhat different. The maximum value for the x-directional equivalent permeability in the iterative coupling was smaller than that in the SIPC simulation, but the maximum value for the y-directional equivalent permeability in the iterative coupling was larger than that in the SIPC simulation, as shown in Table 7.8. As described above, this was why the SIPC coupling simulation reflected fracture geometry data in the directional equivalent permeability calculation. The same aperture value differently affected the directional permeability, depending upon the fracture geometry (such as fracture orientation, length, aperture value, and aperture segment numbers). Therefore, the calculated maximum values of the x- and y-directional permeabilities by SIPC coupling simulation showed different behaviors, as compared to those obtained from the iterative coupling simulation.

Table 7.8 The changing rates of the minimum and maximum values of the x- and y-directional permeabilities

	X-directional permeability, k_x		Y-directional permeability, k_y	
	CR of the minimum k_x	CR of the maximum k_x	CR of the minimum k_y	CR of the maximum k_y
Iterative coupling	7.6 %	315.6 %	7.6 %	786.1 %
SIPC coupling	100 %	485.9 %	100 %	599.0 %
Relative CR	1315.8 %	154.0 %	1315.8 %	76.2 %

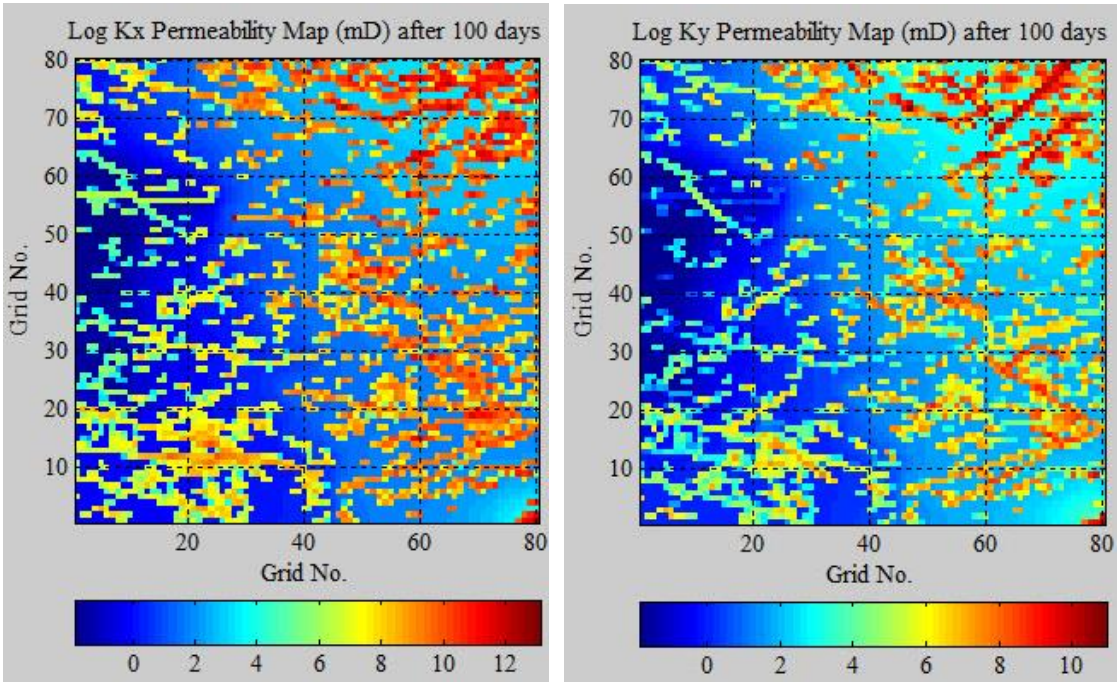

Figure 7.45 The x- and y-directional permeabilities by iterative coupling after 100 days.

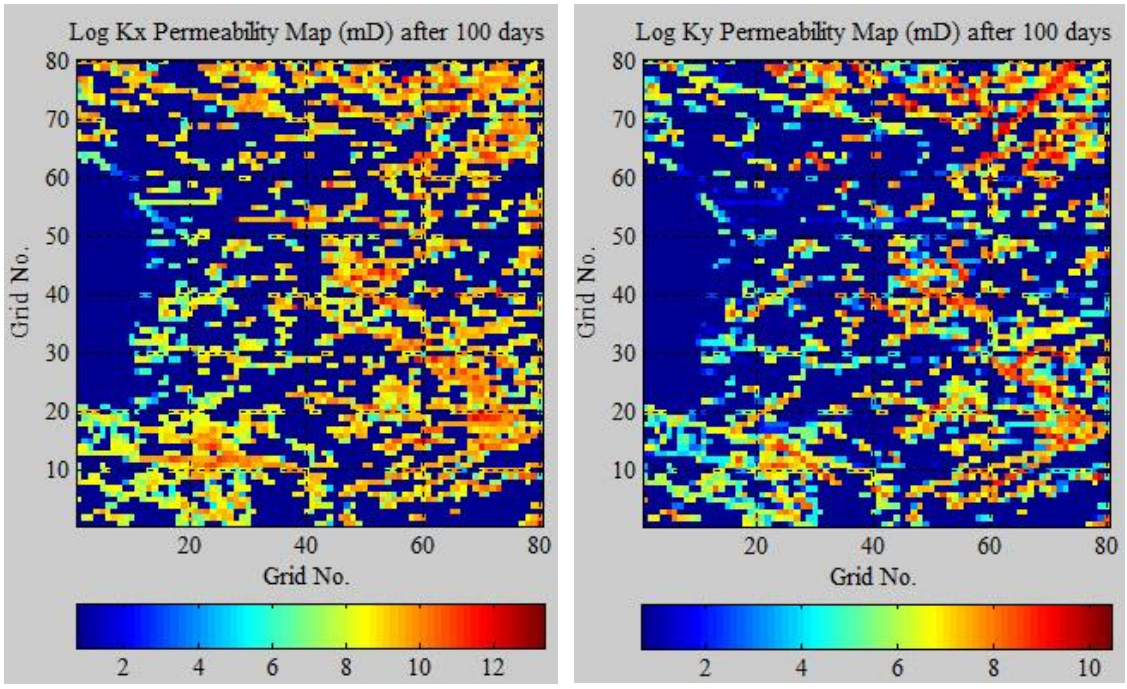

Figure 7.46 The x- and y-directional permeabilities by SIPC coupling after 100 days.

The calculated water saturation maps by each simulation method are shown in Figures 7.47, 7.48, and 7.49. The simulation results of the oil production rate, water cut, and cumulative oil production are plotted in Figures 7.50, 7.51, and 7.52. Due to a lower Young's modulus and injection rate, the iterative coupling simulation showed a different level of production performance with the FDM simulation results, as compared to the previous case study. After 100 days of simulation, SIPC coupling simulation showed the difference rate range from 99.7 % to 102.2 %. Even though the difference of rate was not much, the difference of rate increased as production time passed. In addition, SIPC coupling simulation corresponding value of JCS 20, 30, and 40 showed better production performance than did FDM simulation.

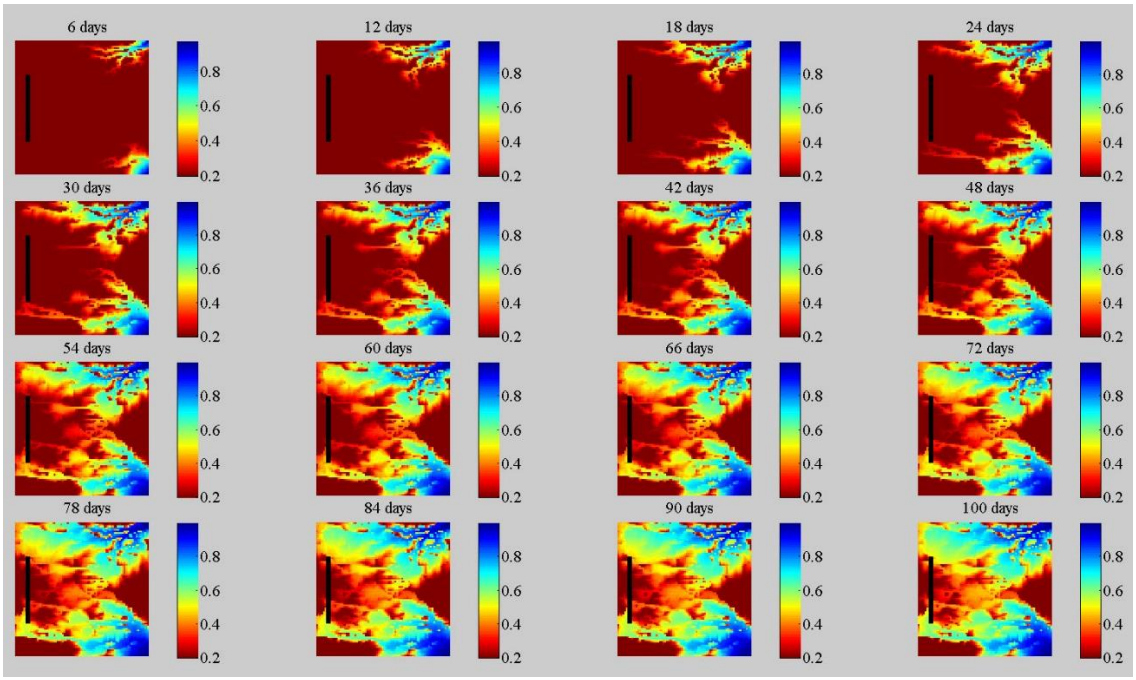

Figure 7.47 Water saturation by FDM simulation.

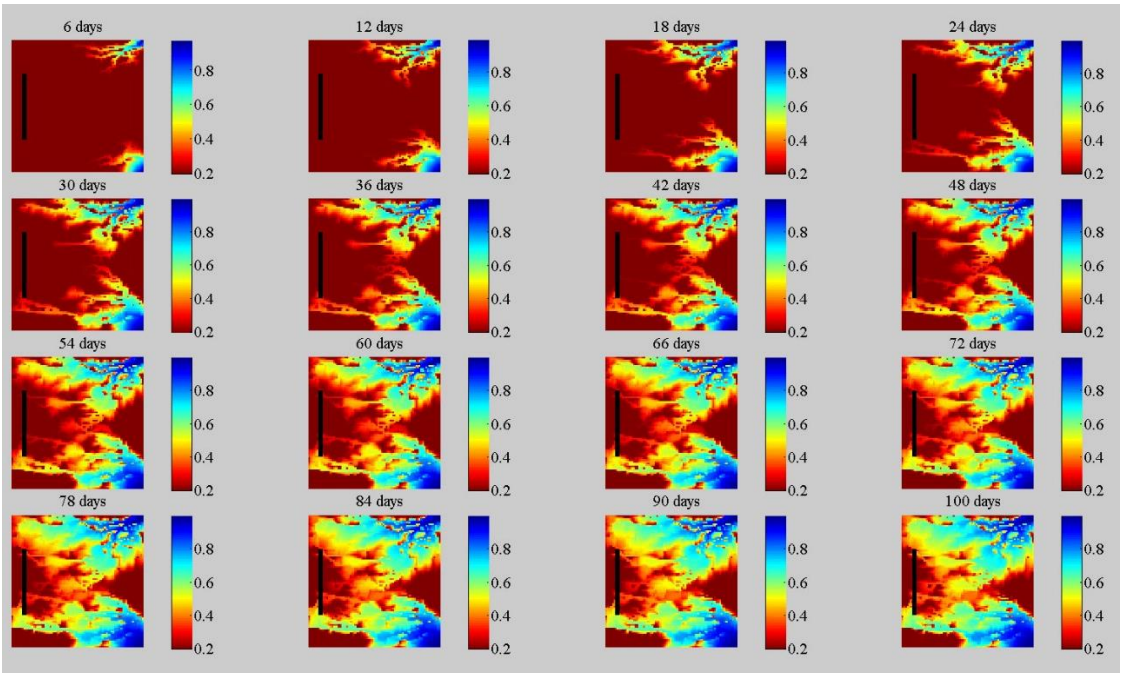

Figure 7.48 Water saturation by iterative coupling simulation.

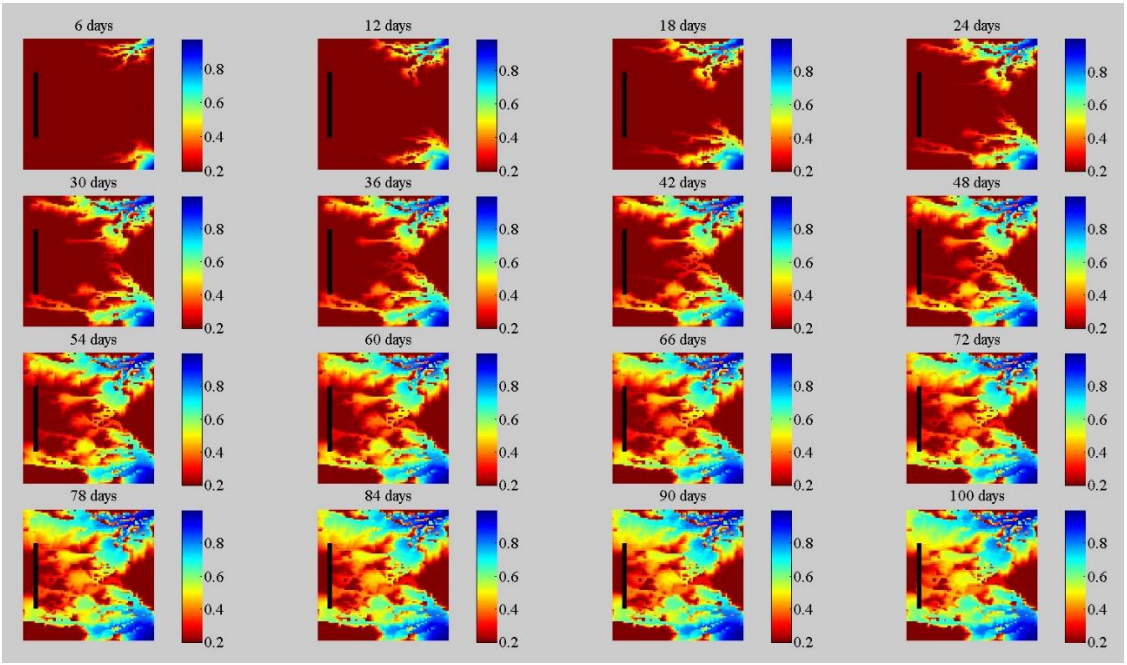

Figure 7.49 Water saturation by SIPC coupling simulation.

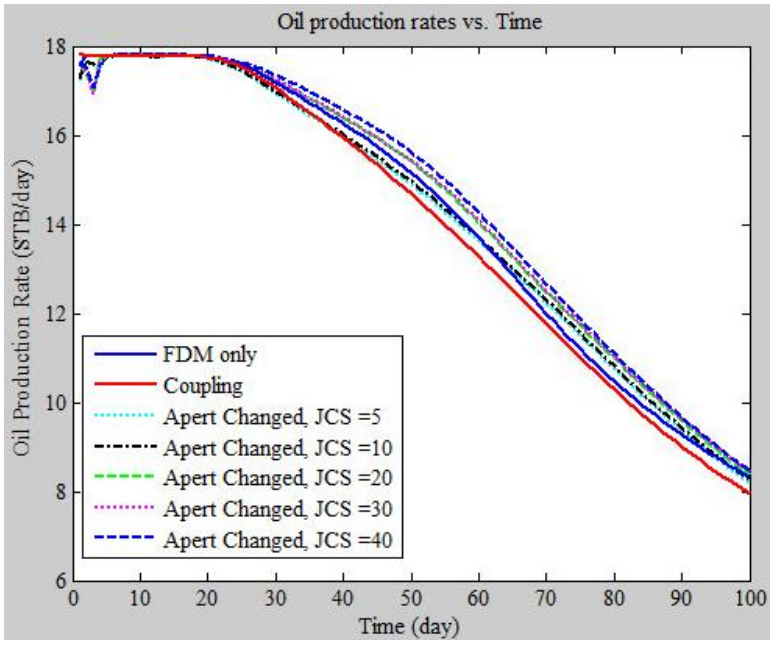

Figure 7.50 Oil production rate by FDM, iterative coupling and SIPC coupling simulations.

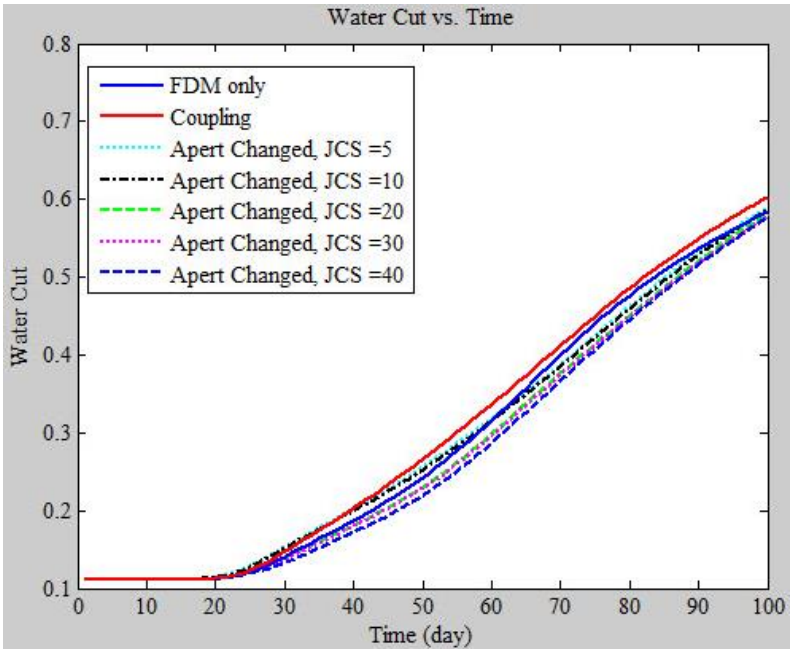

Figure 7.51 Water cut by FDM, iterative coupling and SIPC coupling simulations.

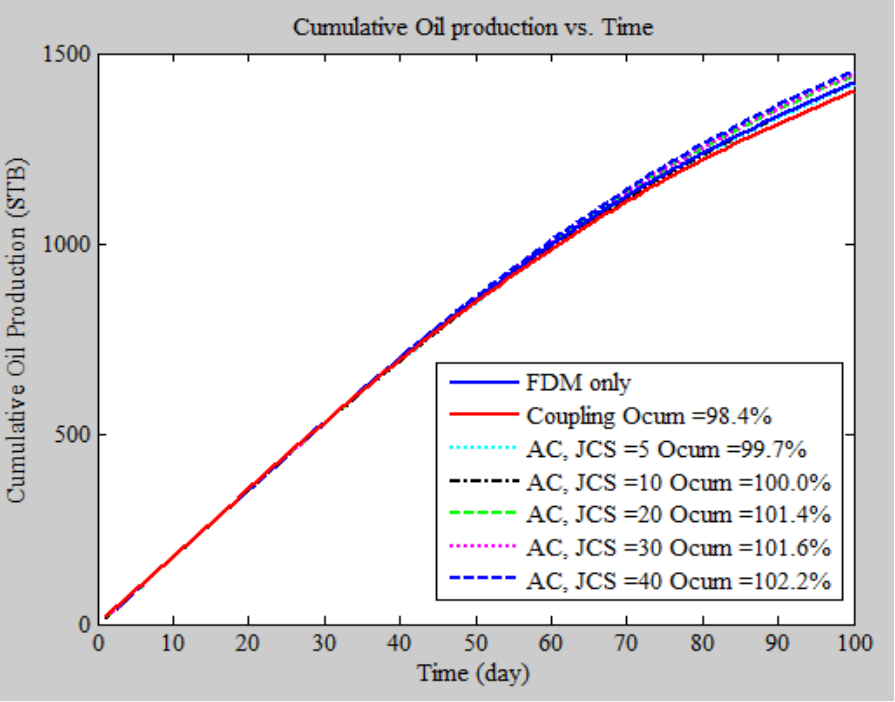

Figure 7.52 Cumulative oil production by FDM, iterative coupling and SIPC coupling simulations.

Figure 7.53 shows the updated aperture distributions after the SIPC coupling simulation. As shown in the Figure, the simulation results show a behavior similar to that of the previous case study: a larger aperture deformation with a lower JCS value, and a normal distribution of the changed aperture distributions. However, as highlighted in the Figure, this case study shows a different aperture closing behavior after the SIPC coupling simulation. Table 7.9 shows the changing rates of the mean value of the updated aperture distribution, as compared with the mean value of the initial aperture distribution.

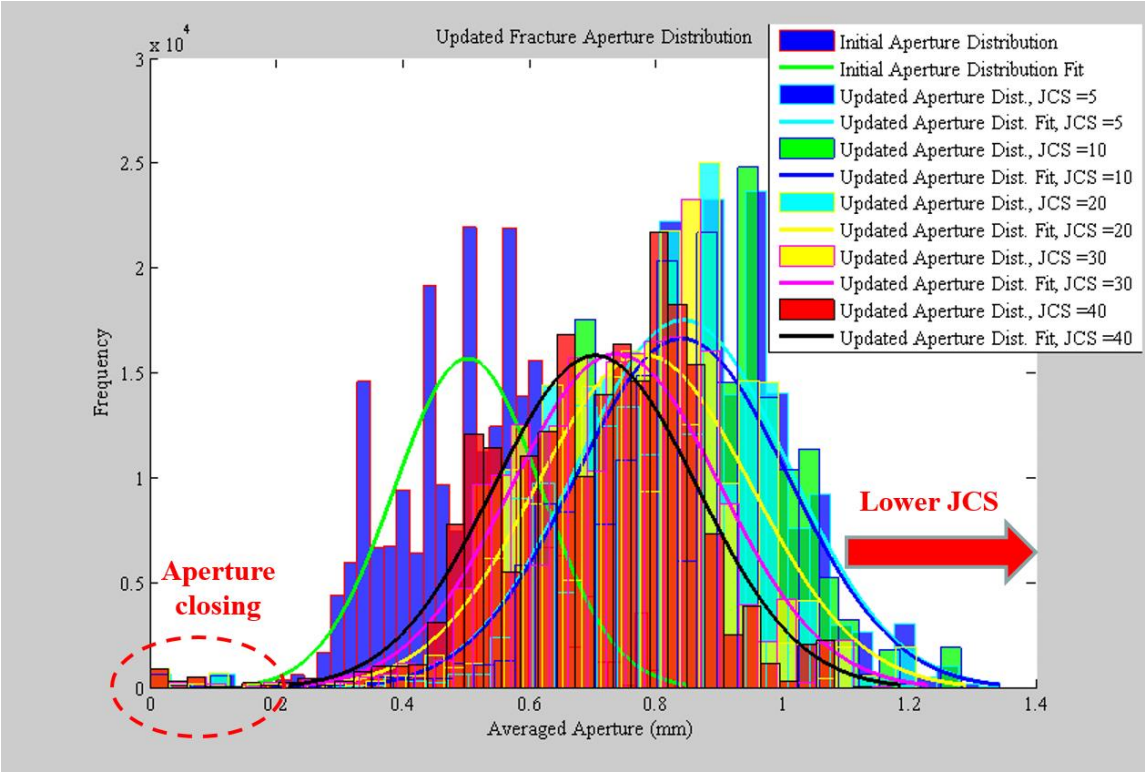

Figure 7.53 Updated aperture distributions after the SIPC coupling simulation.

Table 7.9 The changing rates of the mean value of the updated aperture distribution

JCS	5	10	20	30	40
Changing rate of the mean value	156.3 %	167.3 %	155.4 %	146.7 %	140.1 %

CHAPTER VIII

SUMMARY, CONCLUSIONS AND RECOMMENDATIONS

8.1 Summary

In this work, I developed equivalent permeability estimation codes using generated FDFN data in order to investigate the effect of fracture geometry on directional permeability estimation. In order to consider large numbers of fractures but retain an efficient level of computational cost, I used an Equivalent Continuum (EC) approach for the equivalent permeability calculation. After FDFN generation, the directional equivalent permeability was calculated by a modified Oda's algorithm, and the equivalent permeability was a function of the fracture orientation, length, density, and aperture values in the modified Oda's method. I used a 1,000-time Monte Carlo simulation and generated a CDF plot to determine a P50 fracture map representing the fracture network condition of the reservoir. The domain size was determined from the REV simulation.

In order to investigate the geomechanics effect on the flow simulation, I developed iterative coupling simulation codes that estimated updated permeability changes using empirical relationships controlled by volumetric strain, water saturation and/or porosity variations. However, because these empirical equations had certain limitations preventing them from being directly applied to different reservoir conditions. In addition, it was difficult for the EC approach to properly describe the fracture flow effect on the simulation, due to certain inherent characteristics of the method.

To overcome this shortcoming, I proposed a combined Discrete Fracture Network (DFN) and Equivalent Continuum (EC) approach. In order to describe the anisotropic characteristics of directional permeability change, I developed Stress-Induced Permeability Changing (SIPC) coupling simulation algorithm. Fractal Discrete Fracture Network (FDFN) data were imported to the SIPC simulator to estimate effective normal stress changes of fractures; stress-induced permeability was then calculated by a modified Oda's EC approach.

The calculated permeability data were then passed to the reservoir simulator. In order to investigate the coupling and rock property effects on production performance, coupling simulations were conducted. MRST was used for the flow simulator and an FEM Newton-Raphson framework was implemented for the geomechanics simulator. Porosity was the coupling parameter, and an iterative coupling scheme was used for the coupling simulation.

As a synthetic field case study, a stress-sensitive reservoir was considered. For that, the Belridge and Lost Hills (LH) oil fields in California were selected. Through a series of literature reviews, I tried to select a reasonable field data. More x-directional fractures were considered through a 5-spot pattern case study with a relatively large domain size, and a horizontal well case study with a small domain size.

In order to obtain more reliable simulation results, in addition to general reservoir properties such as Young's modulus, porosity, compressibility, saturation, and so on, specific reservoir properties were also required in this study, such as the Joint Roughness Coefficient (JRC), Joint Compressive Strength (JCS), and/or normal stiffness.

The contributions of this work are as follows:

- Effective reflection of fracture network geometry effects in permeability estimations and coupling simulations.
- A combined DFN and EC approach for performing stress-induced permeability changing coupling simulations that save on computational costs.
- Development of SIPC simulation codes for estimating stress-induced aperture deformations.
- The ability to describe anisotropic stress-induced aperture deformation effects on permeability estimations and coupling simulations.
- Direct calculation of fracture porosity and permeability changes considering stress-induced aperture deformations.
- The ability to consider and apply reservoir properties to permeability estimations and coupling simulations for better results.

8.2 Conclusions

In order to investigate the coupling and rock property effects on production performance, coupling simulation code was developed.

I verified the iterative coupling codes using the analytical solution to Terzaghi's 1D consolidation problem. For that, I simulated the one-way drainage problem; a comparison of the numerical and analytical solutions showed a good match.

In the equivalent permeability simulation case study, I considered more y-directional than x-directional fractured reservoirs in order to estimate the fracture geometry effect on the equivalent permeability calculation. From the results of the equivalent permeability simulation, it was found that the calculated x- and y-directional equivalent permeabilities effectively reflected the heterogeneous and anisotropic characteristics of the generated FDFN.

As a synthetic field case study, a stress-sensitive reservoir was simulated.

In the 5-spot pattern case study, the reservoir pore pressure increased due to water injection. Even though the pore pressure decreased near the producing area, the overall calculated pore pressure was higher than the initial pore pressure This resulted in a decrease in effective stress and increase in the porosity and equivalent permeabilities during the coupling simulation. However, the iterative and SIPC coupling simulation results showed different behaviors in the pore pressure and permeability calculations. The iterative coupling simulation showed isotropic and proportional changing behaviors in the permeability estimation. It was observed that the equivalent permeability increased not only in the fractured zone but also in the non-fractured zone.

In the horizontal well case study, iterative coupling showed a significant decrease in the Changing Rate (CR) of the minimum permeability (7.6%), even though the water was not saturated; the pore pressure didn’t change significantly, as compared with the initial pore pressure. In the case of a fracture flow dominant reservoir with a low matrix permeability, this might result in an excessive permeability estimation.

In the CR calculation of the minimum and maximum permeabilities of the 5-spot pattern case study, the SIPC coupling simulation showed less relative CR with regards to the minimum permeability, 41% and 44.8%, and more relative CR with regards to the maximum permeability, 151% and 137%, in both directions, as compared with the iterative coupling simulation. In the SIPC simulation, the equivalent permeability of the non-fractured zone didn't increase because the permeability was directly calculated by a modified Oda's algorithm using the stress-induced aperture deformation and fracture network geometry data. If the matrix flow is also an important parameter, the matrix permeability increase should be considered in the SIPC coupling simulation.

As shown in the permeability simulation results of the horizontal well case study, the SIPC coupling simulation better reflected the anisotropic characteristics of the directional permeability change and showed a clearer aperture closing effect near the horizontal well than did the iterative coupling simulation. The SIPC coupling simulation showed a relative CR of 154% for the x-directional and 76% for the y-directional maximum permeabilities, as compared with the iterative coupling simulation results. This was somewhat different from the 5-spot pattern case study. Thanks to the ability of the SIPC coupling simulation to describe anisotropic stress-induced aperture deformation effects on permeability estimations and coupling simulations, it showed a smaller CR for the y-directional maximum permeability than did the iterative coupling simulation.

The effects of different Joint Compressive Strength (JCS) values in the coupling simulation were investigated through synthetic field case studies. Cases with lower JCS

values showed wider aperture deformation behavior and larger directional permeability changes. It was observed that the CR of the mean aperture value ranged from 179% to 249% in the 5-spot pattern case, and from 140% to 156% in the horizontal well case.

Larger JCS cases showed better production performances. Simulation results showed that the CR of the cumulative oil production ranged from 92.7% to 96.2% in the 5-spot pattern case, and from 99.6% to 102.2% in the horizontal well case. Even though the difference in rate was not significant, it increased as the production time increased.

After a comparison of the FDM and iterative coupling simulations, it was observed that the SIPC coupling simulation successfully described the anisotropic characteristics of the directional permeability estimation, and reflected the reservoir properties in the coupling simulation. The combined DFN and EC approach was effectively applied to the stress-induced permeability changing reservoir coupling simulation.

8.3 Recommendations for Future Works

In this work, I limited my investigation to a two dimensional coupling simulation with a Cartesian grid system. To apply my work to more general cases such as subsidence analysis, a three dimensional coupling simulation model is required.

Even though unstructured grid systems require more computational cost, they can describe the complex geometry of a fractured reservoir in more detail. In order to analyze the subsidence problem near the well bore area, a refined or unstructured gridding is especially necessary. Through a modification of the coupling module, the

geomechanics FEM code can be coupled with other unstructured gridding fracture flow simulators.

I considered only stress-induced normal aperture deformation in this study. However, stress-induced shear aperture deformation could greatly affect the total aperture deformation, depending upon the reservoir's properties and condition. Therefore, to get more reliable simulation results, a stress-induced shear aperture deformation calculation was also required.

I assumed that the stress of the middle point of the fracture segment represented the stress condition along the plane of the fracture segment. Also, the JRC and JCS of the fracture were assumed to be uniform for all of the fractures, because JRC and JCS are functions of effective stress. However, the stresses were not constant throughout the fracture length. Thus, it is recommended that future researchers consider stress changes at multiple points in each fracture.

REFERENCES

Aghighi, M. A. (2007). Fully coupled fluid flow and geomechanics in the study of hydraulic fracturing and post-fracture production. (Doctor of Philosophy), The University of New South Wales, Sydney, Australia. Retrieved from http://www.unsworks.unsw.edu.au/primo_library/libweb/action/dlDisplay.do?vid=UNSWORKS&docId=unsworks_1382&fromSitemap=1&afterPDS=true Accessed on 07/06/2013

Albinali, A., Kazemi, H., & Alghamdi, B. (2011). Geomechanics and Fluid Flow Modeling Using Finite-Difference Method. Paper presented at the SPE Reservoir Characterisation and Simulation Conference and Exhibition, Abu Dhabi, UAE https://www.onepetro.org/conference-paper/SPE-148292-MS Accessed on 06/20/2013

Amaziane, B., Hontans, T., & Koebbe, J. V. (2001). Equivalent Permeability and Simulation of Two-Phase Flow in Heterogeneous Porous Media. *Computational Geosciences, 5*(4), 279-300. doi:10.1023/a:1014508622020

Aziz, K., & Settari, A. (1979). Petroleum reservoir simulation (reprint ed.). London: Applied Science Publishers.

Bandis, S. C., Lumsden, A. C., & Barton, N. R. (1983). Fundamentals of rock joint deformation. *International Journal of Rock Mechanics and Mining Sciences and Geomechanics Abstracts, 20*(6), 249-268. doi:10.1016/0148-9062(83)90595-8

Barton, N., Bandis, S., & Bakhtar, K. (1985). Strength, deformation and conductivity coupling of rock joints. *International Journal of Rock Mechanics and Mining Sciences & Geomechanics Abstracts, 22*(3), 121-140. doi:10.1016/0148-9062(85)93227-9

Barton, N., & Choubey, V. (1977). The shear strength of rock joints in theory and practice. *Rock Mechanics, 10*(1/2), 1-54. doi:10.1007/BF01261801

Bear, J. (1972). Dynamics of Fluids In Porous Media: American Elsevier Publishing Company.

Bear, J., & Bakhmaṭ, Y. (1991). Introduction to Modeling of Transport Phenomena in Porous Medía: Kluwer Academic Publishers.

Berg, R. R. (1970). Method of Determining Permeability from Reservoir Rock Properties. *Transactions of Gulf Coast Association of Geological Societies, 20*, 303-317.

Biot, M. A. (1941). General Theory of Three-Dimensional Consolidation. *Journal of Applied Physics, 12*(2), 155-164. doi:10.1063/1.1712886

Bour, O., Davy, P., Darcel, C., & Odling, N. (2002). A statistical scaling model for fracture network geometry, with validation on a multiscale mapping of a joint network (Hornelen Basin, Norway). *Journal of Geophysical Research-Solid Earth, 107*(B6), ETG 4-1-ETG 4-12. doi:10.1029/2001JB000176

Brown, S. R., & Bruhn, R. L. (1998). Fluid permeability of deformable fracture networks. *Journal of Geophysical Research-Solid Earth, 103*(B2), 2489-2500. doi:10.1029/97JB03113

Bruno, M. S., & Bovberg, C. A. (1992). Reservoir compaction and surface subsidence above the Lost Hills Field. California. Paper presented at the The 33th U.S. Symposium on Rock Mechanics (USRMS), Santa Fe, New Mexico https://www.onepetro.org/conference-paper/ARMA-92-0263 Accessed on 07/07/2014

Carman, P. C. (1956). Flow of Gases Through Porous Media. New York: Academic Press.

Chang, J., & Yortsos, Y. C. (1990). Pressure Transient Analysis of Fractal Reservoirs. *Spe Journal, 5*(01), 31-38. doi:10.2118/18170-pa

Chen, H. Y., Teufel, L. W., & Lee, R. L. (1995). Coupled Fluid Flow and Geomechanics in Reservoir Study - I. Theory and Governing Equations. Paper presented at the SPE Annual Technical Conference and Exhibition, Dallas, Texas. https://www.onepetro.org/conference-paper/SPE-30752-MS Accessed on 06/16/2013

Chin, L. Y., Raghavan, R., & Thomas, L. K. (1998). Fully Coupled Analysis of Well Responses in Stress-Sensitive Reservoirs. Paper presented at the SPE Annual Technical Conference and Exhibition, New Orleans, Louisiana. paper retrieved from https://www.onepetro.org/conference-paper/SPE-48967-MS Accessed on 05/22/2013

Chin, L. Y., Raghavan, R., & Thomas, L. K. (2000). Fully coupled geomechanics and fluid-flow analysis of wells with stress-dependent permeability. *Spe Journal, 5*(1), 32-45. doi:10.2118/58968-PA

Chin, L. Y., Thomas, L. K., Sylte, J. E., & Pierson, R. G. (2002). Iterative Coupled Analysis of Geomechanics and Fluid Flow for Rock Compaction in Reservoir Simulation. *Oil & Gas Science and Technology, 57*(5), 485-497. doi:10.2516/ogst:2002032

Coates, G. R., & Dumanoir, J. L. (1973). A New Approach To Improved Log-Derived Permeability. Paper presented at the SPWLA 14th Annual Logging Symposium, Lafayette, Louisiana. https://www.onepetro.org/conference-paper/SPWLA-1973-R Accessed on 06/18/2013

Costa, A. (2006). Permeability-porosity relationship: A reexamination of the Kozeny-Carman equation based on a fractal pore-space geometry assumption. *Geophysical Research Letters, 33*(2), L02318 02311-02315. doi:10.1029/2005GL025134

Darcel, C., Bour, O., Davy, P., & de Dreuzy, J. R. (2003). Connectivity properties of two-dimensional fracture networks with stochastic fractal correlation. *Water Resources Research, 39*(10), SBH 1-13. doi:10.1029/2002wr001628

Dershowitz, B., LaPointe, P., Eiben, T., & Wei, L. (2000). Integration of Discrete Feature Network Methods With Conventional Simulator Approaches. *Spe Journal, 3*(2), 165-170. doi:10.2118/62498-pa

Dershowitz, W., Pointe, P. L., & Doe, T. (2004). Advances in Discrete Fracture Network Modeling. Paper presented at the Proceedings of the US EPA/NGWA Fractured Rock Conference. https://www.researchgate.net/publication/229047622_Advances_in_discrete_fracture_network_modeling Accessed on 04/18/2014.

Dobson, P. (2014). Advanced Well Stimulation Technologies in California. Retrieved from Sacramento, California: http://ccst.us/publications/2014/2014wst.php Accessed on 10/11/2015

Du, J., & Wong, R. C. K. (2007a). Application of strain-induced permeability model in a coupled geomechanics-reservoir simulator. *Journal of Canadian Petroleum Technology, 46*(12), 55-61. doi:10.2118/07-12-01

Du, J., & Wong, R. C. K. (2007b). Coupled Geomechanics Reservoir Simulation of UTF Phase A Project Using a Full Permeability Tensor. *Journal of Canadian Petroleum Technology, 48*(07). doi:10.2118/09-07-66

Fardin, N., Stephansson, O., & Jing, L. R. (2001). The scale dependence of rock joint surface roughness. *International Journal of Rock Mechanics and Mining Sciences, 38*(5), 659-669. doi:10.1016/S1365-1609(01)00028-4

Fast, R. E., Murer, A. S., & Timmer, R. S. (1994). Description and Analysis of Cored Hydraulic Fractures, Lost Hills Field, Kern County, California. doi:10.2118/24853-PA

Feder, J. (1988). Fractals. New York: Plenum Press.

Gai, X. (2004). A coupled geomechanical AND reservoir flow model on parallel computers. (Doctor of Philosophy), The University of Texas at Austin, Austin, Texas. Retrieved from http://hdl.handle.net/2152/1187 Accessed on 08/20/2013

Geertsma, J. (1957). The Effects of Pressure Decline on Volumetric Changes of Porous Rocks. Paper presented at the Society of Petroleum Engineers. https://www.onepetro.org/general/SPE-728-G Accessed on 08/24/2013

Goodman, R. E. (1976). Methods of Geological Engineering: In Discontinuous Rocks (illustrated ed.): West Information Publishing Group.

Goovaerts, P. (1997). Geostatistics for Natural Resources Evaluation: Oxford University Press.

Harlow, F. (1995). Introduction to finite-difference methods for numerical fluid dynamics (LA-12984 DE96008885). Retrieved from Department of Energy's (DOE): http://www.osti.gov/scitech/servlets/purl/212567 Accessed on 06/20/2013

Harstad, H., Teufel, L. W., Lorenz, J. C., & Brown, S. R. (1996). Characterization and fluid flow simulation of naturally fractured Frontier sandstone, Green River Basin, Wyoming (SAND96-1955). Retrieved from Sandia National Laboratories: http://www.osti.gov/bridge/servlets/purl/383569-JX2OIf/webviewable/ Accessed on 09/27/2010

He, J., Chen, S.-h., & Shahrour, I. (2013). Numerical estimation and prediction of stress-dependent permeability tensor for fractured rock masses. *International Journal of Rock Mechanics and Mining Sciences, 59*(0), 70-79. doi:10.1016/j.ijrmms.2012.12.001

Hirata, T. (1989). Fractal dimension of fault systems in Japan: Fractal structure in rock fracture geometry at various scales. *Pure and Applied Geophysics (PAGEOPH), 131*(1-2), 157-170. doi:10.1007/bf00874485

Ing, T. C., & Xiaoyan, N. (2002). Coupled consolidation theory with non-Darcian flow. *Computers and Geotechnics, 29*(3), 169-209. doi:10.1016/S0266-352X(01)00022-2

Jalali, M. R., & Dusseault, M. B. (2008). Coupled Fluid-Flow And Geomechanics In Naturally Fractured Reservoirs. Paper presented at the ISRM International Symposium - 5th Asian Rock Mechanics Symposium, Tehran, Iran. https://www.onepetro.org/conference-paper/ISRM-ARMS5-2008-153 Accessed on 02/23/2012

Katz, A. J., & Thompson, A. H. (1985). Fractal sandstone pores: Implications for conductivity and pore formation. *Physical Review Letters, 54*(12), 1325-1328. doi:10.1103/PhysRevLett.54.1325

Kim, J. (2010). Sequential Methods for Coupled Geomechanics and Multiphase Flow. (Doctor of Philosophy), Stanford University. Retrieved from https://pangea.stanford.edu/ERE/pdf/pereports/PhD/Kim10.pdf Accessed on 06/12/2013

Kim, T. H., & Schechter, D. S. (2009). Estimation of Fracture Porosity of Naturally Fractured Reservoirs With No Matrix Porosity Using Fractal Discrete Fracture Networks. *Spe Journal, 12*(02), 232-242. doi:10.2118/110720-pa

Krige, D. (1951). A Statistical Approach to Some Basic Mine Valuation Problems on the Witwatersrand. *Journal of the Chemical, Metallurgical and Mining Society of South Africa, 52*(6), 119-139. doi:10.2307/3006914

Kulatilake, P. H. S. W., & Um, J. (1999). Requirements for accurate quantification of self-affine roughness using the roughness-length method. *International Journal of Rock Mechanics and Mining Sciences, 36*(1), 5-18. doi:10.1016/S0148-9062(98)00170-3

Lee, I.-S. (2008). Computational Techniques for Efficient Solution of Discretized Biot's Theory for Fluid Flow in Deformable Porous Media. (Doctor of Philosophy), Virginia Polytechnic Institute and State University. Retrieved from https://theses.lib.vt.edu/theses/available/etd-07012008-115136/ Accessed on 08/04/2013

Lewis, R. W., & Schrefler, B. A. (1998). The finite element method in the static and dynamic deformation and consolidation of porous media: John Wiley.

Lie, K. A., Krogstad, S., Ligaarden, I. S., Natvig, J. R., Nilsen, H. M., & Skaflestad, B. (2011). Open-source MATLAB implementation of consistent discretisations on complex grids. *Computational Geosciences, 16*(2), 297-322. doi:10.1007/s10596-011-9244-4

Liu, H. H., Bodvarsson, G. S., Lu, S. L., & Molz, F. J. (2004). A corrected and generalized successive random additions algorithm for simulating fractional levy motions. *Mathematical Geology, 36*(3), 361-378. doi:10.1023/B:Matg.0000028442.71929.26

Long, J. C. S., Remer, J. S., Wilson, C. R., & Witherspoon, P. A. (1982). Porous media equivalents for networks of discontinuous fractures. *Water Resources Research, 18*(3), 645-658. doi:10.1029/WR018i003p00645

Lu, B. (2008). Iteratively Coupled Reservoir Simulation for Multiphase Flow in Porous Media. (Doctor of Philosophy), The University of Texas at Austin. Retrieved from http://hdl.handle.net/2152/3880 Accessed on 08/03/2013

Mandelbrot, B. B. (1983). The Fractal Geometry of Nature (Updated and augmented ed.). New York : W.H. Freeman: Macmillan.

Matheron, G. (1963). Principles of geostatistics. *Economic Geology & the Bulletin of the Society of Economic Geologists, 58*, 1246-1266. doi:10.2113/gsecongeo.58.8.1246

McGaughey, D. R., & Aitken, G. J. M. (2000). Statistical analysis of successive random additions for generating fractional Brownian motion. *Physica A: Statistical Mechanics and its Applications, 277*(1–2), 25-34. doi:10.1016/S0378-4371(99)00438-0

Min, K.-B., & Jing, L. (2003). Numerical determination of the equivalent elastic compliance tensor for fractured rock masses using the distinct element method. *International Journal of Rock Mechanics and Mining Sciences, 40*(6), 795-816. doi:10.1016/S1365-1609(03)00038-8

Min, K.-B., Jing, L., & Stephansson, O. (2004). Determining the equivalent permeability tensor for fractured rock masses using a stochastic REV approach: Method and application to the field data from Sellafield, UK. *Hydrogeology Journal, 12*(5), 497-510. doi:10.1007/s10040-004-0331-7

Minkoff, S. E., Stone, C. M., Bryant, S., Peszynska, M., & Wheeler, M. F. (2003). Coupled fluid flow and geomechanical deformation modeling. *Journal of Petroleum Science and Engineering, 38*(1–2), 37-56. doi:10.1016/S0920-4105(03)00021-4

Nelson, P. H. (1994). Permeability-porosity relationships in sedimentary rocks. *Log Analyst, 35*(3), 38-62.

Oda, M. (1982). Fabric tensor for discontinuous geological materials. *Soils and Foundations, 22*(4), 96-108. doi:10.3208/sandf1972.22.4_96

Oda, M. (1985). Permeability Tensor for Discontinuous Rock Masses. *Geotechnique, 35*(4), 483-495. doi:10.1680/geot.1985.35.4.483

Oda, M., Hatsuyama, Y., & Ohnishi, Y. (1987). Numerical experiments on permeability tensor and its application to jointed granite at Stripa Mine, Sweden. *Journal of Geophysical Research: Solid Earth, 92*(B8), 8037-8048. doi:10.1029/JB092iB08p08037

Oda, M., Yamabe, T., & Kamemura, K. (1986). A crack tensor and its relation to wave velocity anisotropy in jointed rock masses. *International Journal of Rock Mechanics and Mining Sciences and, 23*(6), 387-397. doi:10.1016/0148-9062(86)92304-1

Olarewaju, J. (1996). Modeling Fractured Reservoirs With Stochastic Fractals. Paper presented at the Abu Dhabi International Petroleum Exhibition and Conference, Abu Dhabi, United Arab Emirates. https://www.onepetro.org/conference-paper/SPE-36207-MS Accessed on 02/07/2010

Pan, F. (2009). Development and application of a coupled geomechanics model for a parallel compositional reservoir simulator. (Doctor of Philosophy), The University of Texas at Austin. Retrieved from http://hdl.handle.net/2152/7675 Accessed on 06/12/2013

Pan, F., Sepehrnoori, K., & Chin, L. Y. (2009). A New Solution Procedure for a Fully Coupled Geomechanics and Compositional Reservoir Simulator. Paper presented at the SPE Reservoir Simulation Symposium, The Woodlands, Texas. https://www.onepetro.org/conference-paper/SPE-119029-MS Accessed on 06/20/2013

Peaceman, D. W. (1978). Interpretation of Well-Block Pressures in Numerical Reservoir Simulation. *Society of Petroleum Engineers Journal, 18*(03), 183-192. doi:10.2118/6893-PA

Priest, S. D. (1993). Discontinuity Analysis for Rock Engineering: Chapman & Hall.

Rayan, R. (2014). Numerical Modelling of Flow-Mechanics Coupling in Fractured Reservoirs. (Master Thesis), ETH-Zürich. Retrieved from http://e-collection.library.ethz.ch/eserv/eth:47125/eth-47125-01.pdf Accessed on 04/01/2015

Sakellariou, M., Nakos, B., & Mitsakaki, C. (1991). On the fractal character of rock surfaces. *International Journal of Rock Mechanics and Mining Sciences & Geomechanics Abstracts, 28*(6), 527-533. doi:10.1016/0148-9062(91)91129-F

Samuel, U. (2014). A Permeability-Porosity-Saturation Correlation for Niger Delta. *Asia Pacific Journal of Multidisciplinary Research, 2*(2), 20-23.

Settari, A., & Mourits, F. M. (1998). A Coupled Reservoir and Geomechanical Simulation System. *Spe Journal, 3*(03), 219-226. doi:10.2118/50939-pa

Settari, A., & Walters, D. A. (2001). Advances in Coupled Geomechanical and Reservoir Modeling With Applications to Reservoir Compaction. *Spe Journal, 6*(03), 334 - 342. doi:10.2118/74142-pa

Sherif, F. N. (2012). MATLAB FEM Code - From Elasticity to Plasticity. (Master Thesis), Norges teknisk-naturvitenskapelige Universitet. Retrieved from http://hdl.handle.net/11250/232148 Accessed on 08/08/2013

Smith, I. M., & Griffiths, D. V. (1998). Programming the Finite Element Method (3rd ed. ed.). Chichester ; New York: John Wiley & Sons.

Ta, Q. D. (2007). Coupled fluid flow-geomechanics simulations applied to compaction and subsidence estimation in stress sensitive & heterogeneous reservoirs. (Doctor of Philosophy), University of Adelaide. Retrieved from http://hdl.handle.net/2440/56375 Accessed on 06/12/2013

Terzaghi, K. (1926). Principles of soil mechanics: McGraw-Hill.

Terzaghi, K. (1943). Theoretical soil mechanics: J. Wiley and Sons, inc.

Thomas, L. K., Chin, L. Y., Pierson, R. G., & Sylte, J. E. (2003). Coupled Geomechanics and Reservoir Simulation. *Spe Journal, 8*(04), 350-358. doi:10.2118/87339-pa

Timur, A. (1968). An Investigation Of Permeability, Porosity, & Residual Water Saturation Relationships For Sandstone Reservoirs. *9*(04).

Tixier, M. P. (1949). Evaluation of permeability from electric-log resistivity gradients. *Oil & Gas Journal, 17*, 68-73.

Torskaya, T. S., Jin, G., & Torres-Verdin, C. (2007). Pore-Level Analysis of the Relationship Between Porosity, Irreducible Water Saturation, and Permeability of Clastic Rocks. Paper presented at the SPE Annual Technical Conference and

Exhibition, Anaheim, California, U.S.A. https://www.onepetro.org/conference-paper/SPE-109878-MS Accessed on 06/29/2015

Tortike, W. S., & Ali, S. M. F. (1993). Reservoir Simulation Integrated with Geomechanics. *Journal of Canadian Petroleum Technology*. doi:10.2118/93-05-02

Tran, D. (2002). Processes of coupling between geomechanics deformation and reservoir flow in porous media. (Master Thesis), University of Calgary, Calgary, Alberta. Retrieved from http://prism.ucalgary.ca/bitstream/1880/39460/1/2002_Tran.pdf Accessed on 08/21/2013

Tran, D., Nghiem, L., & Buchanan, L. (2005). An Overview of Iterative Coupling Between Geomechanical Deformation and Reservoir Flow. Paper presented at the SPE International Thermal Operations and Heavy Oil Symposium, Alberta, Canada. https://www.onepetro.org/conference-paper/SPE-97879-MS Accessed on 07/06/2013

Tran, D., Settari, A., & Nghiem, L. (2004). New iterative coupling between a reservoir simulator and a geomechanics module. *Spe Journal, 9*(3), 362-368. doi:Doi 10.2118/88989-Pa

Verruijt, A. (1995). Computational Geomechanics: Springer.

Verruijt, A. (2001). Soil Mechanics (pp. 315). Retrieved from http://www.kau.edu.sa/Files/0001553/files/SoilMechBook.pdf Accessed on 07/06/2015

Wang, M., Kulatilake, P. H. S. W., Um, J., & Narvaiz, J. (2002). Estimation of REV size and three-dimensional hydraulic conductivity tensor for a fractured rock mass through a single well packer test and discrete fracture fluid flow modeling. *International Journal of Rock Mechanics and Mining Sciences, 39*(7), 887-904. doi:10.1016/S1365-1609(02)00067-9

Wang, Y., Sun, S. Y., & Yu, B. (2013). On Full-Tensor Permeabilities of Porous Media from Numerical Solutions of the Navier-Stokes Equation. *Advances in Mechanical Engineering*, 1-11. doi:Doi 10.1155/2013/137086

White, J. (2009). Stabilized finite element methods for coupled flow and geomechanics. (Doctor of Philosophy), Stanford University. Retrieved from http://pqdtopen.proquest.com/pubnum/3382958.html Accessed on 08/04/2013

Wright, C. A., Conant, R. A., Golich, G. M., Bondor, P. L., Murer, A. S., & Dobie, C. A. (1995). Hydraulic Fracture Orientation and Production/Injection Induced

Reservoir Stress Changes in Diatomite Waterfloods. Paper presented at the SPE Western Regional Meeting, Bakersfield, California. https://www.onepetro.org/conference-paper/SPE-29625-MS Accessed on 01/18/2015

Wyllie, M. R. J., & Rose, W. D. (1950). Some Theoretical Considerations Related To The Quantitative Evaluation Of The Physical Characteristics Of Reservoir Rock From Electrical Log Data. *Journal of Petroleum Technology, 2*(04). doi:10.2118/950105-G

Xu, H. (2002). Production induced reservoir compaction and surface subsidence, with applications to 4D seismic. (Doctor of Philosophy), Stanford University. Retrieved from http://lib-ezproxy.tamu.edu:2048/login?url=http://search.ebscohost.com/login.aspx?direct=true&db=pta&AN=824256&site=eds-live Accessed on 01/11/2015

Yamamoto, T., Tsusaka, K., & Tanimoto, C. (2007). Deformation Moduli of Soft Rocks In Japan Through Geological Strength Index (GSI). Paper presented at the 1st Canada - U.S. Rock Mechanics Symposium, Vancouver, Canada. https://www.onepetro.org/conference-paper/ARMA-07-035 Accessed on 07/11/2015

Yang, D. (2013). A Simulator with Numerical Upscaling for the Analysis of Coupled Multiphase Flow and Geomechanics in Heterogeneous and Deformable Porous and Fractured Media. (Doctor of Philosophy), Texas A & M University. Retrieved from http://hdl.handle.net/1969.1/151194 Accessed on 10/21/2015

Zhang, Z. (2013). Hydromechanical behaviour and nonlinear flow characteristics of rock fractures. (Doctor of Philosophy), University of Wollongong. Retrieved from http://ro.uow.edu.au/theses/3802 Accessed on 11/14/2014

Zheng, Y., Burridge, R., & Burns, D. (2003). Reservoir Simulation with the Finite Element Method Using Biot Poroelastic Approach. *Massachusetts Institute of Technology*. doi:citeulike-article-id:4589633